Universidade de Aveiro
2019

Micael dos Santos Nascimento

Redes de sensores de fibra ótica para monitorização *in situ* de baterias de ião de lítio

Optical fiber sensors networks for *in situ* lithium-ion batteries monitoring

Universidade de Aveiro
2019

Micael dos Santos Nascimento

Redes de sensores de fibra ótica para monitorização *in situ* de baterias de ião de lítio

Optical fiber sensors networks for *in situ* lithium-ion batteries monitoring

Tese apresentada à Universidade de Aveiro para cumprimento dos requisitos necessários à obtenção do grau de Doutor em Engenharia Física, realizada sob a orientação científica do Professor Doutor João de Lemos Pinto (Professor Catedrático do Departamento de Física da Universidade de Aveiro) e da Doutora Marta Sofia dos Anjos Ferreira (Investigadora de Pós-Doutoramento do i3N e do Departamento de Física da Universidade de Aveiro).

This work was funded by the Project Pest-C/CTM/LA 25/2013: "I3N", by FEDER funds through the COMPETE 2020 Programme and National Funds through FCT, for research fellowships BI/UI96/6642/2013 and BI/UI96/6642/2016.

This work was also funded by European project SIRBATT: "Stable Interfaces for Rechargeable Batteries" (FP7-ENERGY-2013, grant agreement No. 608502) and by the project POCI 01-0145-FEDER-016414 PAC: FIBR3D, cofinanced by POCI and Programa Operacional Regional de Lisboa, through FEDER, for the research fellowships BI/UI96/6642/2014 and BI/UI96/6642/2018, respectively.

o júri

presidente

Professor Doutor Carlos Fernandes da Silva
Professor Catedrático, Universidade de Aveiro

Professor Doutor João de Lemos Pinto
Professor Catedrático, Universidade de Aveiro
(Orientador)

Doutor Henrique Leonel Gomes
Professor Associado Com Agregação, Universidade do Algarve

Doutor António Miguel Lino Santos Morgado
Professor Auxiliar, Universidade de Coimbra

Doutora Carla Alexandra Monteiro da Silva
Professora Auxiliar, Universidade de Lisboa

Doutor Paulo Fernando da Costa Antunes
Equiparado a Investigador Auxiliar, Universidade de Aveiro

Aos meus pais, irmão e avós

Ao meu afilhado Rafael e sobrinho Miguel

À Daniela Lopes

"Enquanto não alcances, não descanses.

De nenhum fruto, queiras só metade."

Miguel Torga

agradecimentos

A realização do trabalho apresentado nesta Tese não seria possível sem a colaboração de algumas pessoas, a quem quero deixar gravado o meu mais sincero OBRIGADO!

Agradeço em particular aos meus orientadores. Ao Professor João de Lemos Pinto por me ter proporcionado a oportunidade da realização deste trabalho e pelo incentivo, desafiando-me sempre a fazer mais e melhor. À Doutora Marta Ferreira pela incansável ajuda, disponibilidade, apoio, incentivo e conselhos prestados, e ainda pela confiança sempre demonstrada, sem os quais, tudo se tornaria muito mais complicado e difícil.

Grato também estou aos colegas de laboratório, Mestre Susana Novais, Mestre Tiago Paixão, Doutor Paulo Antunes, Doutora Cátia Leitão, Doutora Nélia Alberto, Doutora Fátima Domingues e Doutor Carlos Marques pela ajuda e disponibilidade prestada ao serem parte integrante da realização deste trabalho e pelos bons momentos passados.

Gostaria de agradecer ao projeto Europeu SIRBATT, pelo financiamento concedido, tornando possível a realização de alguns dos testes experimentais e de short missions no âmbito desta Tese. Agradecer ainda aos elementos do consórcio do projeto Europeu SIRBATT, com os quais tive a oportunidade e felicidade de trabalhar pessoalmente, Doutor Stephan Koch, Doutor Lorenzo Grande, Doutor Markus Ding, Professor Doutor Stefano Passerini e Doutor John Fergie, pelos conhecimentos e ensinamentos fornecidos sobre a área das baterias de ião de lítio e pela ajuda disponibilizada na realização de alguns dos testes experimentais presentes neste trabalho. Assim como, ao Helmholtz Institut Ulm e à empresa Jonhson Mattey Battery Systems pelo acolhimento e suporte prestado.

À Fundação para a Ciência e Tecnologia e ao Instituto de Nanoestruturas, Nanomodelação e Nanofabricação por também tornarem financeiramente viável este trabalho. Ao Departamento de Física e Instituto de Telecomunicações da Universidade de Aveiro, pelas condições de acolhimento proporcionadas no desenvolvimento desta Tese.

A todos os professores com os quais tive a oportunidade de me cruzar ao longo destes anos, pelos ensinamentos facultados e a todo o staff do Departamento de Física pelas mais diversas ajudas técnicas prestadas.

Aos também meus amigos, Diana Lopes, Maximiliano Castro, Maria João Gonzalez, Pedro Casas, Ana Pedrosa, Júlio Santos, Vânia Pôjo, Rui Coelho e Gonçalo Castro pelo apoio, momentos de felicidade e amizade proporcionados.

Especial agradecimento à Daniela Lopes, pelo carinho, amizade e acima de tudo pelo sincero amor demonstrado ao longo desta feliz caminhada que estamos a traçar juntos.

Sobretudo aos meus pais pela ajuda, orgulho e amor.

palavras-chave

Rede de sensores, redes de Bragg em fibra, cavidades de Fabry-Perot, monitorização *in-situ*, deformação, mapeamento térmico, baterias de ião de lítio, segurança

resumo

No presente trabalho, desenvolveram-se redes de sensores em fibra ótica para integrar em baterias comerciais de ião de lítio (cilíndricas e prismáticas) e em baterias pré-fabricadas em ambiente de laboratório (*pouch cells*), com o objetivo de monitorizar *in situ*, em funcionamento e em tempo real variações internas e externas de temperatura e deformação, sob diferentes condições ambientais e diferentes taxas de carga e descarga.

Para tal, e de maneira a mostrar o melhor desempenho dos sensores de fibra ótica em relação aos eletrónicos tipicamente usados neste tipo de aplicação, os seus tempos de resposta e resolução foram comparados, obtendo-se uma melhoria de 28% do tempo de resposta e uma resolução superior com os sensores em fibra ótica.

Foram feitos estudos da monitorização de variações de temperatura e deformação através de redes de Bragg em fibra (FBG) na configuração cilíndrica e variações de temperatura e deformação bidirecional na configuração prismática, aquando do seu funcionamento em condições normais e abusivas, através do método FBG *strain-free.* Quando as baterias foram submetidas a condições operacionais abusivas, ficou evidente que ocorrem maiores variações de temperatura e de deformação, sendo promovidas pelo rápido transporte dos iões de lítio entre os elétrodos positivo e negativo. Devido à expansão térmica dos materiais que compõem a bateria, a sua estrutura interna é um importante parâmetro a ter em consideração e que pode influenciar o seu comportamento em termos de expansão e contração.

A fim de monitorizar o desempenho térmico de baterias prismáticas de ião de lítio em diferentes condições ambientais, realizaram-se estudos nos quais a bateria operou sob diferentes taxas de descarga em diferentes condições de temperatura e humidade relativa, por forma a simular o desempenho da bateria em três climas distintos: frio, temperado e seco. Destes estudos, constatou-se o fraco desempenho deste tipo de baterias no clima frio, e consequente inferior desempenho térmico.

Uma rede de 37 sensores FBG foi ainda usada para monitorizar as interfaces de um *pack* de 3 baterias poliméricas de lítio, conectadas em série. Foi possível realizar um mapa térmico espacio-temporal para diferentes taxas de descarga, e identificar as zonas mais suscetíveis ao aparecimento de pontos quentes e capazes de colocar em risco o seu normal funcionamento. As zonas mais quentes foram detetadas próximas dos coletores de corrente, devido à superior densidade dos iões de lítio nesta região.

Pela primeira vez, foi realizada a discriminação simultânea de variações internas de temperatura e deformação em baterias de ião lítio na configuração *pouch cell*, através da incorporação de sensores híbridos, que combinam as características operacionais dos sensores Fabry-Perot e FBG. A evolução da deformação e temperatura foi seguida pelos sensores propostos e as maiores variações de deformação foram detetadas no início do processo de descarga, na posição inferior da *pouch cell*.

Com o trabalho desenvolvido nesta Tese, conclui-se que a integração de sensores em fibra ótica em baterias de ião de lítio contribui para um melhor conhecimento, interno e externo, do desempenho térmico e de variações de volume sob diferentes condições de funcionamento. Assim, poder-se-á melhorar as condições de segurança e otimizar o *design* da próxima geração de baterias de ião de lítio.

keywords

Sensors network, fiber Bragg gratings, Fabry-Perot cavities, *in-situ* monitoring, strain, thermal mapping, lithium-ion battery, safety.

abstract

In this work, fiber optic sensor networks were developed to be integrated in commercially available lithium-ion batteries (cylindrical and prismatic) and pre-fabricated batteries in a laboratory environment (pouch cells), with the objective of monitoring in situ, operando and in real time, the internal and external variations of temperature and strain, under different environmental conditions and different charge and discharge rates.

To this end, and in order to show the improved performance of fiber optic sensors in relation to the electronic ones, typically used in this type of application, their response time and resolution were compared. An improvement of 28% of the response time and a better resolution are attained with fiber optic sensors.

Monitorization studies of the temperature and strain variations using fiber Bragg gratings (FBGs) in the cylindrical configuration have been made, as well as temperature and bi-directional strain variations in the prismatic configuration, under normal or abusive operating conditions, using the FBG method strain free. When the batteries were subjected to abusive operating conditions, it was evident that greater temperature and strain variations occur, being promoted by the rapid transport of lithium ions between the positive and negative electrodes. Due to the thermal expansion of the materials that compose the battery, its internal structure is an important parameter to consider and that can influence its behavior in terms of expansion and contraction.

In order to monitor the thermal performance of lithium-ion prismatic batteries in different environmental conditions, studies were performed in which the battery operated at different discharge rates over different conditions of temperature and relative humidity, in order to simulate the performance of the battery in three distinct climates: cold, temperate, and dry. From these studies, the poor performance of this type of batteries in the cold climate, and consequent lower thermal performance was verified.

A network of 37 FBG sensors has also been used to monitor the interfaces of a pack of 3 lithium polymer batteries connected in series. It was possible to perform a spatial and temporal thermal mapping under different discharge rates, and to identify areas that are more susceptible to the appearance of hot spots and that are capable of endanger its normal functioning. Hotter zones were detected near the current collectors, due to the higher density of lithium ions in this region.

For the first time, the simultaneous discrimination of internal temperature and strain variations in lithium-ion batteries in the pouch cell configuration was carried out, through the incorporation of hybrid sensors, which combine the operational characteristics of the Fabry-Perot and FBG sensors. The evolution of the strain and temperature signals was followed by the proposed sensors and the largest strain variations were detected at the beginning of the discharge process, in the bottom position of the pouch cell.

With the work developed in this Thesis, it is concluded that the integration of optical fiber sensors into lithium-ion batteries contributes to a better internal and external knowledge of the thermal performance and volume variations under different operating conditions. This might improve the safety conditions and optimize the design of the next generation of lithium-ion batteries.

Acronyms

AC	Air conditioning
BMS	Battery management system
BOC	Beginning of charge
BOD	Beginning of discharge
C	Charge
CC	Constant current
CO	Carbon monoxide
CO_2	Carbon dioxide
CV	Constant voltage
D	Discharge
DAQ	Data acquisition system
EOC	End of charge
EOD	End of discharge
ER	Electrical resistivity
FBG	Fiber Bragg grating
FP	Fabry-Perot
LFP	Lithium iron phosphate
Li	Lithium
Li^+	Lithium ions
LIB	Lithium-ion battery
LiPB	Lithium polymer battery
$LiPF_6$	Lithium hexafluorophosphate
M	Determinant of the matrix coefficient
MMF	Multimode fiber
PLA	Polylactic acid
R	Rest
RH	Relative humidity
SEI	Solid electrolyte interface
SHM	Structural health monitoring
SMF	Single mode fiber

SOC	State of charge
SOH	State of health
TC	Thermocouple
UV	Ultraviolet

Symbols

α	Thermal expansion coefficient
α_{al}	Thermal expansion coefficient of aluminum
δ_{FP}	FP phase difference
ΔD	Displacement variation
$\Delta\varepsilon$	Strain variation
ΔL	Length variation
$\Delta\lambda$	Wavelength variation
$\Delta\lambda_{FBG}$	FBG wavelength shift
$\Delta\lambda_{FP}$	FP wavelength shift
ΔT	Temperature variation
k	Sensitivity
k_ε	Strain sensitivity
k_T	Temperature sensitivity
$k_{FBG\varepsilon}$	FBG strain sensitivity
k_{FBGT}	FBG temperature sensitivity
$k_{FP\varepsilon}$	FP strain sensitivity
k_{FPT}	FP temperature sensitivity
Λ	Grating period
λ_B	Bragg wavelength
λ	Wavelength
n	Refractive index
n_{eff}	Effective refractive index
R_1	Reflecting component 1
R_2	Reflecting component 2
R^2	Determination coefficient
ρ_e	Photo-elastic constant of the fiber
ζ	Thermo-optic coefficient

Table of contents

Chapter I: General introduction

Chapter II: Real time thermal monitoring of lithium batteries with fiber sensors and thermocouples: A comparative study

Chapter III: Lithium batteries temperature and strain fiber monitoring

Chapter IV: Simultaneous sensing of temperature and bi-directional strain in a prismatic Li-ion battery

Chapter V: Temperature fiber sensing of Li-ion batteries under different environmental and operating conditions

Chapter VI: Thermal mapping of a lithium polymer batteries pack with FBGs network

Chapter VII: Internal strain and temperature discrimination with optical fiber hybrid sensors in Li-ion batteries

Chapter VIII: Final remarks and future developments

List of figures

List of tables

Chapter I

General introduction

1. Introduction

The sensing of characteristic parameters, such as temperature and strain variations, in lithium-ion batteries (LIBs) is a fundamental issue to ensure that they operate in safe conditions. Typically, LIBs are monitored through electronic sensing devices, such as thermocouples, micro-electro-mechanical systems, pyrometers, and resistance temperature sensors. However, in addition to low resolution and accuracy, these sensors are not suitable to be embedded in LIBs, due to the electrochemical environment of the battery. Alternative solutions, with higher precision, multipoint capabilities, reduced the system costs, and that can be easily integrated in LIBs with low invasiveness, are the fiber optic sensors.

1.1 Fiber optic sensors

Manfred Börner, a German physicist, developed in 1965 the first fiber optic patent related with a working fiber-optic data transmission system [1, 2]. Years later, in 1978, the concept of wavelength division multiplexing, where several optic signal chargers are multiplexed into a single optical fiber through different wavelengths was firstly published [3]. Since then, the optical fiber community has expanded and the use of optical fibers as sensing elements attracted a lot of attention. Figure I.1 summarizes the different types of fiber optic sensors developed along the last years [4]. The fiber Bragg gratings (FBGs) and Fabry-Perot (FP) interferometers were the type of sensors selected to be used in the works reported in the present Thesis.

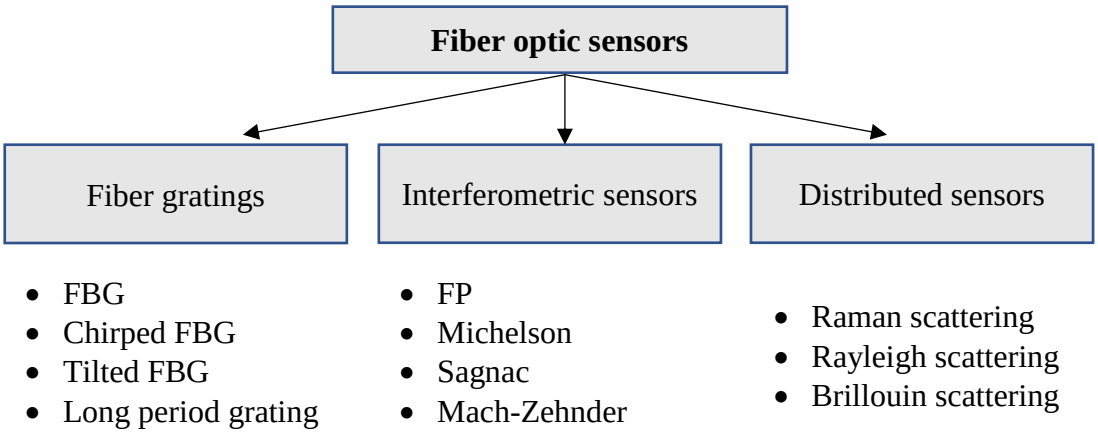

Figure I.1. Types of fiber optic sensors (adapted from [4]).

The first FBG, fabricated using a visible laser propagating along the fiber core, was proposed by Ken Hill, also in 1978 [5]. Fiber optic sensors based on FBGs have been widely applied in the measurement of physical, chemical, biomedical, and electrical parameters, especially for structural health monitoring (SHM) in civil infrastructures, aerospace, energy, and maritime areas [6]. Typically, the measurands information is usually encoded by the Bragg wavelength shift.

In 1897, Charles Fabry and Alfred Perot, published the first paper describing the so-called FP interferometer principle [7]. In the last four decades, fiber optic sensors based on this interferometric method were also applied in numerous applications, such as mechanical, biological, chemical, and various physical parameters including temperature, strain, pressure, and refractive index [4, 8].

Optical fibers have been intensively investigated at various sensor fields owing to their unique characteristics such as multiplexing, remote sensing, high flexibility, low propagating loss, high sensitivity, low fabrication cost, high accuracy, durability, simultaneous sensing ability, and immunity to electromagnetic interference [7-10].

1.1.1 Fiber Bragg gratings

The sensing principle of a FBG is based on a local modulation of the refractive index in the optical fiber, which can be created by using an appropriate sideways illumination with UV-light (spatial fringe pattern) to a photo-sensitive optical fiber. Figure I.2 shows the scheme of a FBG sensor together with a typical FBG writing scheme [4, 6].

Strain and temperature measurements with FBGs are the most common sensing applications. Despite that the values are dependent on FBG types and the operation wavelength, their typical sensitivity to temperature and strain is of ~13.0 pm/°C and ~1.2 pm/με, respectively [10]. In addition to the common advantages of fiber sensors, this wavelength interrogation method provides robustness to noise and power fluctuation and also enables wavelength division-multiplexing, by inscribing several FBGs with different grating periods in the same optical fiber. This allows the monitorization of different positions in one structure/surface with only one sensor line. In practice, both the effective refractive index and the Bragg period of the grating will be affected by any applied mechanical strain as well as by temperature

[11]. They can be easily embedded into composite materials due to their small dimensions, higher flexibility, and higher heat and stress resistance [11-13].

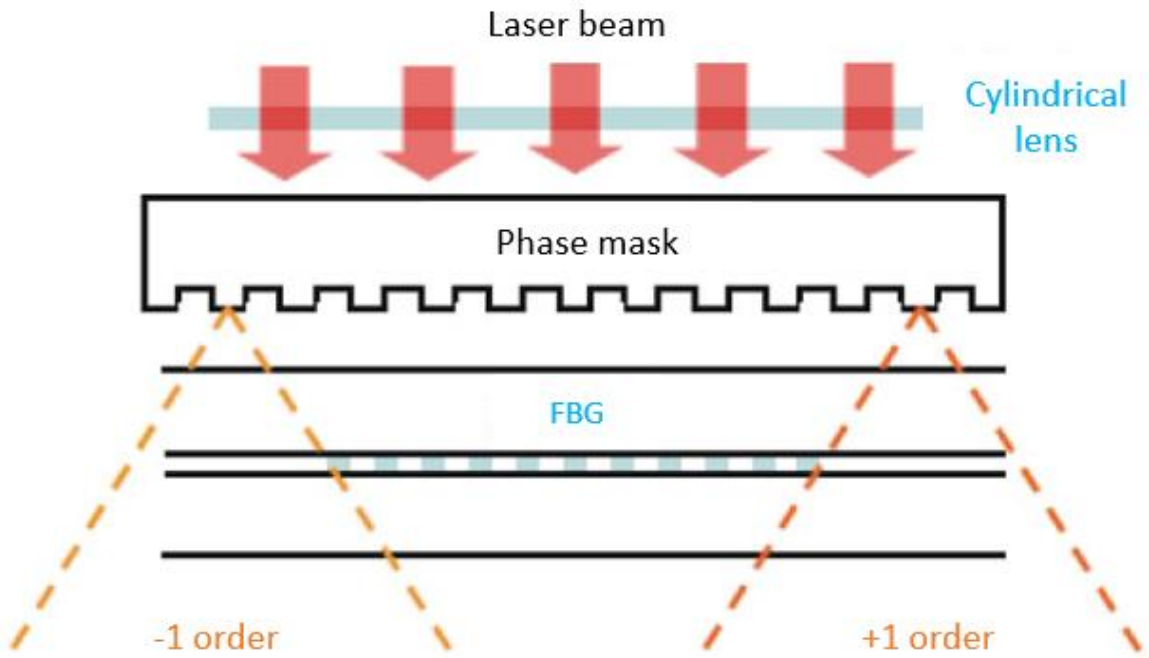

Figure I.2. Schematic process of phase mask technique for the fabrication of FBG sensors in the fiber (adapted from [4, 6]).

1.1.2 Networking of FBGs

In recent years, the research and development of sensor network technology based on FBGs has attracted significant interest, because the wavelength of an individual FBG sensor is able to carry the measurand information in a specific position. Since some tested objects contain more than one measurement point and sometimes have a continuous distribution of temperature and/or strain, the use of multiplexed sensing technology to build up the sensor networks is indispensably required, in order to obtain a complete information of tested objects. By addressing wavelength division, one can acquire the information of different locations along the fiber axis. Only one light source is required, and the same interrogation system is employed for different FBGs, which effectively decreases the system cost [14]. In many applications, when competing with other mature sensing technologies, such as the electronic sensors, the FBGs have proven to be a better solution [14, 15].

1.1.3 Fabry-Perot interferometers sensors

In an interferometric sensor, such as the FP interferometer, a physical change in the structure causes a phase change of the two interfering light signals [16]. A FP cavity sensor is designed by considering two parallel reflecting surfaces separated by a certain length (L). FP sensors can be classified as extrinsic or intrinsic, as can be seen in Fig. I.3 a) and b), respectively. In an extrinsic FP interferometric sensor, the air cavity is formed by a supporting structure. The intrinsic FP interferometric fiber sensor has reflecting components within the fiber itself [17,18].

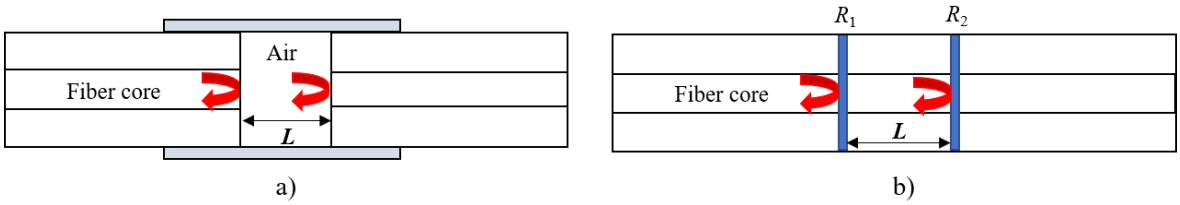

Figure I.3. a) Extrinsic FP sensor performed by forming an external air cavity, and b) intrinsic FP sensor formed by two reflecting components, R_1 and R_2 (adapted from [7]).

A FP sensor can achieve a maximum strain resolution of 0.15 με. The typical measurement range is ~1000 με, which can be extended up to ~5000 με [4]. It can be operated at larger scale of temperatures (-50 °C – 1000 °C) [19, 20], and it is very compact, with a length from few tens of micrometers up to several millimeters. These sensors can also be embedded into the materials without any weight penalty or adverse effects [16, 21].

1.1.4 Simultaneous discrimination of strain and temperature

FBGs are sensitive to more than one physical parameter at the same time, translating in a large cross sensitivity, such as in the case of strain and temperature. Many procedures have been proposed to simultaneously discriminate strain and temperature. The most straightforward way is using two different FBGs, whereupon one FBG is strain-free and the other simultaneously detects strain and temperature. However, this method can be challenging when it is proposed to monitor specific parameters inside electrochemical materials, such as batteries, due to the necessity of involving the strain-free FBG sensors in other conductive materials. Typically, conductive microtubes are used, at the cost of

increasing the invasiveness and the possibility of interacting with the electrochemical materials.

Other methods are based on the use of different sensing elements that have different responses to strain and temperature. For example, methods have been reported that use an FBG pair [22], a chirped FBG [23], or cascading an FBG with a thermochromic material coated fiber tip [24]. All these methods have good response to strain and temperature, however, they are inappropriate for precise measurements due to low spatial resolution. FBGs have also been recorded in high birefringence [25] or doped [26] fibers, however they require a fiber laser system for demodulation.

FP sensors based on air cavities are typically used to monitor strain or pressure variations due to the fact that they are almost insensitive to temperature shifts [27, 28]. Nevertheless, and like the FBGs, when embedded inside materials, their sensitivity to temperature and strain changes due to the mechanical stresses produced by the surrounding material, and an internal calibration is always required [29, 30].

The simultaneous discrimination of strain and temperature can be improved by combining the signals of FBGs and FPs, by writing the FBG sensor as near as possible to the FP cavity. The main advantages of this process are the different strain and temperature sensitivities obtained by the FP cavities comparatively with the FBGs, together with the benefit of using a single fiber to monitor the same point, decreasing the invasiveness inside the battery. Besides, no extra-material is needed to be integrated with this discrimination method.

1.2 State of art – Lithium-ion batteries

Lithium is named after the Greek word "*lithos*" meaning "stone". The soft, silver-white metal belongs to the alkali metal group of chemical elements and is noticeable with the symbol Li. Lithium is the lightest of all metals, has the greatest electrochemical potential and provides the largest specific energy per weight.

In 2016, the total demand for lithium reached almost 120.000 metric tons. Figure I.4 presents typical uses of lithium, which include lubricants, glass, ceramics, pharmaceuticals and refrigeration [31, 32]. According to this graph, batteries consume 39% of the largest share of lithium.

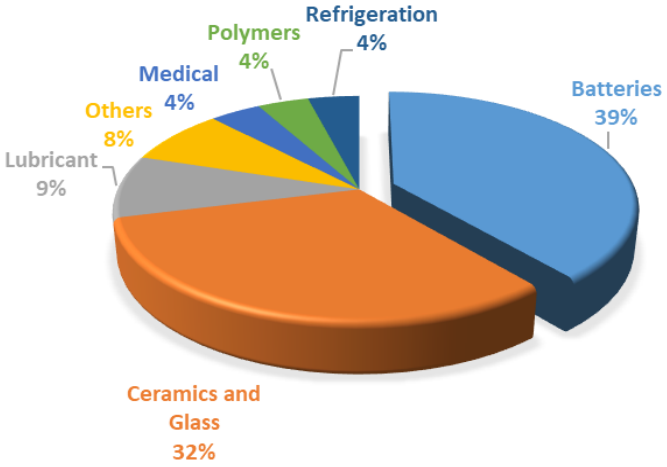

Figure I.4. Distribution of global lithium end-uses at various sectors for different application (2016) (adapted from [31]).

In 1991, Sony commercialized the first LIB, and today the batteries based on this chemistry have become the most promising and fastest growing technologies on this specific market. The key to the superior specific energy is the high nominal cell voltage of 3.60 V, that can directly power mobile phones, tablets and digital cameras, offering simplifications and cost reductions over multi-cell designs. The main drawback is the need of protection circuits to prevent abuse [33].

Most LIBs share a similar design, as illustrated in Fig. I.5, consisting on a metal oxide positive electrode (cathode) that is coated onto an aluminum current collector, a negative electrode (anode) made from carbon/graphite coated on a copper current collector, a separator, and an electrolyte made of lithium salt in an organic solvent. During the charge process, the ions flow from the cathode to the anode through the electrolyte and separator. The discharge process reverses the direction and the ions flow from the anode to the cathode [34].

Commercially available Li-ion cells use polyolefin as a separator, which is moistened with electrolyte and forms a catalyst that promotes the movement of ions. Although ions pass freely between the electrodes, the separator is an isolator with no electrical conductivity [35, 36]. The separator should be as thin as possible to not add dead volume and still provide sufficient tensile strength to prevent stretching during the winding process and offer good stability throughout life. The pores must be uniformly spread on the sheet to ensure even

distribution throughout the entire separator area. Furthermore, the separator must be compatible with the electrolyte and allow easy wetting. Dry areas can create hot spots through elevated resistance, leading to cell failure [33, 37].

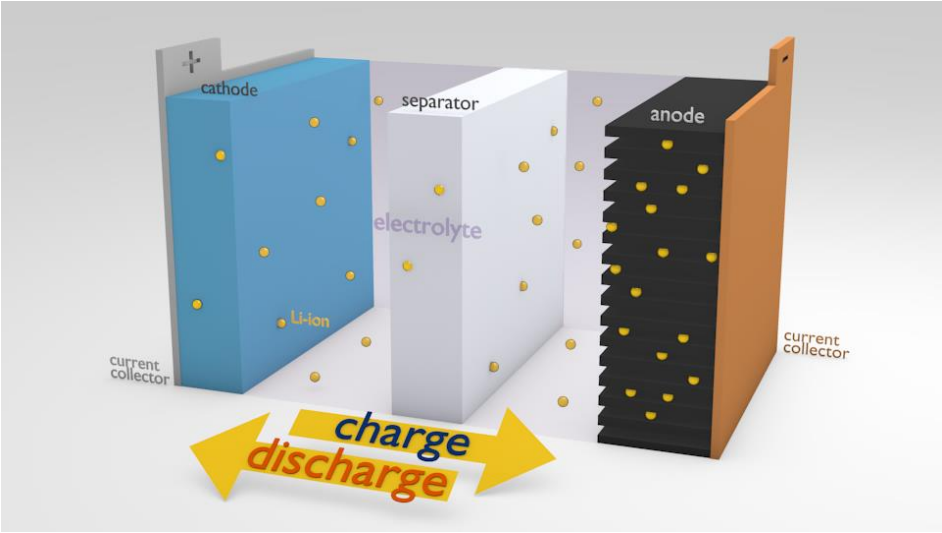

Figure I.5. Ion flow through the LIB separators. These provide a barrier between the anode (negative electrode) and the cathode (positive electrode) while enabling the exchange of lithium ions from one side to the other (adapted from [34]).

The electrolyte serves as catalyst to make the battery conductive by promoting the movement of ions. LIBs can use liquid, gel or dry polymer electrolytes. Ideally, the electrolyte should be stable, but this is not the case with the LIBs. When the LIB is activated for the first time, a passivation film forms on the anode, the so-called solid electrolyte interface (SEI). This layer separates the anode from the cathode but allows ions to pass through much like a separator. In essence, the SEI layer must form to enable the battery to work. The film stabilizes the system and gives the LIB a long life, but this causes a capacity reduction [38, 39].

In addition to the many different alternative LIB chemistries, there is also the possibility to design the battery in different ways. One way is to use large sheets of the anode-cathode combinations, that are layered, cut into a square shape and then stacked. Afterwards, they are enclosed in protective containers; either a flexible pouch cell (aluminum and plastic laminate) or a hard aluminum case (prismatic cell). Another possibility is to use a

combination between the anode and cathode stacked in large sheets and rolled up to form the many layered structure. The roll is cut to the desired length and inserted into a cylindrical container, often of aluminum [37]. The different ways of configurations and that were used in the experimental tests of this Thesis, are presented in the Fig. I.6.

The cylindrical batteries configuration is one of the most widely used packaging styles. The advantages are the ease of manufacture and good mechanical stability. This LIB configuration has good cycling ability, offers a long calendar life and is economical, but it is dense, and it has low packaging density due to the internal space cavities. The 18650 cylindrical battery (18mm in diameter and 65 mm the length) remains one of the most popular cell packages, where the typical applications are power tools, medical devices, gadgets, and electric bicycles [40].

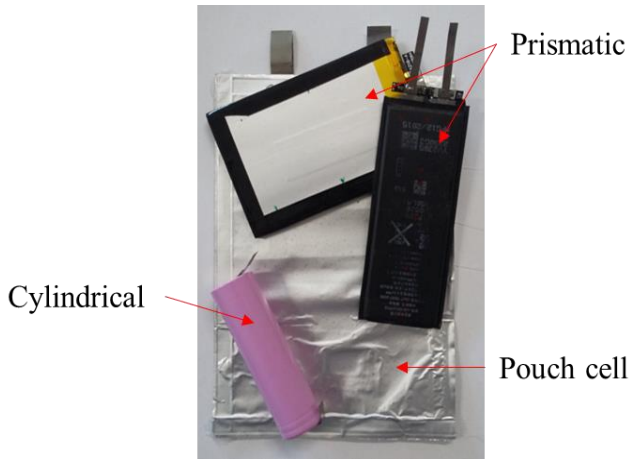

Figure I.6. Photograph of a cylindrical, prismatic and pouch cell LIB configurations.

Introduced in the early 1990s, the prismatic LIB, presented in Fig. I.7, satisfies the demand for thinner sizes. Wrapped in elegant packages, the prismatic batteries make optimal use of space by using the layered approach forming a jelly-roll structure, and are predominantly found in mobile phones, tablets, and low-profile laptops ranging from 800 mAh to 4000 mAh. They are also available in large formats. Packaged in welded aluminum housings, the cells deliver capacities of 20-50 Ah and are primarily used for electric power trains in hybrid and electric vehicles [40]. The prismatic cell improves space utilization and allows flexible design, but it can be more expensive to manufacture, less

efficient in thermal management and have a shorter life cycle than the cylindrical design. This type of cells requires a firm enclosure to achieve compression. Some swelling due to gas buildup is normal, and growth allowance must be made [40].

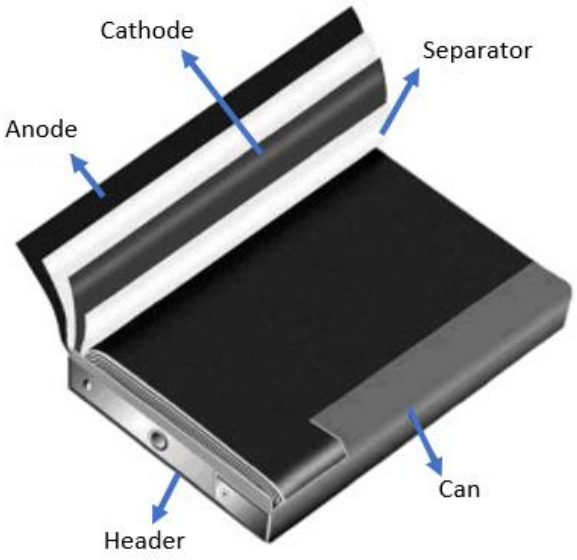

Figure I.7. Cross section of a prismatic LIB (adapted from [40]).

The pouch cell configuration, shown in Fig. I.8, surprised the battery world with a radical new design. Rather than using a metallic cylinder and glass-to-metal electrical feed-through, conductive foil-tabs were welded to the electrodes and brought to the outside in a fully sealed way [41]. This configuration offers a simple, flexible and lightweight solution to battery design.

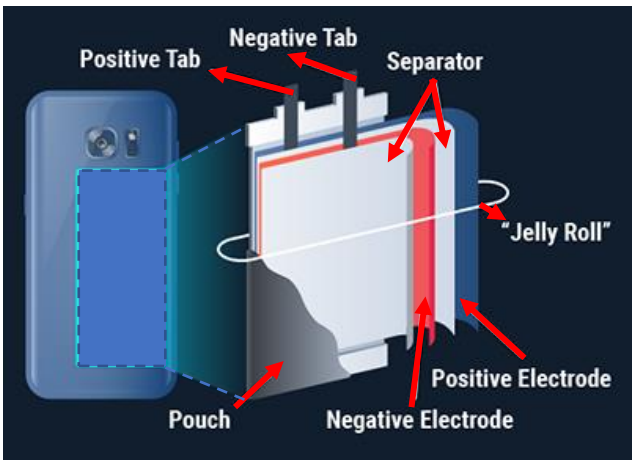

Figure I.8. Li-ion pouch cell used in a cell phone (adapted from [41]).

The Li-ion pouch cells can deliver high load currents, but they perform best under light loading conditions and with moderate charging. They make most efficient use of space and achieve 90 - 95 % packaging efficiency, the highest among battery packs. They are typically used in consumer, military, and automotive applications. No standardized pouch cells exist, and each manufacturer designs its own [40, 41].

Extreme swelling in Li-ion pouch cells, as illustrated in Fig. I.9, is currently a concern. It is best not to stack pouch cells on top of each other but to lay them flat, side by side or to allow extra space between them. The pressure created can crack the battery cover, and in some cases, break the display and electronic circuit boards. The swelling can occur due to gas generation, also known as gassing, that contain mainly CO_2 and CO [33, 42].

Figure I.9. Swollen Li-ion pouch cell (adapted from [42]).

Subsequent charges should produce minimal gases, however, gassing, cannot be fully avoided. It is caused by electrolyte decomposition as part of usage and aging. Stresses, such as overcharging and overheating also promote the gas generation [39].

1.3 Temperature and strain LIBs performance

As can be seen in Table I.1, LIBs can operate over a wide temperature range. However, the charging process is more delicate than discharging and special care must be taken. Extreme cold and high heat reduce charge acceptance, so the battery must be brought to a moderate temperature before charging. LIBs perform well at elevated temperatures however, prolonged exposure to heat decreases longevity. Charging and discharging at elevated

temperatures can cause gas generation that might cause a cylindrical cell to vent and a pouch cell to swell.

Table I.1. Acceptable charge and discharge temperatures of rechargeable LIBs.

Charge temperature / °C	Discharge temperature / °C	Comments
0 to 45	-20 to 60	No charge permitted below freezing. Good charge/discharge performance at higher temperature but shorter life.

LIBs can be fast charged from 5 °C to 45 °C. Below 5 °C, the charge current should be reduced, and no charging is permitted at freezing temperatures because of the reduced diffusion rates on the anode. During charge, the internal cell resistance causes a slight temperature rise that compensates for some of the cold. The internal resistance of all batteries rises when cold, prolonging charge times noticeably [38, 43].

Although the pack appears to be charging normally, plating of metallic lithium can occur on the anode during a sub-freezing charge. This is permanent and cannot be removed with cycling [44-46]. Cold temperature increases the internal resistance and lowers the capacity. A battery that provides 100 % capacity at 27 °C will typically deliver only 50 % at -18 °C [46]. The driving range of an electric vehicle between charges is calculated at ambient temperature. Electrical vehicles drivers are being made aware that frigid temperature reduces the available mileage. This loss is not only caused by heating the cabin electrically but by the inherent slowing of the battery's electrochemical reaction, which reduces the capacity while cold [47, 48]. Fundamentally, the poor performance of LIBs at lower temperatures arises from sluggish kinetics of charge transfer [49, 50], low electrolyte conductivity [35, 51], and reduced solid-state lithium diffusivity [49, 52].

The primary challenge in designing a scaled-up LIB system is to guarantee safety in normal and under abuse operating conditions. Thermal and pressure stability of LIBs are the most important parameters for safety [53]. This type of batteries is exothermic, causing fast temperature increase, when operated under abnormal conditions [44]. Excessive heat generated during charge and discharge at high current (e.g., during overcharge/discharge and in the presence of short circuits) can cause the appearance of hot spots and eventually lead

to their explosion and combustion as a result of the rapid increase of internal temperature and pressure [54].

Bandhauer *et al.* stated in their critical review of thermal issues in LIBs that the main barriers to the deployment of large fleets of vehicles on public roads equipped with LIBs continue to be safety, cost (related to cycle and calendar life), and low temperature performance - all challenges that are coupled to thermal effects in the battery [38]. In order to develop a sufficient thermal management strategy, it is essential to know internal and external cell parameters during operation. Furthermore, it is important to know the cold and hot spots inside the cell during all operating states for online diagnostic analysis [55, 56].

In LIBs, the chemistry of the active materials alters during the charge/discharge processes, promoting strains in electrode particles and changes in the electrode volume. This volume variation is caused by Li^+ intercalation into host materials, like graphite and lithium transition metal oxide and resultant lattice expansion and contraction [53, 57]. The LIB stability and safety can be affected by these induced strains, being the principal cause of material failure and other forms of performance degradation [58].

Effective control and management of cell charge and discharge by battery management systems (BMS) is essential for good performance. Current BMS rely on monitoring conventional external parameters such as voltage, current and external temperature, to estimate state of charge (SOC) and state of health (SOH). However, the information provided by such parameters is limited and can compromise the estimation accuracy of both SOC and SOH. Furthermore, it contributes to over-conservative usage and over-engineering of a battery pack [57, 58].

Using the information of additional parameters such as internal temperature or strain has the potential to improve SOC/SOH estimation accuracy, which in turn can lead to optimal battery-pack design and capacity utilization. However, the available options to sense these internal parameters are limited by the corrosive and electrically noisy environment of batteries, which makes the internal sensing a challenge.

The optimized design of a LIB management system needs firstly to solve questions in terms of inherent safety under both normal and abuse operating conditions, being correlated with strain and temperature monitoring. The ability to quantify and evaluate the variation in strain and heat generated during the electrochemical processes that the batteries can operate

will be crucial information regarding their behavior as well as an active tool to promote their safety [43, 44]. Fiber optic sensors, due to their already mentioned advantages and attributes, are attractive candidates for reliable state monitoring in LIBs.

1.4 Different environmental conditions: Köppen classification

The climate zone where the battery operates plays an important role in its behavior. Climate, in a narrow sense, is usually defined as the "average weather", or more rigorously, as the statistical description in terms of the mean and variability of relevant quantities over a period of time ranging from months to thousands or millions of years. The classical period is 30 years, as defined by the World Meteorological Organization [59]. These quantities are most often surface variables such as temperature, precipitation, humidity, and wind [60, 61]. The climate classification system most widely used depends on the average monthly values of temperature and precipitation and it was proposed in 1900 by Wladimir Köppen [55]. There are five primary climate types, labeled from A to E, which are distributed worldwide according to Fig. I.10. These climate types are described as follows [60-62]:

A- Tropical - Tropical climates are known for the high temperatures year-round and for the large amount of year-round rain. The average temperature is about 27 °C. The temperatures feel hotter because the humidity is usually very high, between 77 and 88 %RH.

B- Dry - Dry climates are characterized by little rain and a huge daily temperature range. Summer has the average temperature is about 35 °C and humidity of 20 %RH. In the winter, the average temperature is of 15 °C and the humidity is of 50 %RH.

C- Temperate - These climates have warm, dry summers and cool, wet winters. The average monthly temperature is above 24 °C, with the average humidity of 50 %RH in the warmest months and in the coldest months, the average temperature is above 10 °C and the humidity of 80 %RH.

D- Cold - Cold climates can be found in the interior regions of large land masses. Total precipitation is not very high and seasonal temperatures vary widely. These climates have an average temperature above 18 °C and humidity of 65 %RH in their warmest months, and a coldest month average below -5 °C with humidity of 75 %RH.

E- Polar - These climates are part of areas where ice and tundra are always present. Only about four months of the year have temperatures above the freezing point. These climates are characterized by average temperatures of -5 °C in the summer and -15 °C in the winter with humidity of 80 %RH in both seasons.

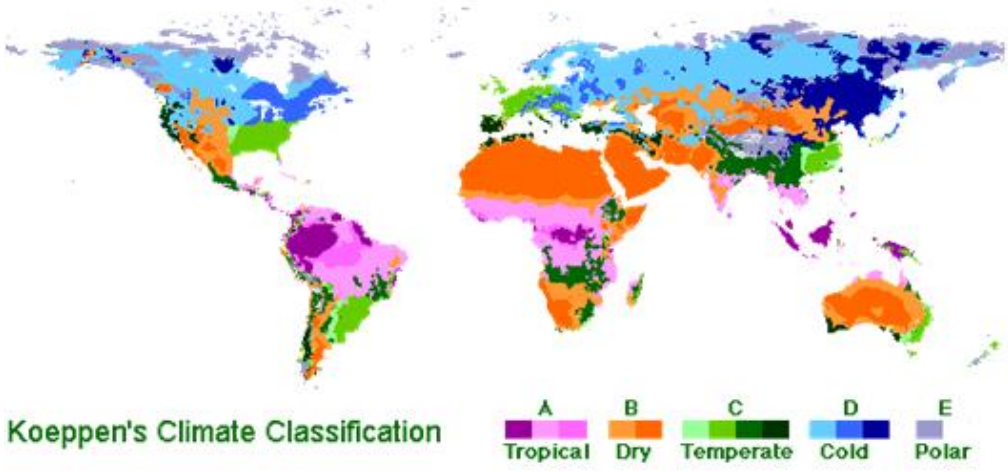

Figure I.10. Köppen climate classification (adapted from [61]).

2. Goals and Thesis structure

As previously mentioned in this introductory Chapter, the sensing of characteristic parameters, such as temperature and strain variations in LIBs seems to be an essential issue to ensure their operation in safe conditions. In this Thesis, this matter is addressed by proposing new sensing networks based on FBGs to study, monitor, and quantify multipoint temperature and strain variations in different configurations of LIBs (cylindrical, prismatic, and pouch cell). The studies comprised both external and internal monitoring; during normal and abusive operating conditions, i.e. under different environments and charges/discharges C-rates.

The optical sensors responses were compared with electronic devices, namely K-type thermocouples; and a sensing network of FBG sensors was performed to spatial and temporal thermal mapping the interfaces of a LiPBs pack. The simultaneous discrimination of internal temperature and strain variations in a LIB pouch cell configuration was achieved by employing a hybrid sensor, that combined the operational characteristics of both FBG and

FP interferometer sensors. These specific objectives are addressed in the present Thesis along eight Chapters, described below:

[Chapter I] In this Chapter, a general introduction is provided. It consists of a brief contextualization of the thematic approach of this Thesis, relatively to the utilization of an optical fiber sensors network to monitor characteristic parameters of interest in different configurations of LIBs, to improve their use in safe conditions.

[Chapter II] In Chapter II, the main objective is to compare the response of optical and electronic sensors regarding the real time monitoring of LIB surface temperature variations. Three different positions of a rechargeable prismatic LIB are considered, and constant current charge and different discharge rates are tested.

[Chapter III] The objective of this Chapter is to evaluate the outcome of the real-time monitoring of external temperature and strain variations using FBG sensors, in a rechargeable cylindrical LIB under different operating conditions.

[Chapter IV] The main goal of this Chapter is to assess, through a sensing network of FBGs, quantitative temperature and bi-directional strain shifts. The correspondent longitudinal and transversal strain variations are also provided, as a function of the respective voltage signal of a prismatic LIB, during different cycling protocols.

[Chapter V] This Chapter focuses on an optical fiber sensing network based on FBGs developed to real time, *in situ* and *operando* monitor the thermal performance in five different points of a rechargeable smartphone LIB under different environments, by applying constant current charge and different discharge rates. An analysis of the thermal performance of a LIB under different environmental conditions typical of the temperate, dry, and cold climates is presented for the first time, to the best of our knowledge.

[Chapter VI] In this Chapter, a spatial and temporal thermal mapping of the interfaces that compose a LiPBs pack is presented. For that, the temperature monitorization is performed through a sensing network of 37 FBGs during different operation cycling tests. To the best of our knowledge, this is the first time that a spatial and temporal thermal mapping is reported for this specific application, using a network of FBG sensors.

[Chapter VII] The main goal of this Chapter is to simultaneously discriminate internal strain and temperature in a Li-ion pouch cell. For that, and as a proof-of-concept, a hybrid sensing network of FBGs and FPs is preliminary tested on the surface of a smartphone

prismatic battery to discriminate external strain and temperature variations. Afterwards, the sensing network is embedded in a pouch LIB to monitor and discriminate *operando* and *in situ* internal strain and temperature shifts. Galvanostatic cycling at different C-rates are applied to correlate the variations in temperature and strain with the processes in the pouch cell. To the best of our knowledge, this is the first time that this innovative methodology is presented for this type of application.

[Chapter VIII] Final remarks. In this final Chapter, information obtained within this study is discussed in an integrated way, and future work is approached.

3. Main contributions and publications

Due to their novelty and the potential technological impact in the design and monitorization of the next generation of LIBs, the author declares that three of the works presented, stand out as main contributions. The first one is the work presented in the Chapter V, in which an analysis of the thermal performance of a LIB under different environmental conditions is presented. The second one is approached in the Chapter VI, where a spatial and temporal thermal mapping is reported for this specific application, using a network of FBG sensors. The last one, reported in Chapter VII, is about the simultaneous measurement of internal strain and temperature in a Li-ion pouch cell using a hybrid sensing network of FBGs and FPs. To the author´s knowledge, it is the first time that these topics are reported for this application using fiber-based sensors.

This Thesis allowed the publication of five papers in international journals, as first author. Besides, three works have been presented in international conferences, one of them as oral presentation. Furthermore, one other paper in international journal and one book chapter have been published as co-author.

[1] Micael Nascimento, Susana Novais, Markus Ding, Marta S. Ferreira, Stephan Koch, Stefano Passerini, and João L. Pinto. Internal strain and temperature discrimination with optical fiber hybrid sensors in Li-ion batteries. *Journal of Power Sources*, 2019, 410-411, 1-9, DOI: 10.1016/j.jpowsour.2018.10.096.

[2] Micael Nascimento, Marta S. Ferreira, and João L. Pinto. Temperature fiber sensing of Li-ion batteries under different environmental and operating conditions. *Applied Thermal Engineering*, 2019, 149, 1236-1243, DOI: 10.1016/j.applthermaleng.2018.12.135.

[3] Micael Nascimento, Tiago Paixão, Marta S. Ferreira, and João L. Pinto. Thermal Mapping of a Lithium Polymer Batteries Pack with a Network of FBGs. *Batteries*, 2018, 4(4), 67, DOI: 10.3390/batteries4040067.

[4] Micael Nascimento, Marta S. Ferreira, and João L. Pinto. Simultaneous Sensing of Temperature and Bi-Directional Strain in a Prismatic Li-Ion Battery. *Batteries*, 2018, 4(2), 23, DOI: 10.3390/batteries4020023.

[5] Micael Nascimento, Marta S. Ferreira, and João L. Pinto. Real time thermal monitoring of lithium batteries with fiber sensors and thermocouples: A comparative study. *Measurement* 2017, 111, 260 - 263, DOI: 10.1016/j.measurement.2017.07.049.

[6] Susana Novais, Micael Nascimento, Lorenzo Grande, Fátima Maria Domingues, Paulo Antunes, Nélia Alberto, Cátia Leitão, Ricardo Oliveira, Stephan Koch, Guk Tae Kim, Stefano Passerini, and João L. Pinto. Internal and external temperature monitoring of a Li-ion battery with fiber Bragg sensors. *Sensors* 2016, 16, 1394, DOI: 10.3390/s16091394.

[7] Micael Nascimento, Marta S. Ferreira, and João L. Pinto. Strain and temperature discrimination in operando Li-ion polymer batteries. 26th International Conference on Optical Fibre Sensors - OFS26, 2018, Lausanne, Switzerland, OSA Technical Digest (Optical Society of America), paper TuE41, DOI: 10.1364/OFS.2018.TuE41.

[8] Micael Nascimento, Marta S. Ferreira, and João L. Pinto. Impact of different environmental conditions on lithium-ion batteries performance through the thermal

monitoring with fiber sensors. 3rd International Conference on Applications of Optics and Photonics, *Proc. SPIE*, 2017, 10453, 104532S-1, DOI: 10.1117/12.2276331.

[9] Susana Novais, Micael Nascimento, Marta S. Ferreira, M. Fátima Domingues, Stephan Koch, Gang Yang, Stefano Passerini, and João L. Pinto. Lithium batteries monitoring with fiber Bragg gratings. Advances in Sensors: Reviews' Book Series, 5, 2018.

[10] Micael Nascimento, Susana Novais, Cátia Leitão, M. Fátima Domingues, Nélia Alberto, Paulo Antunes, and João L. Pinto. Lithium batteries temperature and strain fiber monitoring. *Proc. SPIE*, 24th International Conference on Optical Fibre Sensors - OFS24, 2015, Curitiba, Brazil, 9634, 96347V1 – 96347V4, DOI: 10.1117/12.2195218.

References

[1] Jeff Hecht. City of light: The story of fiber optics. Oxford University Press, Inc. ISBN 0-19-510818-3; 0-19-516255-2, 1999.

[2] M. Borner. Electro-optical transmission system utilizing lasers, US Patent 3,845,293, 1974.

[3] J. Minowa H. Ishio and K. Nosu. Review and status of wavelength-division-multiplexing technology and its application. *J. Lightw. Techol.* 1984, 4, 448 – 463, DOI:10.1109/JLT.1984.1073653.

[4] D. S. Raffaella. Fibre optic sensors for structural health monitoring of aircraft composite structures: Recent advances and applications. *Sensors* 2015, 15, 18666 - 18713, DOI: 10.3390/s150818666.

[5] D. C. Johnson, K. O. Hill, Y. Fujii and B. S. Kawasaki. Photosensitivity in optical fiber waveguides: Application to reflection filter fabrication. *Appl. Phys. Lett.* 2008, 32, 647, DOI: 10.1063/1.89881.

[6] W. Lutang and F. Nian. Applications of fiber-optic interferometry technology in sensor fields, Optical interferometry A. A. Banishev, M. Bhowmick and J. Wang, IntechOpen, 2017, DOI: 10.5772/66276.

[7] C. Fabry and A. Perot. Sur les franges des lames minces argentées et leur application a la mesure de petites épaisseurs d'air. *Ann. Chim. Phys*. 1897, 12:459 - 501.

[8] B. H. Lee, Y. H. Kim, K. S. Park, J. B. Eom, M. J. Kim, B.S. Rho, H.Y. Choi, Interferometric fiber optic sensors. *Sensors* 2012, 12, 2467 - 2486, DOI: 10.3390/s120302467.

[9] A. Othonos and K. Kalli. Fiber Bragg gratings: Fundamentals and applications in telecommunications and sensing. Artech House: New York, NY, USA, 1999.

[10] Y. J. Rao. Fiber Bragg grating sensors: principles and applications. In: K. T. V. Grattan, B. T. Meggitt. eds. Optical Fiber Sensor Technology 1998, 2: 355 - 389.

[11] G. Luyckx, E. Voet, N. Lammens, and J. Degrieck. Strain measurements of composite laminates with embedded fibre Bragg gratings: Criticism and opportunities for research. *Sensors* 2011, 11, 384 - 408, DOI: 10.3390/s110100384.

[12] X. Shu, Y. Liu, D. Zhao, B. Gwandu, F. Floreani, L. Zhang, and I. Bennion. Dependence of temperature and strain coefficients on fiber grating type and its application to simultaneous temperature and strain measurement. *Opt Lett*. 2002, 27, 9, 701, DOI: 10.1364/ol.27.000701.

[13] D. Kinet, P. Mégret, K. W. Goossen, L. Qiu, D. Heider, and C. Caucheteur. Fiber Bragg grating sensors toward structural health monitoring in composite materials: Challenges and solutions. *Sensors* 2014, 14, 7394 - 7419, DOI: 10.3390/s140407394.

[14] G. Hongwei, L. Hongmin, L. Bo, Z. Hao, L. Jianhua, C. Ye, Y. Shuzhong, Z. Weigang, K. Giuyun, and D. Xiaoyi. A novel Fiber Bragg grating sensor multiplexing technique. *Opt. Commun.* 2005, 251, 361 - 366, DOI: 10.1016/j.optcom.2005.03.027.

[15] B. Culshaw, and A. Kersey. Fiber-Optic Sensing: A Historical Perspective. *J. Lightw. Techol.* 2008, 26, 9, 1064 – 1078, DOI: 10.1109/JLT.0082.921915.

[16] T. Yoshino, K. Kurosawa, K. Itoh, and T. Ose. Fiber-optic Fabry–Perot interferometer and its sensor applications. *IEEE Transactions on Microwave Theory and Techniques* 1982, 30, 1612 - 1621, DOI: 10.1109/TMTT.1982.1131298.

[17] W. H. Tsai and C. J. Lin. A novel structure for the intrinsic Fabry-Perot fiber-optic temperature sensor. *J. Lightw. Techol*. 2001, 19, 682 - 686, DOI: 10.1109/50.923481.

[18] S. H. Kim, J. J. Lee, D.C. Lee, and I. B. Kwon. A study on the development of transmission-type extrinsic Fabry-Perot interferometric optical fiber sensor. *J. Lightw. Techol*. 1999, 17, 1869 - 1874, DOI: 10.1109/50.793768.

[19] T. G. Liu, J. D. Yin, J. F. Jiang, K. Liu, S. Wang, and S. L. Zou. Differential-pressure-based fiber-optic temperature sensor using Fabry-Perot interferometry. *Opt Lett.*, 2015, 40(6), 1049 - 1052, DOI: 10.1364/OL.40.001049.

[20] P. Chen and X. Shu. Refractive-index-modified-dot Fabry-Perot fiber probe fabricated by femtosecond laser for high-temperature sensing. *Opt. Express*, 2018, 26 (5), 5292 - 5299, DOI: 10.1364/OE.26.005292.

[21] S. Mekid, N. Saheb, S. M. A. Khan, and K. K Qureshi. Towards sensor array materials: can failure be delayed? *Sci. Technol. Adv. Mater*. 2015, 16, 034607, DOI: 10.1088/1468-6996/16/3/034607.

[22] M. R. Mokhtar, T. Sun, and K. T. V. Grattan. Bragg grating packages with non-uniform dimensions for strain and temperature sensing, *IEEE Sens. J.* 2012, 12, 139 - 144, DOI: 10.1109/JSEN.2011.2134845.

[23] O. Frazão, M. Melo, P. V. S. Marques, and J. L. Santos. Chirped Bragg grating fabricated in fused fibre taper for strain-temperature discrimination, *Meas. Sci. Technol.* 2005, 16, 984 - 988, DOI: 10.1088/0957-0233/16/4/010.

[24] C. Fernández-Valdivielso, I. R. Matías, and F. J. Arregui. Simultaneous measurement of strain and temperature using a fiber Bragg grating and a thermochromic material. *Sens. Act A* 2002, 101, 107 - 116, DOI: 10.1016/S0924-4247(02)00188-7.

[25] L. A. Ferreira, F. M. Araújo, J. L. Santos, and F. Farahi. Simultaneous measurement of strain and temperature using interferometrically interrogated fiber Bragg grating sensors. *Opt. Eng.* 2000, 39, 2226 - 2234, DOI: 10.1117/1.1305493.

[26] J. Jung, N. Park, and B. Lee. Simultaneous measurement of strain and temperature by use of a single fiber Bragg grating written in an erbium:ytterbium-doped fiber. *Appl. Opt.* 2000, 39, 1118 - 1120, DOI: 10.1364/ao.39.001118.

[27] B. Dong, J. Hao, C. Liaw, B. Lin, and S. C. Tjin. Simultaneously strain and temperature measurement using a compact photonic crystal fiber inter-modal interferometer and fiber Bragg grating. *Appl. Opt.* 2010, 49, 32:6232 – 6235, DOI: 10.1364/AO.49.006232.

[28] S. Novais, M. S. Ferreira, and J. L. Pinto. Lateral load sensing with an optical fiber inline microcavity, *IEEE Photon Technol Lett.* 2017, 29, 17:1502 – 1505, DOI: 10.1109/LPT.2017.2735021.

[29] A. K. Singh, S. Berggren, Y. Zhu, M. Han, and H. Huang. Simultaneous strain and temperature measurement using a single fiber Bragg grating embedded in a composite laminate. *Smart Mater. Struc*. 2017, 26, 115025, DOI: 10.1088/1361-665X/aa91ab.

[30] M. G. Zubel, K. Sugden, D. J. Webb, D. Saez-Rodriguez, K. Nielsen, and O. Bang. Embedding silica and polymer fibre Bragg gratings (FBG) in plastic 3D-printed sensing patches. Micro-structured and specialty optical fibres IV. 2016, DOI: 10.1117/12.2228753.

[31] B. Swain. Recovery and recycling of lithium: A review. *Separation and Purification Technology* 2017, 172, 388 - 403, DOI: 10.1016/j.seppur.2016.08.031.

[32] J. Staiger. Lithium Report 2017. Swiss resource Capital AG, 2017.

[33] G. E. Blomgren. The development and future of lithium ion batteries. *J. Electrochem. Soc.* 2017, 164, 1:A5019 - A5025, DOI: 10.1149/2.0251701jes.

[34] Y. Min and H. Junbo. Membranes in lithium ion batteries. *Membranes* 2012, 2, 367 – 383, DOI: 10.3390/membranes2030367.

[35] J. Kalhoff, G. G. Eshetu, D. Bresser, and S. Passerini. Safer electrolytes for lithium-ion batteries: state of the art and perspectives. *ChemSusChem* 2015, 8, 2154 - 2175, DOI: 10.1002/cssc.201500284.

[36] M.C. Smart, B. V. Ratnakumar, and S. Surampudi. Use of organic esters as co solvents in electrolytes for lithium-ion batteries with improved low temperature performance. *J. Electrochem. Soc.* 2002, 149, A1079 - A1082, DOI: 10.1149/1.1453407.

[37] M. Romare and L. Dahllöf. The life cycle energy: Consumption and greenhouse gas emissions from lithium-ion batteries. No. C 243. ISBN 978-91-88319-60-9, 2017.

[38] T.M. Bandhauer, S. Garimella, and T. F. Fuller. A critical review of thermal issues in lithium-ion batteries. *J. Electrochem. Soc.* 2011, 158, R1 -. R25, DOI: 10.1149/1.3515880

[39] X. Zhang, X. Kong, G. Li, and J. Li. Thermodynamic assessment of active cooling/heating methods for lithium-ion batteries of electric vehicles in extreme conditions. *Energy* 2014, 64, 1092 - 1101, DOI: 10.1016/j.energy.2013.10.088

[40] Battery University, 2017. Battery University. [Online] Available at: http://batteryuniversity.com [Accessed April 2018].

[41] Exploding lithium-ion battery lawsuits. [Online] Available at: https://www.chaffinluhana.com/exploding-lithium-ion-battery lawsuit. [Accessed July 2018].

[42] Bulging batteries frequently asked questions. [Online] Available at: https://smartofficesandsmarthomes.com/swelling-bulging-batteries-frequently-asked-questions. [Accessed July 2018].

[43] J. Yi, U. S. Kim, C. B. Shin, T. Han, and S. Park. Modeling the temperature dependence of the discharge behavior of a lithium-ion battery in low environmental temperature. *J. Power Sources* 2013, 244, 143 - 148, DOI: 10.1016/j.jpowsour.2013.02.085.

[44] R. Kizilel, R. Sabbah, J. R. Selman, and S. Al-Hallaj. An alternative cooling system to enhance the safety of Li-ion battery packs. *J. Power Sources* 2009, 194, 1105 - 1112, DOI: 10.1016/j.jpowsour.2009.06.074.

[45] H. P. Lin, D. Chua, M. Salomon, H-C. Shiao, M. Hendrickson, E. Plichta, and S. Slane. Low-temperature behavior of Li-ion cells. *Electrochem. Solid-State Lett*. 2001, 4, A71 - A73, DOI: 10.1149/1.1368736.

[46] J. Fan and S. Tan. Studies on charging lithium-ion cells at low temperatures. *J. Electrochem. Soc.* 2006, 153, A1081 - A1092, DOI: 10.1149/1.2190029.

[47] Y. Jia and C. Y. Wang. Heating strategies for Li-ion batteries operated from subzero temperatures. *Electrochemical Acta* 2013, 107, 664 - 674, DOI: 10.1016/j.electacta.2013.03.147.

[48] NissanUSA. How conditions affect range, 2012. Available at: http://www.nissanusa.com [Accessed May 2015].

[49] C. K. Huang, J. S. Sakamoto, J. Wolfenstine, and S. Surampudi. The limits of low-temperature performance of Li-ion cells. *J. Electrochem. Soc.* 2000, 147, 2893 - 2896, DOI: 10.1149/1.1393622.

[50] S. S. Zhang, K. Xu, and T. R. Jow. The low temperature performance of Li-ion batteries. *J. Power Sources* 2003, 115, 137 - 140, DOI: 10.1016/S0378-7753(02)00618-3.

[51] M. C. Smart, B. V. Ratnakumar, and S. Surampudi. Electrolytes for low-temperature lithium batteries based on ternary mixtures of aliphatic carbonates. *J. Electrochem. Soc.* 1999, 146, 486 - 492, DOI: 10.1149/1.1391633.

[52] S. S. Zhang, K. Xu, and T. R. Jow. Low temperature performance of graphite electrode in Li-ion cells. *Electrochemical Acta* 2002, 48, 241 - 246, DOI: 10.1016/S0013-4686(02)00620-5.

[53] H. L. Jae, M. L. Hyang, and A. Soonho. Battery dimensional changes during charge/discharge cycles – thin rectangular lithium ion and polymer cells. *J. Power Sources* 2003, 119 - 121, 833 - 837, DOI: 10.1016/S0378-7753(03)00281-7.

[54] M. S. Robert, J. Weaver, G. Yeduvaka, D. H. Doughty, and E. P. Roth. Simulation of abuse tolerance of lithium-ion battery packs. *J. Power Sources* 2007, 163, 1080 - 1086, DOI: 10.1016/j.jpowsour.2006.10.013.

[55] C. Veth, D. Dragicevic, and C. Merten. Thermal characterizations of a large-format lithium ion cell focused on high current discharges. *J. Power Sources* 2014, 267, 760 - 769, DOI: 10.1016/j.jpowsour.2014.05.139.

[56] S. Tippmann, D. Walper, L. Balboa, B. Spier, and W. G. Bessler. Low-temperature charging of lithium-ion cells part I: Electrochemical modeling and experimental investigation of degradation behavior. *J. Power Sources* 2014, 252, 305 - 316, DOI: 10.1016/j.jpowsour.2013.12.022.

[57] W. Xianming, S. Yoshitsugu, S. Go, N. Hitoshi, Y. Chisa, and K. Koichi. Understanding volume change in Lithium-ion cells during charging and discharging using in situ measurements. *J. Electrochem. Soc.* 2007, 154, A14 - A21, DOI: 10.1149/1.2386933.

[58] P. K. Leung, C. Moreno, I. Masters, S. Hazra, B. Conde, M. R. Mohamed, R. J. Dashwood, and R. Bhagat. Real-time displacement and strain mappings of lithium-ion batteries using three-dimensional digital image correlation. *J. Power Sources* 2014, 271, 82 - 86, DOI: 10.1016/j.jpowsour.2014.07.184.

[59] World Meteorological Organization [Online] Available at: http://www.wmo.int/pages/prog/wcp/ccl/faq/faq_doc_en.html. [Accessed August 2018].

[60] M. C. Peel, B. L. Finlayson, and T. A. McMahon. Updated world map of the Köppen-Geiger climate classification. *Hydrol. Earth Syst. Sci.* 2007, 11, 1633 - 1644, DOI: 10.5194/hess-11-1633-2007.

[61] W. Köppen. Das geographisca system der klimate, in: Handbuch der klimatologie. Ed. by: Köppen W. and Geiger G., 1. C. Gebr, Borntraeger, 1 - 44, 1936.

[62] M. Kottek, J. Grieser, C. Beck, B. Rudolf, and F. Rubel. World map of the Köppen-Geiger climate classification updated. *Meteorol. Z.* 2006, 15, 259 - 263, DOI: 10.1127/0941-2948/2006/0130.

Chapter II

Real time thermal monitoring of lithium batteries with fiber sensors and thermocouples: A comparative study

Published in *Measurement*, 2017, 111, 260-263
DOI: 10.1016/j.measurement.2017.07.049

Real time thermal monitoring of lithium batteries with fiber sensors and thermocouples: A comparative study

Micael Nascimento, Marta S. Ferreira, and João L. Pinto

Abstract

This work shows a comparative study between the thermocouples and fiber sensors response for the monitoring of temperature variations occurring in three different locations of a lithium battery. The battery is submitted to constant current charge and different discharge rates, under normal and abusive operating conditions. For this specific application, the results show that the fiber Bragg grating sensors have better resolution and a rise time 28.2 % lower than the K-type thermocouples, making them a better choice for the real time monitoring of the battery surface temperature as well as a useful tool for failure detection and an optimized management in batteries.

Keywords: Fiber sensors; Thermocouples; Temperature monitoring; Lithium batteries; Abusive conditions.

1. Introduction

Nowadays, due to the strong decrease of the worldwide petroleum resources and the present environment pollution, significant research has been carried out on the development of lithium-ion batteries (LIBs) as alternative energy power supplies [1, 2]. The traditional LIBs are extensively used in portable electronic equipment, such as notebook computers, mobile phones and electric vehicles due to its high energy density, high voltage and low self-discharge rate [3, 4].

The primary challenge in designing a scaled-up LIBs system is to guarantee safety under normal and abuse operating conditions. Thermal management of batteries is critical in achieving better lifetime performance and safety of the batteries. Besides, the heat generated in a battery must be controlled in order to improve lifecycle reliability and prevent failure.

The LIB operation out of the adequate range of temperatures can cause their rapid degradation and reduction of the available discharge energy [5]. When carried out under

abnormal conditions, they are largely exothermic, causing fast temperature increase [2]. The effective control and management of battery charge and discharge by battery management systems (BMS) is essential for good performance. In order to develop a sufficient thermal management strategy, it is essential to monitor the thermal gradient in the battery during all operating states for an accurate online diagnostic analysis. Current BMS rely on monitoring conventional external parameters such as voltage, current and external temperature.

Most of the previous works were focused on monitoring temperature using thermocouples (TC) attached to the surface of batteries, in strategic locations. The TC have the advantages of small dimensions, self-powered and ease of handling [7, 8]. Recent works have proposed the use of optical fiber sensors as an alternative method, due to their intrinsic characteristics, such as small dimensions, capability of multiplexing, chemical inertness, and the possibility of optimized integration inside the batteries. They also have the ability to monitor simultaneously multi-parameters such as temperature, strain, and pressure [4, 9]. In general, the performance of both types of sensors has been increasingly questioned in terms of response rates and accuracy, under normal and abusive operating conditions.

In this study, a comparative outcome of the real-time monitoring of surface temperature variations using fiber Bragg grating sensors (FBGs) and TC, in three different positions of a rechargeable LIB under constant current charge and different discharge rates is presented.

2. Experimental setup

A schematic diagram of the experimental setup for real time temperature monitoring of the LIB is shown in Fig. II.1. A commercial rechargeable Li-ion Polymer Battery (Iphone 5G Battery, Singapore) with maximum voltage of 4.3 V, nominal capacity of 1440 mAh and dimensions of 130 mm (length) × 90 mm (width) × 20 mm (height), was used.

The temperature variations (ΔT) were monitored with three K-type commercial TCs (RS Pro, Israel) and three FBGs, all glued to the surface of the battery in three different positions (top, middle and bottom). The TCs had a conductor dimension of 1.0/0.2 mm and a temperature operation range from –75.0 °C up to 260.0 °C. The three FBGs (length of 3.0 mm), spaced by 40.0 mm, were written by the phase mask method in a commercial photosensitive single mode fiber (PS1250/1500, FiberCore). Typically, these sensors can operate from 0 °C up to ~350 °C without damaging the sensor reflection signal.

The TCs signals were acquired using a NI compactDAQ (NI cDAQ-9174, National Instruments) with a temperature module (NI 9211, National Instruments). The Bragg wavelength was monitored using an interrogation system (sm125-500, Micron Optics Inc., Atlanta, USA) with a sample rate of 2 Hz and a wavelength accuracy of 1 pm.

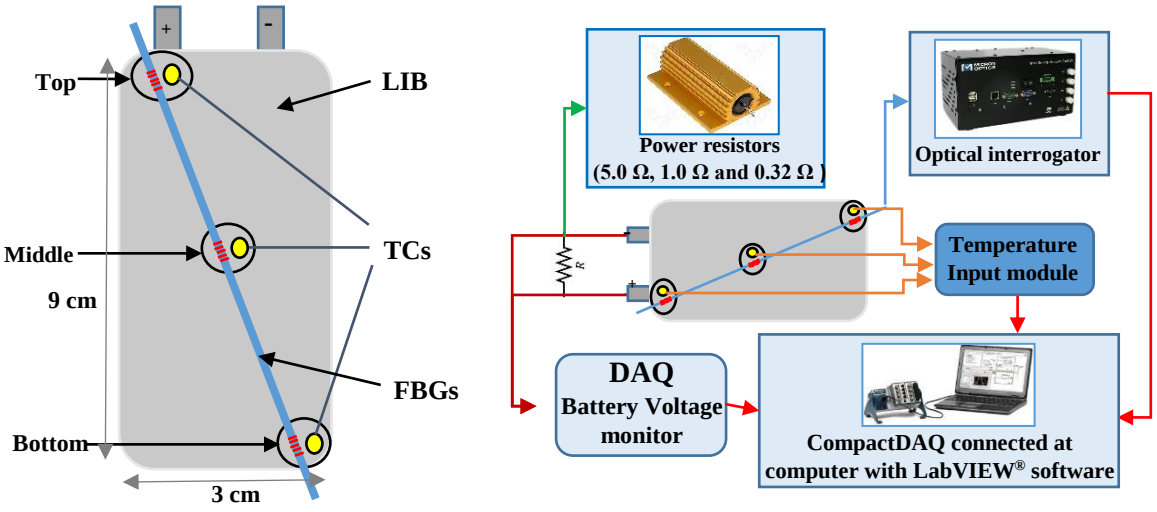

Figure II.1. (left) Schematic of rechargeable LIB test setup with the location of TCs and FBGs and (right) schematic diagram.

The LIB voltage was monitored using a 12-bit resolution data acquisition system (DAQ) (USB6008, National Instruments). The acquisition modules were controlled using a computer with a LabVIEW® customized application, allowing the real-time monitoring of the acquired data. During all experiments, the battery was kept away from external heat sources, and the environmental temperature, monitored by a reference TC, was of ~20.0 °C. This value was considered for the ΔT calculations.

2.1. Sensors thermal calibration

The sensors were calibrated on a thermal chamber (Model 340, Challenge Angelantoni Industrie) in a temperature range from 10.0 °C up to 50.0 °C, with 10.0 °C steps. At room temperature, the Bragg wavelengths of these sensors were 1536.27 nm (FBG Top), 1546.21 nm (FBG Middle) and 1561.65 nm (FBG Bottom). Sensitivities of 9.08 pm/°C,

9.17 pm/°C, and 9.24 pm/°C were respectively obtained for the FBGs located at the top, middle and bottom positions.

Through the equation $\Delta\lambda = k_T \times \Delta T$, where $\Delta\lambda$ and k_T are the wavelength shift and temperature sensitivity, respectively, it is possible to determine the ΔT detected by the sensors. Uncertainties of 0.17 °C and 0.12 °C were obtained for the TCs and the FBGs, respectively. This parameter was determined by considering the calculation of the standard deviation between the maximum and minimum fluctuations of the sensors signals, acquired over 1 h on a thermal chamber with stabilized temperature.

2.2. Battery test procedure

To perform the cycling tests on the battery different discharge rates (0.53 C, 2.67 C and 8.25 C, where 1 C is the rate of the ideal capacity charge/discharge in 1 h) were used, in order to monitor the battery performance and behavior under normal and abnormal operating conditions. Three different power resistors (10 W) were employed, with an equivalent resistance of 5.00 Ω, 1.00 Ω, and 0.32 Ω.

The charge was performed at a C-rate of 0.70 C, using a commercial battery charger with output voltage of 5.0 V (ETA0U83EWE, Samsung, Vietnam). The battery test procedure, shown in Table II.1, was selected in order to promote abusive operating conditions on the battery.

Table II.1 Battery test procedure.

Steps	**Time (min)**	**C-rate**	**Limit criteria**
Charge (C)		0.70 C	≈ 4.0 V
Rest (R)	10		
Discharge (D)		0.53 C	≈ 0.5 V
Rest (R)	15		
	Cycle Repetition		
Charge (C)		0.70 C	≈ 4.0 V
Rest (R)	10		
Discharge (D)		2.67 C	≈ 0.5 V
Rest (R)	15		
	Cycle Repetition		
Charge (C)		0.70 C	≈ 4.0 V
Rest (R)	10		
Discharge (D)		8.25 C	≈ 0.5 V
Rest (R)	15		
	Cycle Repetition		

In all the experiments, the battery was discharged until a voltage of 0.5 V was reached. Between the charge/discharge steps, a resting time was selected in order to stabilize the battery temperature. Each discharge rate was repeated several times and the results were consistent throughout the experiments.

3. Results and discussion

The sensors output signals during two of the cycling tests for each C-rate, and the corresponding battery voltage are shown in Fig. II.2 (left). During the charge process, an increase of (1.00 ± 0.12) °C was registered until the battery charged was ~98.8%. Above this value and until the maximum voltage achievement (4.0 V), the temperature decreased once again to room temperature. This behaviour was consistent throughout the experiments.

Regarding the discharge, it was observed that a significant rise of ΔT occurs when the discharge rate increases. However, the temperature variations for each cycle repetition were nearly the same. For the lowest C-rate, the discharge occurred in ~1.6 h. As the voltage decreases until it reaches 3.2 V, the temperature increase is lower than (1.00 ± 0.12) °C. After this value, the battery is working in abnormal conditions and the voltage drops significantly. In this case the temperature shift detected by the FBGs is ~2.50 °C.

The same behaviour was observed for 2.67 C-rate: below the cut-off voltage, there was a significant increase of temperature. This effect was not observed for the highest C-rate because at such extreme conditions the voltage drop is nearly instantaneous. In fact, for 2.67 C it takes 6.4 min for the voltage to drop to 3.2 V, whereas for the highest C-rate it took only few seconds until it reached abnormal condition voltages. The changes in temperature showed a direct correlation with the applied current gradient, with the highest peaks being detected always at the end of discharge. This is coherent with the fact that, over discharge, Li ions migrate inside the battery to establish a concentration gradient, which generates heat as a function of the applied current.

The zoom in of the highest discharge rate is presented in Fig. II.2 (right). From this figure, it is evident that the FBGs detect higher temperature variations in all locations. During the higher discharge rate, the response rate of the sensors located in the top was determined by considering the time required by the sensors to reach 63% (t63) of the temperature, after a sudden temperature increase.

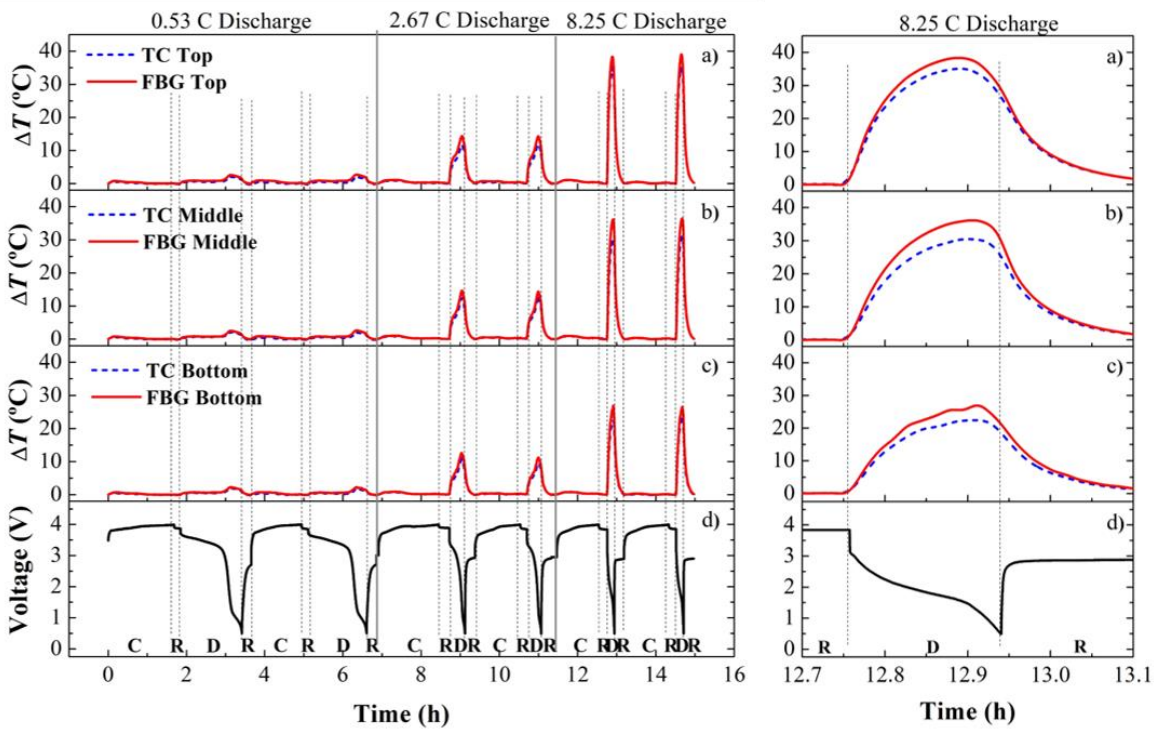

Figure II.2. (left) Surface temperature variations during the cycling tests. Three different positions are considered: a) top, b) middle, c) bottom, and d) correspondent LIB voltage. Steps: C-charge, R-rest, D-discharge. (right) Zoom in of the sensors response for the last cycling test.

Thus, the response rate was estimated to be 4.88 °C/min and 4.10 °C/min, for the FBG and TC, respectively. This indicates that the FBGs presented a response rate ~1.2 times higher than the TCs. Besides, considering the time interval for the temperature range between (10% - 90%) ΔT, a lower rise time of 28.2% was obtained for the FBGs in comparison to the TCs. These values were approximately constant in all locations and for C-rates considered. This result is an important evidence of the fast response of the FBGs compared with the TCs.

The maximum temperature variations measured by the sensors in the different locations are shown in Fig. II.3. For the lower C-rate, the maximum temperature reached is nearly constant (~2.50 °C) throughout the LIB surface. For 2.67 C, the higher ΔT values were recorded by the sensors located on the middle position, followed by the ones on the top, and finally on the bottom.

However, for 8.25 C, the higher temperature variations were detected by the top sensors

(39.98 ± 0.12) °C and (35.07 ± 0.17) °C for FBG and TC, followed by the middle (36.42 ± 0.12) °C and (30.63 ± 0.17) °C, for FBG and TC, and finally the bottom position (27.19 ± 0.12) °C and (23.05 ± 0.17) °C, for FBG and TC, respectively. This indicates that the temperature gradient profile within the surface of the battery changes according to the discharge rate.

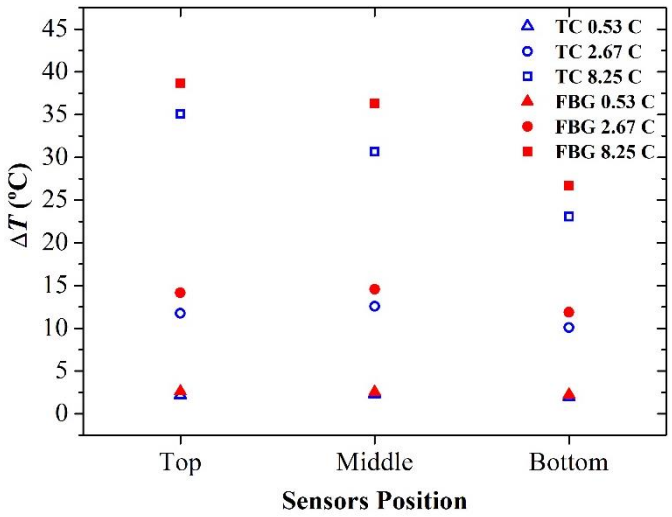

Figure II.3. Maximum Δ*T* values registered by both types of sensors for each sensors position.

The difference between the discharge peak Δ*T* values detected for both types of sensors, in each battery location, is presented in Fig. II.4. It stands out that the higher the C-rate, the larger the discrepancy between the sensors response (which can be as high as ~5.77 °C for the middle position). Under normal operating conditions (lower C-rates), the two types of sensors responses are closer to each other.

As the discharge rate increases and the discharging time decreases, this difference becomes significant and the use of fiber-based sensors can give more accurate responses than the standard electric ones. Under such conditions, the TCs do not have the ability to respond rapidly to the heat generation that occurs in the battery and the correspondent fast increase on the battery surface temperature.

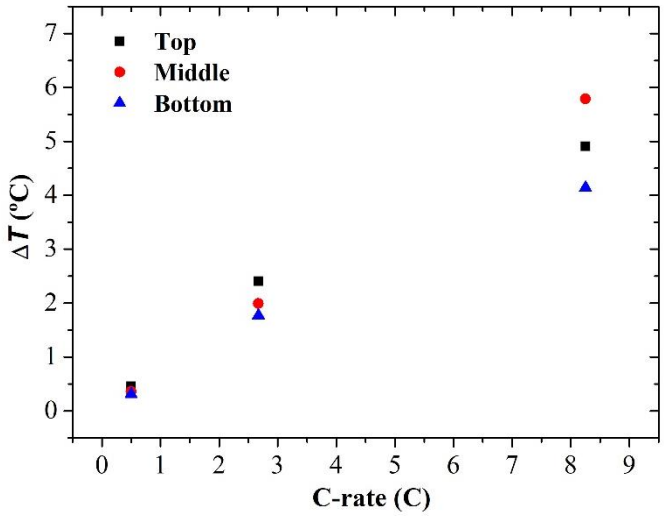

Figure II.4. Difference between the maximum temperature variations detected by the FBGs and TCs for different locations and discharge rates.

This outcome needs to be considered for battery management system and battery modelling purposes, since battery damages caused by overheating are an important reason for capacity fading in Li-ion batteries and thermal runaways are the major source of safety concerns.

4. Conclusions

FBG and TC sensors were successfully coupled in LIB in order to monitor temperature changes during testing at different discharge rates (0.53 C, 2.67 C, and 8.25 C) and normal constant charge. Three different locations were monitored on the battery surface. For the higher discharge rate of 8.25 C, temperature variations of (39.98 ± 0.12) °C were registered by the FBGs compared with the (35.07 ± 0.17) °C registered by the TCs, on the top position.

On the middle and bottom positions, the variations were of (36.42 ± 0.12) °C and (27.19 ± 0.12) °C for the FBGs and (30.63 ± 0.17) °C and (23.05 ± 0.17) °C for the TCs, respectively. The results obtained show that, for this particular application, the FBGs had a rise time 28.2% lower than the TCs, making them a better choice for the real time monitoring of the batteries surface temperature under normal and abuse operating conditions and a useful tool for failure detection in batteries.

LIBs used commercially, especially for mobile device applications are rarely under constant voltage condition, but often subjected to continuous cycling. In fact, strong heating of the batteries inside smartphones is an everyday experience. This is not only unpleasant, but also deleterious to the battery life as high temperatures favor electrolyte decomposition. A better understanding of the temperature variations in LIB under heavy-duty cycling, accessible with the sensors presented in this work, is key for the improvement of battery components and management systems.

Acknowledgments: This work is funded by European project "Stable Interfaces for Rechargeable Batteries "(SIRBATT) (FP7-ENERGY-2013, grant agreement No. 608502) and by FEDER funds through the COMPETE 2020 Programme and National Funds through FCT - Portuguese Foundation for Science and Technology under the project UID/CTM/50025/2013. Micael Nascimento and Marta S. Ferreira are also grateful for the research fellowships no. BI/UI6642/2016 and BPD/UI96/7331/2016, respectively.

References

[1] J. Chen and F. Cheng. Combination of lightweight elements and nanostructured materials for batteries. *Accounts Chem. Res*. 42 (2009) 713-723.

[2] R. Kizilel, R. Sabbah, J. R. Selman, and S. Al-Hallaj. An alternative cooling system to enhance the safety of Li-ion battery packs. *J. Power Sources* 194 (2009) 1105-1112.

[3] C-Y. Lee, S-J. Lee, Y-M. Hung, C-T. Hsieh, Y-M. Chang, Y-T. Huang, and J-Y. Lin. Integrated microsensor for real time microscopic monitoring of local temperature, voltage and current inside lithium ion battery. *Sensor Actuat. A-Phys*. 253 (2017) 59-68.

[4] G. Yang, C. Leitão, Y. Lib, J. Pinto, and X. Jiang. Real-time temperature measurement with fiber Bragg sensors in lithium batteries for safety usage. *Measurement* 46 (2013) 3166-3172.

[5] M. Yildiz, H. Karakoc, and I. Dincer. Modelling and validation of temperature changes in a pouch lithium ion battery at various discharge rates. *Int. Commun. Heat Mass* 75 (2016) 311-314.

[6] L. W. Sommer, P. Kiesel, A. Ganguli, A. Lochbaum, B. Saha, J. Schwartz, C-J. Bae, and M. Alamgir. Fast and slow ion diffusion processes in lithium ion pouch cells during cycling observed with fiber optic strain sensors. *J. Power Sources* 296 (2015) 46-52.

[7] P. Wang, X. Zhang, L. Yang, X. Zhang, M. Yang, H. Chen, and D. Fang. Real-time monitoring of internal temperature evolution of li ion coin cell battery during the charge and discharge process. *Extreme Mech. Lett.* 9 (2016) 459-466.

[8] L. Zhe, J. Zhang, B. Wu, J.Huang, Z. Nie, Y. Sun, F. An, and N. Wu. Examining temporal and spatial variations of internal temperature in large-format laminated battery with embedded thermocouples. *J. Power Sources* 241 (2013) 536-553.

[9] M. Nascimento, S. Novais, C. Leitão, M. F. Domingues, N. Alberto, P. Antunes, and J. Pinto. Lithium batteries temperature and strain fiber monitoring. *Proc. SPIE*, OFS24, 9634 (2015) 9634V-1 - 9634V-4.

Chapter III

Lithium batteries temperature and strain fiber monitoring

Published in *Proc. SPIE*, 2015, 9634, 96347V1 – 96247V4

DOI: 10.1117/12.2195218

Lithium batteries temperature and strain fiber monitoring

Micael Nascimento, Susana Novais, Cátia Leitão, M. Fátima Domingues, Nélia Alberto, Paulo Antunes, João L. Pinto

Abstract

Fiber Bragg grating sensors were attached to the surface of a rechargeable lithium battery to monitor its thermal and strain fluctuations through charge and different discharge rates. During the discharge process above 1 C, it was observed, a temperature and strain fluctuations of a 4.12 ± 0.67 °C and 24.64 ± 6.02 με, respectively. In the regular charge process, a temperature and strain variation of 1.03 ± 0.67 °C and 15.86 ± 6.02 με, were detected.

Keywords: Lithium battery, Bragg sensor, temperature, strain, safety.

1. Introduction

Nowadays, due to the present environment pollution and the strong decrease of the worldwide petroleum sources, significant research has been carried out on the development of lithium batteries as new energy power supplies [1]. The primary challenge in designing a scaled-up lithium battery system is to guarantee safety in normal and under abuse operating conditions. Thermal and pressure stability of lithium batteries are the most important parameters for safety [2]. They are largely exothermic, causing fast temperature increase, when carried out under abnormal conditions [1, 3].

In abuse conditions, such as under high current density charge/discharge cycles and in short circuit, the rapidly increase of temperature and pressure could cause the appearance of hot spots, which may lead to an increasing degradation rate or even to its explosion and/or combustion [4]. Quantitative measurements of the heat generation rate inside a single battery during normal and abuse conditions are required to design and develop a suitable thermal management system for scaled-up batteries [5].

To overcome the limitations of electronic sensors in challenging environments, optical fiber sensors have been widely used in physical, chemical, and even biological measurements, owing to their fast response, high resolution, good stability and repeatability, electrical isolation, chemical inertness and immunity to electromagnetic interference.

Moreover, they have the advantages of small dimensions, flexibility and multiplexing ability [6].

Typically, the monitoring of the surface temperature of lithium batteries is performed using thermocouples, electro-mechanical sensors, and pyrometers [5]. Recent works showed that optical fiber sensors are an effective method to perform both static and dynamic temperature measurements in batteries [2].

In the present study, the outcome of the real-time monitoring of external temperature and strain variations using fiber Bragg grating (FBG) sensors, for a rechargeable cylindrical lithium battery under charge and different discharge rates is presented.

2. Experimental setup

For these exploratory tests, a commercial rechargeable lithium battery (LITUR18650WSAN, Sanyo) with maximum voltage of 3.7 V and nominal capacity of 1500 mAh was used. The cathode is a lithium cobalt oxide and the anode is composed by graphite. Lithium ions are extracted from the anode and flow into the cathode during discharge.

The electrolyte is a solution consisting of organic solvent and inorganic salt, which provides the medium for lithium ions transport [7]. A small part of the polymeric protective layer was removed and the FBG sensors were placed in direct contact with the aluminium surface, as schematized in Figure III.1.

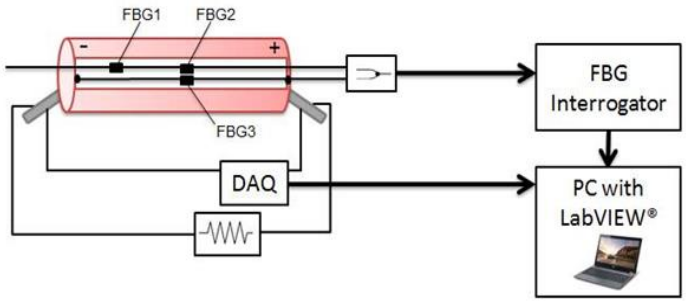

Figure III.1. Experimental setup diagram of the temperature and strain monitoring system during charge/discharge of the battery.

The FBGs used in the monitoring system were written in commercial photosensitive single mode fiber (FiberCore PS1250/1500), previously calibrated on a thermal chamber (Model 340, Challenge Angelantoni Industrie). To monitor the temperature variations on the battery, two FBG sensors were inscribed in the same fiber, spaced out 2 cm from each other and attached to the battery surface. At room temperature, the Bragg wavelengths of these sensors were 1550.35 nm (FBG1) and 1543.09 nm (FBG2). Along the fiber, a thermal paste was used to increase thermal conductivity between the battery and the FBG sensors.

The detection of the strain fluctuations was accomplished by using a third FBG sensor (FBG3), placed along the battery's longitudinal axis, monitoring strain changes on the battery full length. This FBG was calibrated for strain measurement using a micrometric translation stage. The fiber was pre-tensioned and fixed to the battery on its extremities, resulting in a final Bragg wavelength of 1565.80 nm.

The tests were repeated twice for each C-rate discharge under study (0.25 C and 1.33 C, where 1 C is the rate of the ideal capacity charge/discharge in 1 h) and the charge process was performed 5 times. The FBG1 and FBG2 only measured temperature variations while FBG3 was subjected to the strain and temperature variations that occurred in the battery. Temperature measurements made by FBG2 sensor were used to compensate thermal effects on FBG3, allowing to measure the longitudinal strain variation along the battery length.

The voltage values along the process were monitored using a 12-bit resolution data acquisition system (DAQ) (USB6008, National Instruments) and the Bragg wavelength was monitored using a spectrometer (I-MON 512E model, Ibsen, sample rate of 95.2 Hz and wavelength resolution of 5 pm). The acquisition modules were controlled in the computer by a *LabVIEW*® customized application, allowing the real-time monitoring of the acquired data.

3. Results and discussion

The thermal characterization of the FBG sensors was made in a range of temperatures between 5 °C and 50 °C, in steps of 5 °C. Sensitivities of 7.51 ± 0.15 pm/°C for FBG1 ($r^2 > 0.998$) and 7.43 ± 0.15 pm/°C for FBG2 ($r^2 > 0.997$) were obtained. FBG3 strain characterization yielded to a strain sensitivity of 0.83 ± 0.01 pm/με ($r^2 > 0.992$).

Figure III.2 represents the temperature and strain fluctuations during the charge process of the battery. For the two regions in analysis, a continuous increase of the temperature was obtained during all charging process (100 min), measuring a temperature variation of 1.08 ± 0.66 °C (FBG1) and 1.03 ± 0.67 °C (FGB2), respectively (Fig. III.2 a)). The similarity between these values suggest a uniform distribution of the temperature for the charge process. Regarding the strain monitoring, also a uniform increase was registered, achieving maximum variation of 15.86 ± 6.02 με, (Fig. III.2 b)). This behaviour corresponds to a longitudinal variation of 0.05 %.

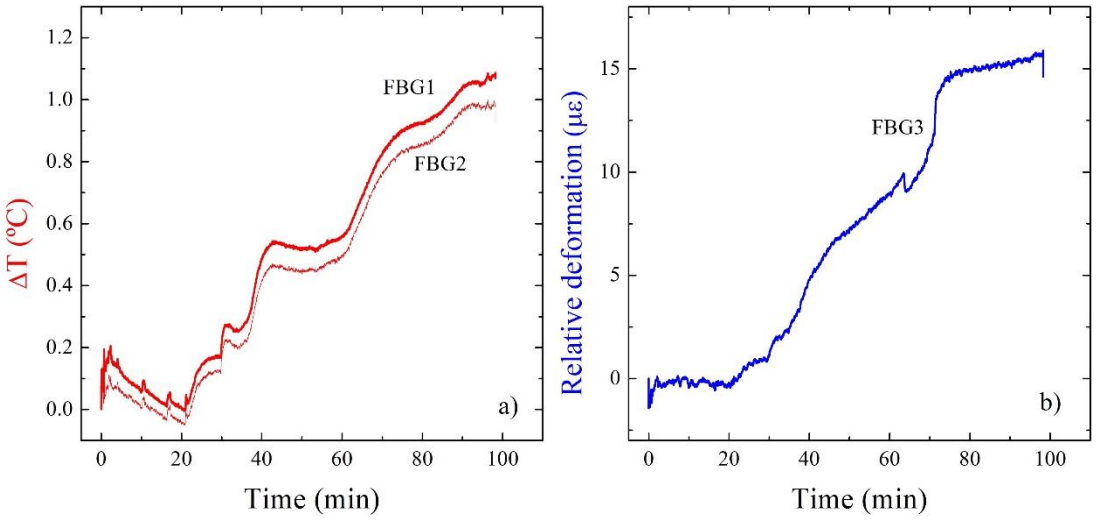

Figure III.2. Temperature a) and strain b) variation during the charge process, under normal conditions.

Figure III.3 a) presents the temperature fluctuations as function of time for the two considered regions of the battery during the discharge process at low C-rate (0.25 C), throughout which it was observed a similar temperature behaviour. Temperature variations of 1.37 ± 0.66 °C and 1.47 ± 0.67 °C were observed, in the FBG1 and FBG2, respectively.

Figure III.3 b) summarizes the results obtained for high C-rate (1.33 C). Under this condition, it was measured a temperature variation of 4.53 ± 0.66 °C in the FBG1, whereas in the FBG2, a temperature variation of 4.12 ± 0.67 °C was registered. Although the increase of the temperature was accentuated, a uniformity of the thermal distribution during this process was still evident, as both sensors registered similar variations. Also, it is evident, in

both figures that the maximum values obtained for the temperature variation are in accordance with the sudden decrease of the current.

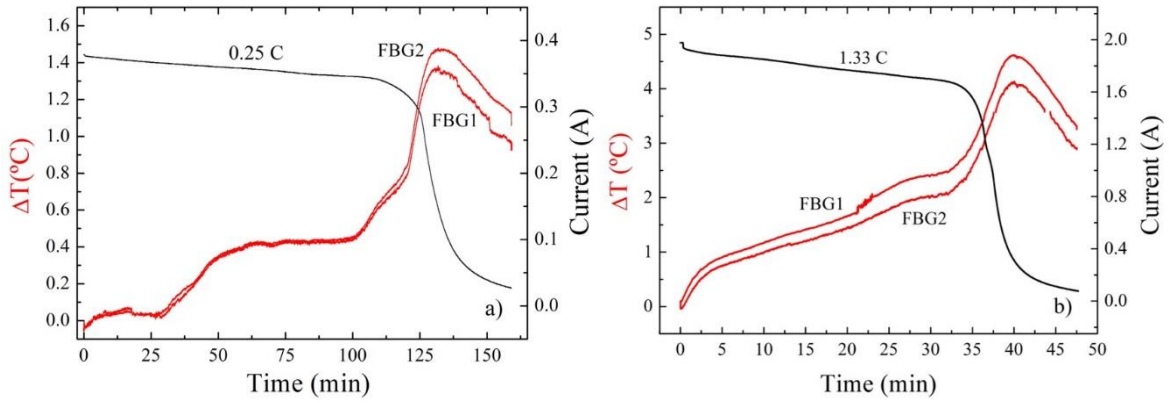

Figure III.3. Temperature and current fluctuations during the discharge process in two different regions of the battery for: a) low (0.25 C) and b) high (1.33 C) rates.

Regarding the strain behaviour, in Fig. III.4 a) it can be seen a variation of 9.72 ± 6.02 με, at the 125 min, which occurs simultaneously with the abrupt decrease of the current, for low discharge rate conditions. This strain variation can be translated as a longitudinal variation of 0.05 % of the battery, considering that at the thermal linear expansion of the battery surface material (α_{al} = 22.10 x 10^{-6} °C^{-1}) registered for this low current analysis can be neglected.

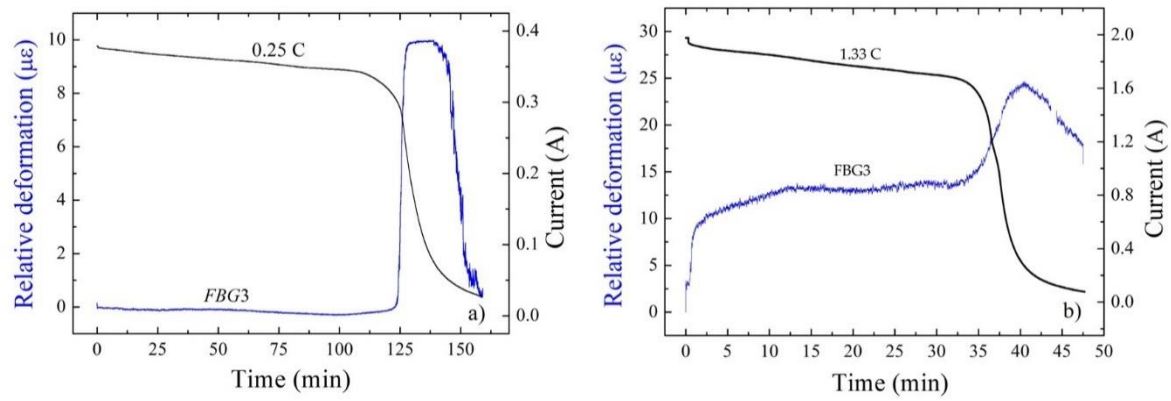

Figure III.4. Strain and current variations during discharge process of the battery for: a) low (0.25 C) and b) high (1.33 C) rates.

In Figure III.4 b), it is presented the strain variation as function of the time of discharge, for high C-rates (1.33 C). In this situation, it was measured a relative deformation of 24.64 ± 6.02 με, at the 40 min. Also, as in the temperature analysis, the maximum values of the strain variation occur when the abrupt decrease in the current is registered.

4. Conclusions

In this work, FBG sensors were attached with success to the surface of a rechargeable lithium battery to monitor its thermal and strain variations through charge and different discharge rates. Under abnormal conditions (1.33 C), during the discharge process, it was measured higher temperature fluctuation and consequent strain variations, induced by the increase of the battery internal pressure.

As future work it is intended to test the battery with a multiplexed sensors network, to obtain a broader knowledge of the temperature and strain variations profiles. Other aim is to integrate the FBGs inside the battery to monitor internal temperature and pressure under normal and abusive conditions. Thereby, this method allows to monitor temperature and pressure variations in lithium batteries and from those values to identify the battery health condition and remaining life time.

Acknowledgments: Micael Nascimento, Susana Novais and M. Fátima Domingues acknowledges the financial support from the Project 608502-SIRBATT though the research fellowship BI/UI96/6642/2014, BI/UI96/6643/2014 and BI/UI96/7040/2015, respectively. Cátia Leitão acknowledges the financial support from Fundação para a Ciência e a Tecnologia (FCT) through the Doctoral fellowship SFRH/BD/84076/2012, Nélia Alberto and Paulo Antunes the Postdoctoral fellowships SFRH/BPD/78141/2011, SFRH/BPD/76735/2011, respectively.

References

[1] Kizilel, R., Lateef. A., Sabbah, R., Farid, M., Selman, J. and Al-Hallaj, S. Passive control of temperature excursion and uniformity in high-energy Li-ion battery packs at high current and ambient temperature. Journal of Power Sources 183, 370-375 (2008).

[2] Yang, G., Leitão, C., Li, Y., Pinto, J. L. and Jiang, X. Real-time temperature measurement with fiber Bragg sensors in lithium batteries for safety usage. Measurement 46, 3166-3172 (2013).

[3] Kizilel, R., Sabbah, R., Selman, J. R. and Al-Hallaj, S. An alternative cooling system to enhance the safety of Li-ion battery packs. Journal of Power Sources 194, 1105-1112 (2009).

[4] Spotnitza, R. and Franklin, J. Abuse behavior of high-power, lithium-ion cells. Journal of Power Sources 113, 81–100 (2003).

[5] Kim, U. S., Shin, C. B., Kim, C. S. Effect of electrode configuration on the thermal behavior of a lithium-polymer battery. Journal Power Sources 180, 909–916 (2008).

[6] Antunes, P., Lima, H., Monteiro, J., Andre, P. S. Elastic constant measurement for standard and photosensitive single mode optical fiber. Microwave and Optical Technology Letters 50, 2467-2469 (2008).

[7] Fu, Y., Lu, S., Li, K., Liu, C., Cheng, X., Zhang, H. An experimental study on burning behaviors of 18650 lithium ion batteries using a cone calorimeter. Journal of Power Sources 273, 216-222 (2015).

Chapter IV

Simultaneous sensing of temperature and bi-directional strain in a prismatic Li-ion battery

Published in *Batteries,* 2018, 4(2), 23

DOI: 10.3390/batteries4020023

Additional information is available at the end of this Chapter.

Simultaneous sensing of temperature and bi-directional strain in a prismatic Li-ion battery

Micael Nascimento, Marta S. Ferreira, and João L. Pinto

Abstract

Thermal and pressure stability of Li-ion batteries (LIB) are the most important parameters for safety. In abuse operating conditions, the rapid increase of temperature and pressure can cause the appearance of hot spots, which may lead to an increasing degradation rate or even to the battery's explosion and/or combustion. A sensing network of fiber Bragg gratings is attached to the surface of a prismatic LIB to monitor its temperature and bi-directional strain variations through normal charge (0.70 C) and two different discharge rates (1.32 C and 5.77 C) in the x- and y-directions. More significant variations are registered when the LIB operates in abnormal conditions. A maximum temperature variation of 27.52 ± 0.13 °C is detected by the sensors located close to the positive electrode side. Regarding strain and consequent length variations, maximum values of 593.58 ± 0.83 με and 51.05 ± 0.37 μm are respectively obtained by the sensors placed on the y-direction. The sensing network presented can be a solution for the real-time monitoring, multipoint and *operando* temperature and bi-directional strain variations in the LIBs, promoting their safety.

Keywords: Li-ion batteries; fiber Bragg grating sensor; strain; temperature; safety.

1. Introduction

Lithium-ion batteries (LIB) are extensively used as power sources for a wide range of electronic devices such as smartphones and laptops, ensuring optimized conditions in the perspective of power, energy, long cycle-life, and slow self-discharge [1, 2]. Prismatic LIBs, characteristically used on smartphones, are more disposed to thermal and mechanical abuses from external actions.

The induced strain can be a question that affects the LIB stability and safety, making it the principal cause of material cracking and other forms of performance degradation [3]. Analogous to other electrochemical energy storage systems, the chemical compositions of the active materials change under the charge/discharge processes, which induces strains in

electrode particles and causes changes in LIB volume. The aim of thickness reduction of smartphones can be a problem for the users, because these new designs of the smartphone do not integrate a dually protective device which relieves at a set pressure, thus avoiding the overpressure of the LIB. Additionally, LIB companies pursue higher energy density and thinner devices at the cost of safety, which moves against the inherently safer design of a commercial LIB [4].

In addition to strain, thermal runaway is also an essential issue, with impact in the global LIB performance, which is reproduced by the fast increase of temperature. The internal structures of prismatic LIBs are made-up of multiple layers, forming a 'jelly roll' structure, where each layer consists of the anode, cathode, electrolyte, and polymer film separators.

Under abnormal conditions, such as temperature exceeding the separators melting point, mechanical deformation, or breakdown of the layered materials, an internal short circuit can happen. The hot spot generated by internal short circuit can ignite thermal runaway, leading to fire or explosion of the LIB [5, 6].

The ability to quantify and evaluate the mechanism of strain and thermal runaway generated during the electrochemical processes that the batteries can operate will be beneficial information regarding their behavior as well as an active tool to promote their safety. The temperature and strain sensing of LIB is typically performed using thermocouples [7, 8], pyrometers [9], electro-mechanical sensors [10], and 3D digital image correlation [6].

Due to their ease in multiplexing, fast response, immunity to electromagnetic interference advantages when compared to electronic sensors [11], recent works showed that fiber Bragg gratings (FBG) are an effective method to perform temperature and strain measurements in LIBs [12–16].

In this work, through a sensing network of FBGs, quantitative temperature, bi-directional strain shifts, and correspondent longitudinal and transversal variations are provided, as a function of the respective voltage signal of a prismatic LIB, during different cycling protocols.

2. Materials and methods

2.1 FBG Sensors: Mechanism of operation

Typically, a FBG sensor consists of a short segment of a single-mode optical fiber (with a length of a few millimeters) with a photoinduced periodically modulated index of refraction in the core of the fiber. The FBG resonant wavelength is related to the effective refractive index of the core mode (n_{eff}) and to the grating period (Λ). When the grating is illuminated with a broadband optical source, the reflected power spectrum presents a sharp peak (with a full width at half maximum of a few nanometers), which is caused by interference of light with the planes of the grating and can be described through Equation (1) [11].

$$\lambda_B = 2n_{eff}\Lambda \tag{1}$$

where λ_B is the so-called Bragg wavelength. When the fiber is exposed to external variations of a given measurand (such as strain, temperature, stress or pressure, among others), both n_{eff} and Λ can be altered, causing a shift in the Bragg wavelength.

The FBG sensitivity towards a given parameter is obtained simply by subjecting the sensor to pre-determined and controlled variations of such parameter and measuring the Bragg wavelength for each step. In the case of a linear response, the sensitivity (k) is given by the slope of the linear fit obtained from the experimental data. The effects of temperature are accounted for in the Bragg wavelength shift by differentiating Equation (1),

$$\Delta\lambda = 2\lambda_B\left(\frac{1}{n_{eff}}\frac{\partial n_{eff}}{\partial T} + \frac{1}{\Lambda}\frac{\partial \Lambda}{\partial T}\right)\Delta T = \lambda_B(\alpha + \xi)\Delta T = k_T\Delta T, \tag{2}$$

where α and ξ are the thermal expansion and thermo-optic coefficient of the optical fiber material, respectively. On the other hand, if the fiber is subjected to strain variations, its response can be determined by differentiating Equation (1),

$$\Delta\lambda = \lambda_B\left(\frac{1}{n_{eff}}\frac{\partial n_{eff}}{\partial \varepsilon} + \frac{1}{\Lambda}\frac{\partial \Lambda}{\partial \varepsilon}\right)\Delta\varepsilon = \lambda_B(1 - p_e)\Delta\varepsilon = k_\varepsilon\Delta\varepsilon, \tag{3}$$

where p_e is the photoelastic constant of the fiber (~0.22) and $\Delta\varepsilon$ is the applied strain. The strain variations can be determined using the equation $\Delta\varepsilon = \Delta L/L$ where ΔL is the length variation and L the fiber length over which strain is applied.

2.2 Strain and temperature discrimination: Reference FBG method

The temperature and bi-directional strain discrimination were performed using the reference FBG method. On a single measurement of the Bragg wavelength-shift, it is not possible to discriminate the effect of changes in strain and temperature. Therefore, a reference is required for temperature measurement.

Several methods have been addressed in the literature for an accurate discrimination between these two parameters [17–19]. The most straightforward way is to use a separated, strain-free FBG, which acts as a temperature sensor. In this case, the wavelength shift, $\Delta\lambda_{B1}$, is related to temperature variations, ΔT_1, according to:

$$\Delta\lambda_{B1} = k_{T1}\Delta T_1, \tag{4}$$

where k_{T1} is the temperature sensitivity of the non-fixed FBG. This reference FBG is in the same thermal environment as the other sensors, which simultaneously detect strain and temperature.

Assuming that the wavelength-shifts to strain and temperature are linear, a response to a strain change, $\Delta\varepsilon_2$ and a temperature change, ΔT_2, is given by:

$$\Delta\lambda_{B2} = k_{\varepsilon 2}\Delta\varepsilon_2 + k_{T2}\Delta T_2, \tag{5}$$

where $k_{\varepsilon 2}$ and k_{T2} are the strain and temperature sensitivities of the fixed FBG [11], determined in the calibration procedure. Therefore, using Equation (4), the wavelength variations detected by the strain-free FBG can be converted into temperature variations. These temperature variations are then considered in Equation (5), allowing the determination of strain.

2.3 Experimental setup

A network of five FBG sensors, recorded in two different fibers, was placed in direct contact with the LIB surface on the *x*- and *y*-directions, as schematized in Fig. IV.1. The FBGs network used in the monitoring system, with estimated gratings length of ~3.0 mm, was pre-fabricated in our lab and written in commercial photosensitive single mode fiber (125 µm of cladding diameter) (FiberCore PS1250/1500) by the phase mask method. The UV radiation system used was a pulsed excimer laser (KrF) (Industrial Bragg Star, Coherent,

California, USA), emitting at a wavelength of 248 nm, 4 mJ/pulse (20 ns duration), and 500 Hz repetition rate.

As can be seen in Fig. IV.1, the FBG1 was placed on the *x*-direction, FBG4 on the *y*-direction and FBG3 out of the battery to monitor the external room temperature. These sensors were only used to measure temperature variations, as they were not fixed to the battery.

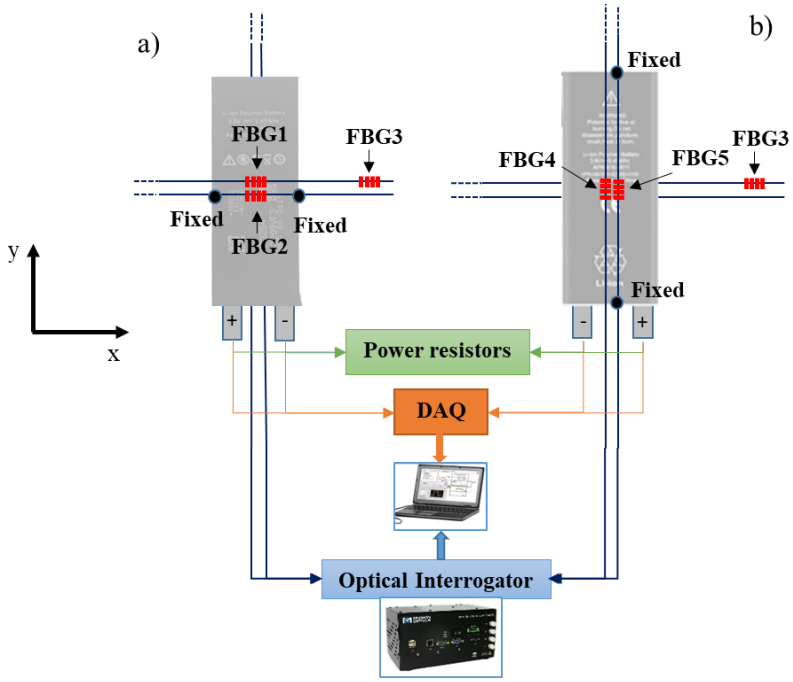

Figure IV.1. Experimental setup diagram of the temperature and bi-directional strain monitoring system of the battery: a) down view; b) top view.

The simultaneous detection of the strain and temperature variations was accomplished by fixing a second fiber side by side to the first one, with two sensors: FBG2 and FBG5. This fiber was pre-tensioned and fixed to the battery on its extremities, along the LIB *x*- and *y*-directions. Thermal paste was placed along both fibers to increase thermal conductivity between the battery and the FBGs. To calculate the length variations on the two directions, the distance between the two fixed points was considered. As the glue was placed as close to the edge of the LIB as possible, the length variations are related to the battery dimension.

The LIB used in this work was a commercial hard prismatic rechargeable smartphone LIB (Iphone 5G Battery, Singapore) with an open-circuit voltage of 4.30 V, nominal capacity of 1440 mAh, cut-off voltage of 3.20 V, dimensions of 8.6 (length) × 3.0 (width) × 0.3 cm (thickness), and mass of 23.47 g. Inside the aluminum–plastic pouch, the internal structure is constructed by winding the ribbon-like electrode and separator to form a "jelly-roll" structure. The negative and positive active materials are coated on each side of the separator materials, and thin layers of copper and aluminum foils are used as the current collectors [4].

Prior to the fiber sensor network's attachment to the LIB, a calibration to strain and temperature was carried out. The strain characterization was performed using a micrometric translation stage between 0 με and 2000 με. The sensors thermal calibration was made on a thermal chamber (Model 340, Challenge Angelantoni Industrie, Massa Martana, Italy). The temperature range was between 20.0 °C and 50.0 °C, in steps of 5.0 °C. The temperature and strain sensitivities obtained are presented in Table IV.1.

Table IV.1. Temperature and strain sensitivities of the FBG sensors.

FBG	Direction	λ_B/nm	$k_T \pm 0.01$/ pm / °C	$k_\varepsilon \pm 0.01$/ pm/με
1	*x*	1553.57	7.92	-
2	*x*	1553.32	7.92	1.16
3	Room temperature sensor	1540.17	8.04	-
4	*y*	1535.70	7.80	-
5	*y*	1535.42	7.80	1.20

The reflected Bragg wavelengths were measured with an optical interrogator (sm125-500, Micron Optics Inc., Atlanta, USA) operating at 2.0 Hz and wavelength accuracy of 1.0 pm. The voltage signal was monitored using a 12-bit resolution data acquisition system (DAQ) (USB6008, National Instruments, Texas, USA). The acquisition modules were controlled by a LabVIEW® customized application, allowing the real-time monitoring of the acquired data.

The LIB was cycled twice under two different discharge rates of 1.32 C and 5.77 C (where 1.00 C is the rate of the ideal capacity charge/discharge in 1 h) through two power resistors of 2.0 Ω and 0.47 Ω until a voltage of 1.95 V was reached. A normal charge rate of 0.70 C

was applied, using a commercial battery charger with output voltage of 5.00 V (ETA0U83EWE, Samsung, Vietnam).

3. Results and discussion

The temperature variations registered by the FBG sensors placed on the two sides of the battery are presented in Fig. IV.2 and IV.3. The positive and negative electrodes indicated in the figures correspond to the sensors placed on the *y*- and *x*-directions, respectively. The cycling protocol, where the discharge rate of 1.32 C was applied, is shown in Fig. IV.2.

Over the CC charge step (1), a maximum temperature variation of 1.29 ± 0.13 °C was measured by the sensors placed on the positive electrode side, whereas on the negative electrode side, the maximum temperature shift was of 0.86 ± 0.13 °C. Between the constant current (CC) charge/discharge steps, constant voltage (CV) steps (2) of 10 min and 15 min were selected to stabilize the temperature and relax the battery.

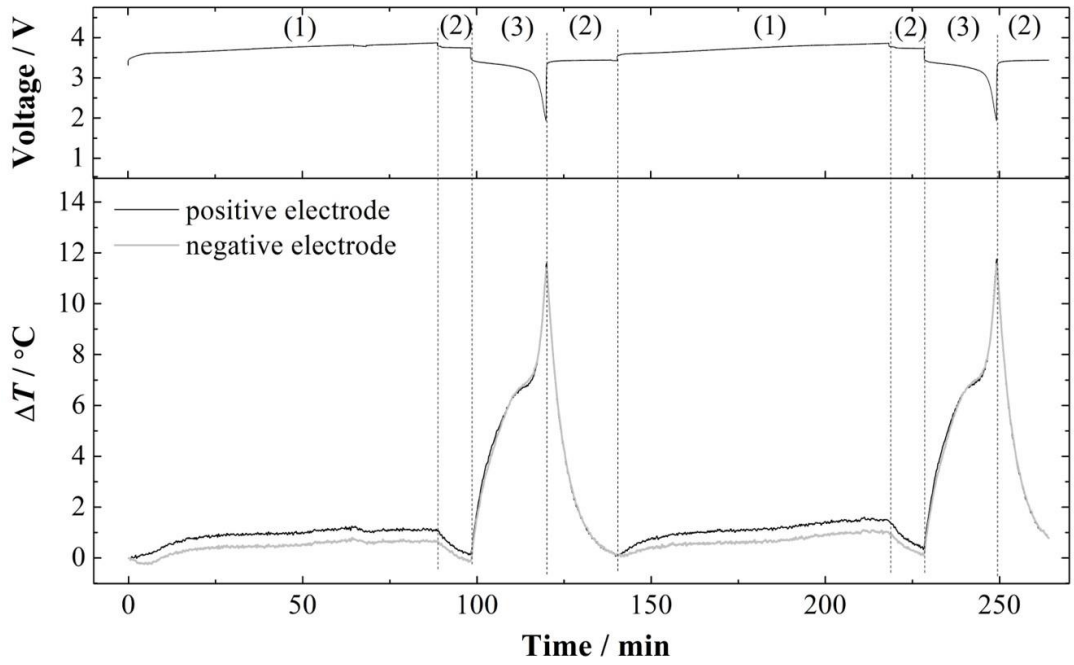

Figure IV.2. Voltage and temperature variations recorded during two cycling tests, in the sides of the positive and negative electrodes of the battery. (1) CC charge; (2) CV; (3) CC discharge at 1.32 C.

The starting of the CC discharge step (3) causes an instantaneous increase on the battery surface temperature, however, the maximum temperature shift was achieved only at the end of the discharge process. These fast and significant increases are related to the larger electrochemical reactions produced by the flow of Li^+ on migration to the positive electrode. During all the discharge steps, two different moments of temperature variations can also be observed. The first moment occurs when the LIB voltage crosses the cut-off voltage, and the second between the cut-off and the end of the discharge process. The maximum temperature variations detected were very similar on both electrodes, around 11.50 ± 0.13 °C.

Figure IV.3 shows the cycling protocol where a discharge rate of 5.77 C was applied. Attending to the CC charge steps (1) and comparing with previous cycling protocol, the same range of values was registered by the FBG sensors located on the positive and negative electrodes. As expected, the main difference was in the temperature variations achieved during the CC discharge step (3).

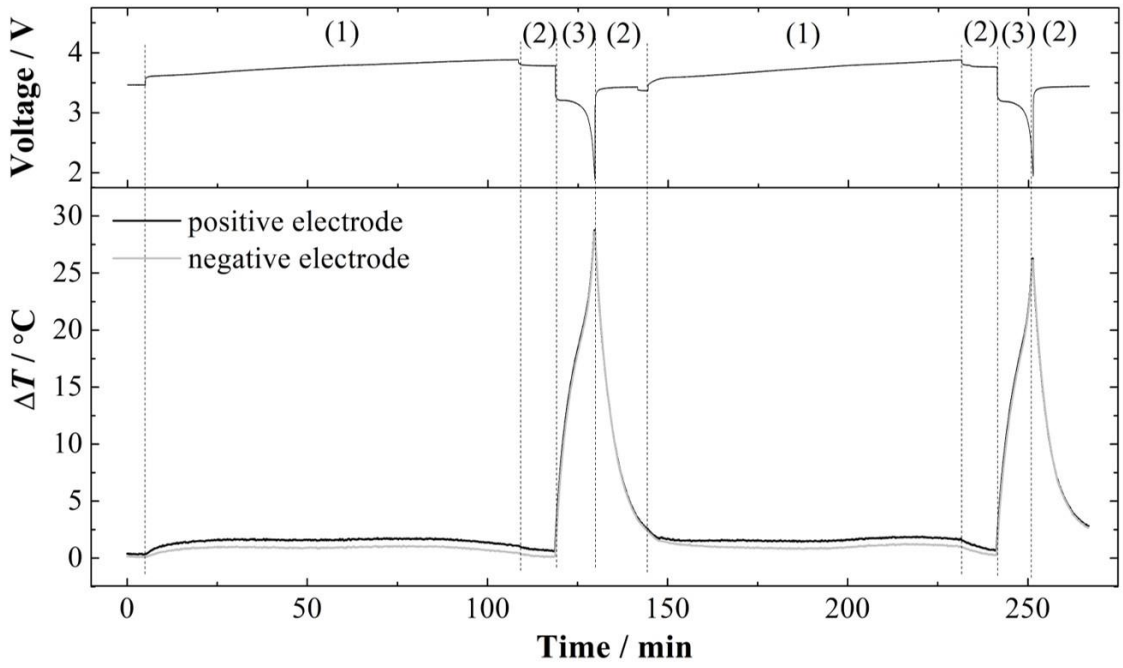

Figure IV.3. Voltage and temperature variations recorded during two cycling tests, in the sides of the positive and negative electrodes of the battery. (1) CC charge; (2) CV; (3) CC discharge at 5.77 C.

In all discharge steps, a monotonic increase can be observed, until the LIB reaches 1.95 V. A maximum temperature variation of 27.52 ± 0.13 °C was recorded on the positive electrode side by the FBG4. On the negative electrode side, an inferior ΔT value of 27.25 ± 0.13 °C was obtained, however, this difference is not significant, taking the measurement error into account.

The bi-directional strain variations detected by the FBG sensors on the *x*- and *y*-directions, during the experimental cycling protocol with the discharge rate of 1.32 C, as well as their voltage signal, are presented in Fig. IV.4. Over the CC charge steps (1), mean strain variations of 122.49 ± 0.83 με and 29.61 ± 0.86 με were measured on the *y*- and *x*-directions, respectively, when the battery reached the 3.95 V. As already mentioned, during the 10 min CV step (2), between the CC charge (1) and CC discharge (3) steps, a relaxation occurs on the battery. This relaxation was higher on the *y*-direction, translating into a strain diminishing of 25.58 ± 0.83 με.

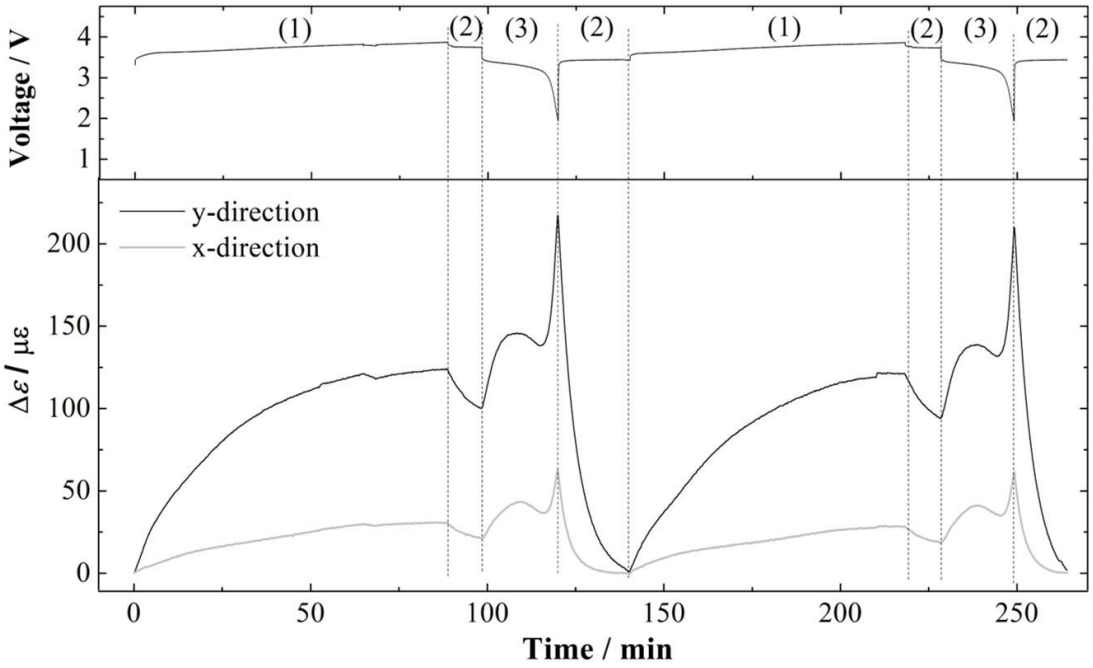

Figure IV.4. Voltage and strain variations recorded during two cycling tests in the battery in the *x*- and *y*-directions. (1) CC charge; (2) CV; (3) CC discharge at 1.32 C.

When the battery is subjected to the CC discharge step (3), at 1.32 C, three different behaviors can be observed on the two different directions. In the first one, until the LIB reached the 3.30 V, there is a sudden increase of strain. In the *y*-direction this increase is nearly two-times higher than the one measured in the *x*-direction. After this, a strain decreases of 7.39 ± 0.83 με and 6.46 ± 0.86 με was measured in the *y*- and *x*-directions, respectively, until the cut-off voltage was reached. This was followed by a fast increase of strain, as the battery starts to operate under abusive conditions, between 3.20 V and 1.95 V. In this case, the *y*-direction strain increased up to 213.53 ± 0.83 με. On the *x*-direction, a 3.4-times lower strain value was recorded. These values can be converted to length variations (ΔL), by multiplying the strain by the length or the width of the LIB on the *y*- or *x*-directions, respectively. Thus, maximum ΔL of 18.36 ± 0.18 μm and 1.86 ± 0.06 μm on the *y*- and *x*-directions were calculated, respectively. These length variations can be translated to a longitudinal and transversal variation in the battery of 0.021% and 0.006% in the *y*- and *x*-directions, respectively.

The same LIB was submitted to a different cycling protocol test, where a discharge rate of 5.77 C was applied. This higher discharge rate was selected so that the battery would operate under abnormal conditions. However, the same charge rate was used to charge the battery at 3.95 V. The bi-directional strain variations obtained are presented in Fig. IV.5.

Comparatively to the cycling protocol presented previously and attending the CC charge steps (1) and CV steps (2), the same range of $\Delta\varepsilon$ were obtained, causing maximum ΔL of 10.53 ± 0.13 μm and 0.89 ± 0.04 μm in the *y*- and *x*-directions, respectively, and longitudinal and transversal shifts of 0.012% and 0.003%, respectively, on the battery.

When the battery is subjected to CC discharge steps (3), a monotonic increase can be observed in both directions. However, a different increasing time occurs, before and after the battery reached the cut-off voltage, following the fast voltage decrease. On the *y*-direction, a maximum strain variation of 593.58 ± 0.83 με was measured and a correspondent ΔL of 51.05 ± 0.37 μm was calculated. This high elongation translated in a battery longitudinal variation of 0.060%. The sensors located in the *x*-direction followed a similar behavior as in the previous cycling protocol and detected lower strain variations. In this case, a maximum transversal variation of 0.022% was obtained.

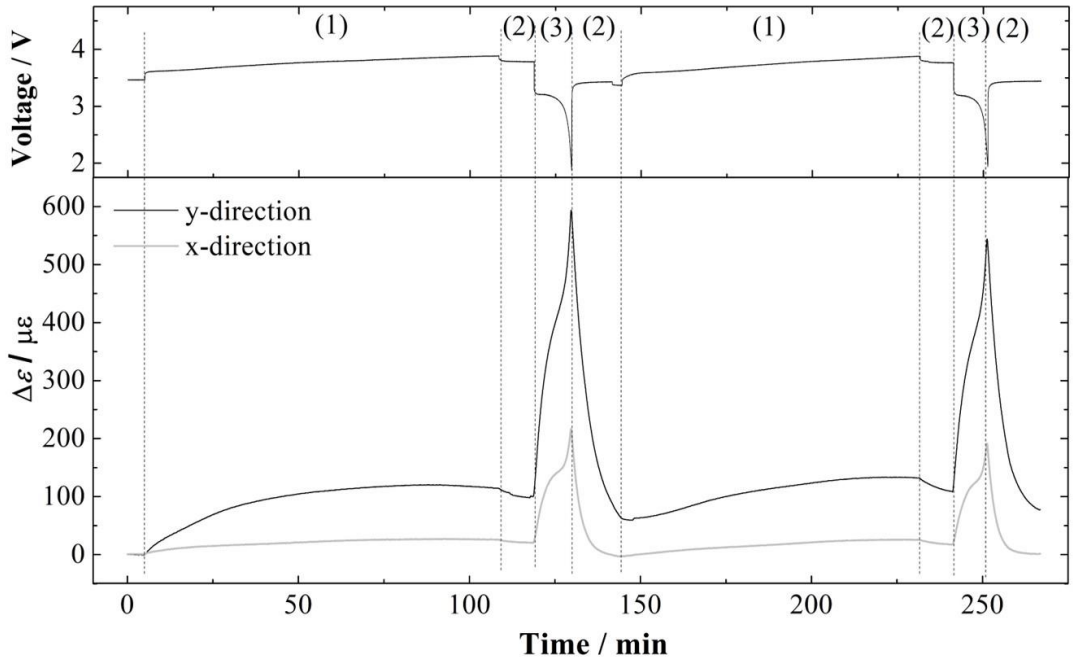

Figure IV.5. Voltage and strain variations recorded during two cycling tests in the battery in the *x*- and *y*-directions. (1) CC charge; (2) CV; (3) CC discharge at 5.77 C.

In all cycles, it was observed that the maximum strain variations are registered when the battery discharge process ends. A relation between the different discharge rates which are applied and the longitudinal and transversal variations on the LIB can be performed by considering the battery dimensions and the ΔL values obtained in the two directions.

For instance, the ratio of the LIB dimensions is 2.87, whereas dividing the longitudinal by the transversal variation measured over the higher discharge rate, a ratio of 2.73 is calculated. Making the same analogy but for the discharge rate of 1.32 C, a ratio value of 3.50 is obtained. This means that the expansion and contraction of the internal 'jelly roll' structure that constitutes the prismatic battery behaves differently on each charge/discharge process which is subject, and it is not proportional to the LIB dimensions.

Through a complete analysis of the cycling test, it is evident that, in both cases, the maximum values obtained for the temperature and strain variations agree with the sudden decrease of the voltage. Considering all strain and temperature values measured, different behaviors in terms of direction of expansion and temperature variations on the two sides of

the battery were detected. These results are in good agreement with the ones found in the literature [6,9,10].

The monitoring of the internal and external parameters during charge and discharge cycles, combined with battery management systems, seems to be adequate to improve overall safety. They also could be used to determine realistic operating conditions and geometries, towards more stable cell pack designs.

4. Conclusions

A network of FBG sensors was successfully used to simultaneously monitor temperature and bi-directional (*x*- and *y*-direction) strain in a prismatic rechargeable LIB, under an experimental cycling protocol with normal CC charge and different CC discharge steps (1.32 C and 5.77 C).

When the battery was subjected to abnormal operating conditions, as fast discharge and operating below the cut-off voltage, it is evident that higher temperature and strain variations occur, which are promoted by the rapid Li^+ transport between the positive and negative electrodes. Over the CC charge step, maximum temperature and strain variations were reached at the end of the process, with values of 1.29 ± 0.13 °C in the positive electrode side and 122.49 ± 0.83 με and 29.61 ± 0.86 με on the *y*- and *x*-directions, respectively.

During the CC discharge step, the higher strain and temperature values of 593.58 ± 0.83 με and 27.52 ± 0.13 °C were respectively registered for the higher discharge rate and when the LIB voltage was lower. These values also relate to the *y*-direction and positive electrode side and correspond to a battery longitudinal expansion of 0.060%. As expected, there is a deformation increase when the temperature also increases, due the thermal expansion of the materials that compose the battery.

Thus, the internal structure of the battery is an important parameter to have in consideration and can influence the behavior of battery materials in terms of expansion and contraction over its operation. The presented sensing network proved to be an effective, precise, alternative solution to real time monitor, multipoint and *operando* temperature and bi-directional strain changes in the LIBs promoting their safety.

Author Contributions: All authors contributed equally. M.N. and M.S.F. conceived the experiments and analyzed the data. All authors wrote and revised the paper.

Acknowledgments: This work was funded by FEDER funds through the COMPETE 2020 Program and National Funds through FCT2014 Portuguese Foundation for Science and Technology under the project UID/CTM/50025/2013. Micael Nascimento and Marta S. Ferreira are also grateful for research fellowships BI/UI96/6642/2016 and SFRH/BPD/124549/2016, respectively.

Conflicts of Interests: The author declares no conflicts of interest.

References

[1] Zhang, Z.; Ramadass, P.; Fang, W. Safety of Lithium-ion Batteries. In *Lithium-Ion Batteries: Advances and Applications*, 1st ed.; Elsevier: Amsterdam, The Netherlands, 2014; Volume 18, pp. 409–435, ISBN: 978-0-444-59513-3.

[2] Spotnitz, R.; Franklin, J. Abuse behavior of high-power, lithium-ion cells. J. Power Sources 2003, 113, 81–100, DOI: 10.1016/S0378-7753(02)00488-3.

[3] Mankowski, P.J.; Kanevski, J.; Bakirtzian, P.; Cugno, S. Cellular phone collateral damage: A review of burns associated with lithium battery powered mobile devices. Burns 2016, 42, e61–e64, DOI: 10.1016/j.burns.2015.10.012.

[4] Yih-Shing, D.; Kai, H.L.; Chen-Shan, K. Experimental investigation and visualization on thermal runaway of hard prismatic lithium-ion batteries used in smart phones. J. Therm. Anal. Calorim. 2018, 1–16, DOI: 10.1007/s10973-018-7077-2.

[5] Leung, P.K.; Moreno, C.; Masters, I.; Hazra, S.; Conde, B.; Mohamed, M.R.; Dashwood, R.J.; Bhagat, R. Real-time displacement and strain mappings of lithium-ion batteries using three-dimensional digital image correlation. J. Power Sources 2014, 271, 82–86, DOI: 10.1016/j.jpowsour.2014.07.184.

[6] Wang, Q.; Ping, P.; Zhao, X.; Chu, G.; Sun, J.; Chen, C. Thermal runaway caused fire and explosion of lithium ion battery. J. Power Sources 2012, 208, 210-24, DOI: 10.1016/j.jpowsour.2012.02.038.

[7] Mutyala, M.S.K.; Zhao, J.; Li, J.; Pan, H.; Yuan, C.; Li, X. In situ temperature measurement in lithium-ion battery by flexible thin film thermocouples. J. Power Sources 2014, 260, 43–49, DOI: 10.1016/j.jpowsour.2014.03.004.

[8] Fu, Y.; Lu, S.; Li, K.; Liu, C.; Cheng, X.; Zhang, H. An experimental study on burning behaviors of 18650 lithium ion batteries using a cone calorimeter. J. Power Sources 2015, 273, 216–222, DOI: 10.1016/j.jpowsour.2014.09.039.

[9] Panchal, S.; Dincer, I.; Agelin-Chaab, M.; Fraser, R.; Fowler, M. Experimental temperature distributions in a prismatic lithium-ion battery at varying conditions. Int. Commun. Heat Mass Transf. 2016, 71, 35–43, DOI: 10.1016/j.icheatmasstransfer.2015.12.004.

[10] Xianming, W.; Yoshitsugu, S.; Go, S.; Hitoshi, N.; Chisa, Y.; Koichi, K. Understanding volume change in Lithium-ion cells during charging and discharging using in situ measurements. J. Electrochem. Soc. 2007, 154, A14–A21, DOI: 10.1149/1.2386933.

[11] Grattan, K.T.V.; Meggitt, B.T. Optical Fiber Sensor Technology: Applications and Systems; Kluwer Academic Publishers: London, UK, 1999; Volume 3, pp. 357–363, ISBN: 978-1-4757-6077-4.

[12] Yang, G.; Leitão, C.; Lib, Y.; Pinto, J.L.; Jiang, X. Real-time temperature measurement with fiber Bragg sensors in lithium batteries for safety usage. Measurement 2013, 46, 3166–3172, DOI: 10.1016/j.measurement.2013.05.027.

[13] Nascimento, M.; Novais, S.; Leitão, C.; Domingues, M.F.; Alberto, A.; Antunes, P.; Pinto, J.L. Lithium Batteries Temperature and Strain Fiber Monitoring. In Proceedings of the 24th International Conference on Optical Fiber Sensors, Curitiba, Brazil, 28 September–2 October 2015; Volume 9634 96347V-1, DOI: 10.1117/12.2195218.

[14] Sommer, L.W.; Kiesel, P.; Ganguli, A.; Lochbaum, A.; Saha, B.; Schwartz, J.; Bae, C.-J.; Alamgir, M. Fast and slow ion diffusion processes in lithium-ion pouch cells during cycling observed with fiber optic strain sensors. J. Power Sources 2015, 296, 46–52, DOI: 10.1016/j.jpowsour.2015.07.025.

[15] Novais, S.; Nascimento, M.; Grande, L.; Domingues, M.F.; Antunes, P.; Alberto, A.; Leitão, C.; Oliveira, R.; Koch, S.; Kim, G.T.; et al. Internal and external temperature monitoring of a Li-ion battery with fiber Bragg grating sensors. Sensors 2016, 16, 1394, DOI: 10.3390/s16091394.

[16] Nascimento, M.; Ferreira, M.; Pinto, J.L. Real time thermal monitoring of lithium batteries with fiber sensors and thermocouples: A comparative study. Measurement 2017, 111, 260–263, DOI: 10.1016/j.measurement.2017.07.049

[17] Jin, W. Simultaneous measurement of strain and temperature: Error analysis. Opt. Eng. 1997, 36, 598, DOI: 10.1117/1.601233.

[18] James, S.W.; Dockney, M.L.; Tatam, R.P. Simultaneous independent temperature and strain measurement using in-fibre Bragg grating sensors. Electron. Lett. 1996, 32, 1133–1334, DOI: 10.1049/el:19960732.

[19] Guan, B.O.; Tam, H.Y.; Tao, X.M.; Dong, X.Y. Simultaneous strain and temperature measurement using a superstructure fiber Bragg grating. IEEE Phot*onics Technol. Lett.* 2000, *12*, 675–677, DOI: 10.1109/68.849081.

Additional information – Proceeding published in the 26th International Conference on Optical Fiber Sensors, OFS26, 24 - 28 September, Lausanne, Switzerland, 2018.

Part of the work described in this Chapter was presented in the Conference OFS26. In this Section, some additional information regarding a different cycling protocol used for the same battery, and that was discussed in the Conference Proceedings, is given.

The LIB was cycled twice under abusive discharge rate of 2.67 C through a power resistor of 1.0 Ω until a voltage of 1.95 V was reached. This voltage value was selected to operate the LIB in abnormal discharge conditions. A normal charge rate of 0.70 C was applied, using a commercial battery charger with output voltage of 5.00 V.

The temperature, strain and the correspondent displacement variations detected by the FBG sensors on the parallel direction, during the experimental cycling protocol applied to the battery, as well as their voltage signal, are presented in Fig. IV.6. Between the constant current (CC) charge/discharge steps (2), constant voltage (CV) steps of 10 min and 15 min were selected to stabilize the battery temperature.

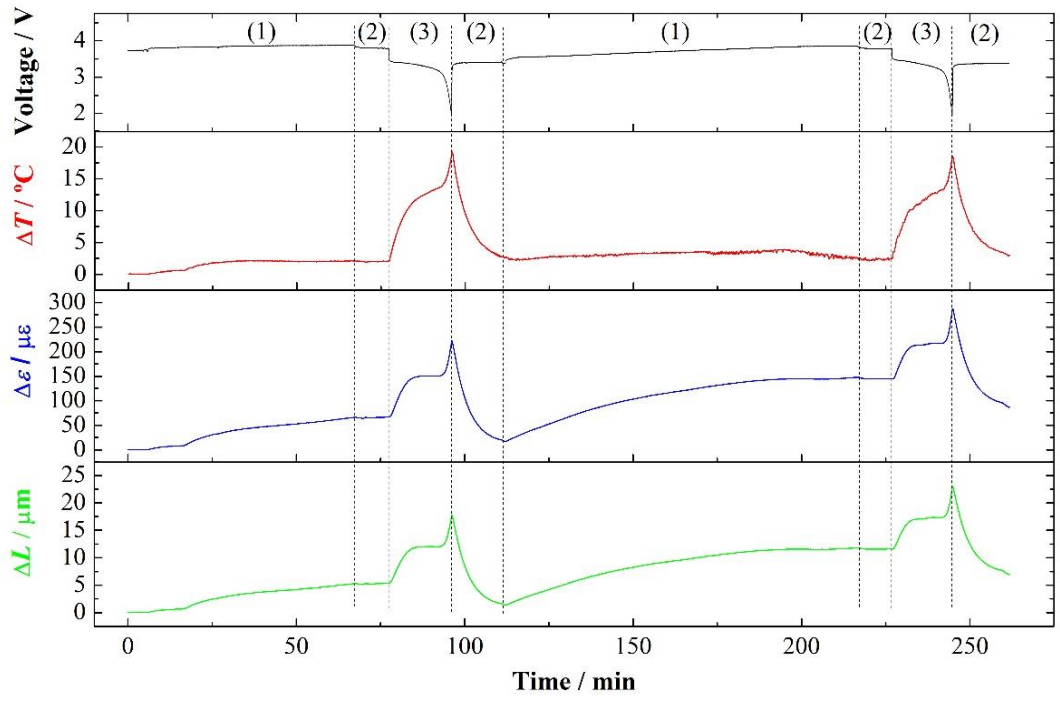

Figure IV.6. Voltage, temperature, strain and displacement variations recorded during two cycling tests in the battery in the parallel direction. (1) CC Charge; (2) CV; (3) CC Discharge.

During the CC charge step (1), maximum ΔT of (3.75 ± 0.13) °C was registered. Regarding the strain values, maximum $\Delta\varepsilon$ of (147.32 ± 0.83) με was recorded in the end of the second CC charge step and a correspondent ΔL of (11.82 ± 0.15) μm was calculated.

When the battery is subjected to a CC discharge step (3), two different behaviours can be observed. There is a sudden increase of temperature and strain until the LIB reached the cut-off voltage, where ΔT values of (11.33 ± 0.13) °C, $\Delta\varepsilon$ of (82.01 ± 0.83) με, and ΔL of (6.56 ± 0.11) μm were detected. These parameters increase even more when the battery is operating under abusive conditions, between 3.20 V and 1.95 V. In this case, the ΔT of (5.80 ± 0.13) °C, $\Delta\varepsilon$ of (71.63 ± 0.83) με, and ΔL of (5.74 ± 0.11) μm were registered. However, between the 3.35 V and 3.20 V, when the temperature increases slightly, the $\Delta\varepsilon$ remains constant. Attending to the maximum temperature and strain variations over the whole experimental cycling protocol, higher values of (19.21 ± 0.13) °C and (287.35 ± 0.83) με were measured when the voltage of the battery is lower.

Figure IV.7 presents the results obtained in the perpendicular direction. Under this direction, on the CC charge step (1), maximum ΔT of (3.92 ± 0.13) °C was measured, whereas on the CC discharge step (3), maximum ΔT of (19.43 ± 0.13) °C was registered. Attending that the sensors in this direction are placed on the side where the positive electrode of the battery is located, the higher temperatures registered when compared to the opposite side are expected.

Comparatively to the parallel direction, lower $\Delta\varepsilon$ and consequently ΔL values were measured. Over the CC charge steps (1), a maximum $\Delta\varepsilon$ value of (53.22 ± 0.86) με was recorded and a correspondent displacement of (1.48 ± 0.05) μm was calculated. When the battery is subjected to CC discharge steps (3), two continuous increasing times can also be observed in all sensors. On this direction, $\Delta\varepsilon$ of (74.01 ± 0.86) με and ΔL of (2.08 ± 0.06) μm were detected.

On the second increase, until the battery discharge process ends, $\Delta\varepsilon$ of (55.53 ± 0.86) με and ΔL of (1.56 ± 0.05) μm were registered. However, between the voltage values of 3.35 V and 3.20 V, a small relaxation of the battery of (14.14 ± 0.86) με was observed. As expected, there is a deformation increase when the temperature also increases, due the thermal expansion of the materials that compose the battery.

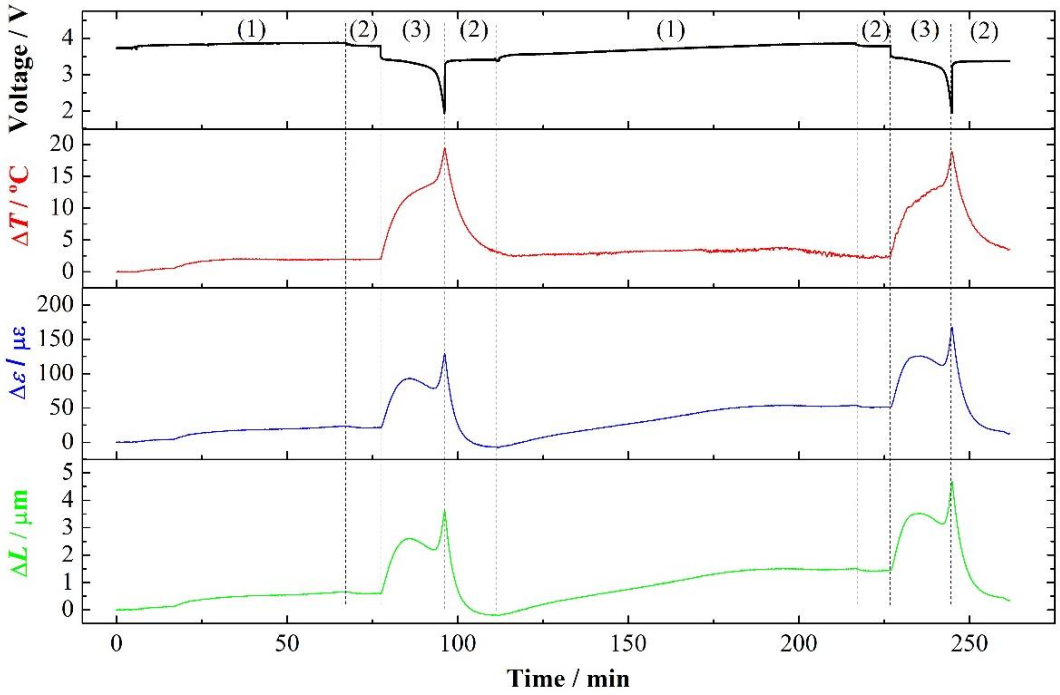

Figure IV.7. Voltage, temperature, strain and displacement variations recorded during two cycling tests in the battery in the perpendicular direction. (1) CC Charge; (2) CV; (3) CC Discharge.

Through a complete analysis of the cycling test, it is evident that, in both cases, the maximum values obtained for the temperature and strain variations agree with the sudden decrease of the voltage. These strain variations can be translated in a battery longitudinal variation of 0.017% and 0.013% in the parallel and perpendicular directions, respectively. Considering these values, a different behaviour in terms of direction of expansion of the battery was detected.

Chapter V

Temperature fiber sensing of Li-ion batteries under different environmental and operating conditions

Published in *Applied Thermal Engineering*, 2019, 149, 1236-1243

DOI: 10.1016/j.applthermaleng.2018.12.135

Temperature fiber sensing of Li-ion batteries under different environmental and operating conditions

Micael Nascimento, Marta S. Ferreira, and João L. Pinto

Abstract

In this work, a network of fiber sensors has been developed for real time, *in situ*, and *operando* multipoint monitoring the surface temperature distribution on a smartphone Li-ion battery (LIB). Different temperature and relative humidity conditions are considered, in order to mimic the LIB response in the dry, temperate, and cold climates. In total, the temperature variations that occur in five different locations of the LIB are monitored, during constant current charge and different discharge rates, under normal and abusive operating conditions, performing a thermal spatial mapping of the battery surface. In general, the sensors detect temperature variations according to the voltage signal change and faster variations of voltage usually translate in higher temperature rise at the LIB surface. For instance, under abusive discharge, where the voltage drop is fast, the temperature increases at least twice when compared to the normal operating conditions. Absolute temperature values as high as (65.0 ± 0.1) °C are detected by the optical sensor located near the electrodes, under the higher discharge rate (5.77 C) and dry climate. A thermal gradient is identified from the top to the bottom on the LIB surface during the experimental tests. A lower battery performance is observed when it operates under the cold climate, with maximum temperature variations of (30.0 ± 0.1) °C for the higher discharge rate. These results can be helpful to design of next generation of LIBs, improving a faster cooling in critical areas, in order to reduce accumulated heat and preventing consequences such as thermal runaway and failure.

Keywords: Li-ion batteries; Fiber Bragg grating sensors; Temperature monitoring; Environment; Abnormal operating conditions; Safety.

1. Introduction

Li-ion batteries (LIBs) have been widely used as power sources for a wide range of electronic devices such as smartphones, cameras, and laptops, and are considered to be the

ideal power sources for next generation vehicles, electric vehicles and hybrid electric vehicles, ensuring optimized conditions in the perspective of energy, power and self-discharge parameters [1-3]. However, this technology still has some relevant issues of safety, running costs, recycling, charging and thermal management, with great impact in the overall LIB performance [4].

Between all safety issues, thermal runaway is a fundamental issue, which is reproduced by the rapid increasing of temperature. This increase produces heat energy at a rate faster than heat can be dissipated followed by a collapse of the LIB internal separator components, resulting in local short-circuiting [5]. Furthermore, accumulated heat in the batteries brings concerns of performance drops and safety hazards [6].

Through the charge-discharge process, high temperature typically consequences in the failure of batteries and even more seriously, fire and explosion accidents. LIB powered cellular devices have recently received media attention for an apparent increase in "exploding smartphones", where half of the cases identified involved thermal injuries sustained from battery malfunction [7]. Good thermal management systems are thus becoming essential for providing good performance and autonomy.

To reach out a satisfactory thermal management solution some cooling methodologies can be applied. They are dependent upon a number of factors, such as the level of heat to be dissipated, the maximum allowable component temperatures, the operating environment, the available space, reliability, and cost [8]. For low profile scales the design of cooling solutions becomes a challenge and new ideas, new strategies, and approaches should be considered. Examples of technologies for thermal management are air and liquid cooling [9], micro heat pipes [10], high conductivity materials such as carbon substrates [11], and phase change materials [12].

The motivation of these technologies is upon heat spreading and transport within a device rather than the active removal of heat from the device. For example, liquid cooling, heat pipes, and high conductivity materials only provide paths of reduced thermal resistance for the flow of heat within the devices, while the phase change materials store the heat to be dissipated over time. Hence, heat is ultimately removed by some combination of natural convection, conduction and radiation [8].

Although these technologies present some efficiency in terms of batteries thermal management, they still have some constraints. The liquid cooling system is more effective, but it presents a higher complexity, cost, and also potential leakage. Heat pipe cooling is limited by gravity, weight, and passive control. The addition of phase change materials could raise undesirable mass and/or volume and it is still necessary to drain the heat absorbed during continuous cycling [13].

However, some of these problems would be solved if these technologies were associated with a best knowledge of the spatial thermal mapping of the batteries under different real time operating conditions, in order to improve the thermal management of all battery system. This association would reduce the quantity of materials required on the battery system to effectively dissipate the heat generated and could lead to the development of new designs of LIB thermal management.

The behavior of LIB at low temperatures has been questioned by different authors in the literature, including the impact of different environmental temperature in electric vehicles autonomy. Heating strategies for LIB operated from subzero temperatures were already investigated by employing an electrochemical-thermal coupled model. It was suggested that AC heating should be used for external power heating, being an internal heating strategy that provides uniform heat [14]. The low temperature performance was studied by Zhang *et al*., who concluded that the cycling performance of a LIB is affected by the total impedance of the cell [15]. The driving autonomy of a 2012 Nissan Leaf has been reported decreasing from 220 km to 100 km, for temperatures varying from -10.0 °C to 0 °C [14].

Electrochemical models and simulations were also used to investigate the charge and discharge behaviors of LIB in low environmental temperatures [16, 17]. Furthermore, the temperature variations of the LIB surface were monitored with attached thermocouples, at different discharges rates [18]. Andreev *et al*. performed a simulation of the LIB operation under severe temperature conditions typically found in Russia. The authors concluded that the lower environmental conditions influence the internal resistance and the available discharge capacity [19].

Overall, the poor battery performance at cold temperatures has been related to an increase of the internal resistance, due to the interdependence of thermal and electrochemical processes. In fact, the cell temperature evolution is dependent of the electrochemical

processes through the heat generated and dissipated to the environment and, consequently, it affects the transport and kinetic properties in the electrochemical processes. Generally, low environmental temperatures seem to be associated with a decrease of chemical reactions, causing relevant changes in charge kinetics, electrolyte conductivity, and lithium ions diffusivity within the anode, affecting the overall LIB performance.

In order to ensure optimized and safe conditions of operation under different environments, it is necessary to predict and monitor through an analysis and modeling of the thermal behavior of LIB. Most of the previous works were focused on monitoring temperature on LIB using thermocouples in strategic locations and through estimation methods. The thermocouples have the advantages of having small dimensions, of being self-powered and ease of handling.

Wang *et al*. studied the internal temperature evolution of coin LIB during charge and discharge process, using resistance temperature sensors. They concluded that measuring the internal temperature is faster and more accurate than the surface temperature [20]. Twelve thermocouples were used to study the internal temperature inside a large-format laminated battery under different thermal boundary conditions, where the direction for the improvement of cell thermal design and the ways for effective thermal management were identified [21].

Transferable flexible thin film thermocouples were also embedded inside the LIB to measure temperature at high charging and discharging rates [22]. Panchal *et al*. attached 3 and 10 T-type thermocouples in a surface of a prismatic lithium battery to study uneven temperature and voltage distributions at rapid discharge rates and different boundary conditions. A comparison with simulated tests was also performed. They concluded that the temperature distribution of the cells increased as the C-rates increase, and it was higher near electrodes. However, this type of thermocouples presents uncertainty of 1.0 °C and several thermocouples were needed, resulting in a complex and bulky measurement setup [23, 24]. However, it is still necessary to develop novel thermal management systems with rapid heat dissipation to keep both the electronic components and the LIB working under the optimum temperature range.

Recent works have proposed the use of fiber Bragg grating (FBG) sensors as an alternative method to monitor temperature attached to the surface of LIB, due to their

intrinsic characteristics, such as small dimensions, capability of multiplexing, chemical inertness, passivity (no need of electrical power to operate), and the possibility of optimized integration inside the batteries [25]. Furthermore, these sensors present faster response rates and higher accuracy, under normal and abusive operating conditions. They also have the ability to monitor simultaneously multi-parameters such as temperature, strain, and pressure [25].

The performance of the thermocouples and FBG sensors has been increasingly questioned and confronted in terms of response rates and accuracy, under normal and abusive operating conditions. In a recent study, a comparative response of both type of sensors was analyzed, where it was concluded that the FBG presents better resolution and lower rise time than the thermocouples, making them a better choice for the real time monitoring of the battery surface temperature as well as a useful tool for failure detection and an optimized management in batteries [26].

Yang *et al*. had also integrated FBG sensors in a coin LIB to measure real time temperature variations during the battery's operation under normal and abnormal conditions. The FBG sensors exhibited good thermal responses to dynamic loading when compared with the thermocouples [27]. A network of FBG sensors was integrated in a lab scale Li-ion pouch cell to monitor simultaneously and *operando*, internal and external temperature variations, where the temperature evolution during galvanostatic cycling at different C-rates was analyzed. The authors concluded that the low invasiveness and high tolerance to the chemically aggressive environment of the FBG sensors inside the LIB make them an interesting possibility for integration on these batteries [28]. Sommer *et al*. had also integrated FBG sensors to monitor strain and temperature during fast and slow ion diffusion processes in lithium ion pouch cells [29].

These works reveal that FBGs can be an optimal, low cost, and non-active tool to support and improve the LIB thermal management, by obtaining a spatial thermal mapping of the battery surface, as well as to detect which are the areas that can heat more or even the existence of hot spots. Furthermore, these sensors can also help in the development of new designs and intrinsic materials to be integrated on the batteries.

In this study, an optical fiber sensing network based on FBGs is developed to real time, *in situ* and *operando* monitor the thermal performance in five different points of a

rechargeable smartphone LIB under different environments, constant current charge and different discharge rates. An analysis of the thermal behavior of a LIB under different environmental conditions typical of the temperate, dry, and cold climates through the temperature and relative humidity (RH) variations in a controlled environment is presented, to the best of our knowledge, for the first time.

2. Materials and methods

2.1 Materials

A commercial rechargeable smartphone LIB (Iphone 5G Battery, Singapore) with maximum voltage of 4.3 V, nominal capacity of 1440 mAh and dimensions of 130 mm (length) × 90 mm (width) × 30 mm (height), was used. The temperature variations were monitored with a network of five FBGs, glued on the surface of the battery in five strategic positions (top, top-middle, middle, middle-bottom, and bottom) in order to evaluate the temperature variations throughout the LIB surface.

The FBGs (length of 3.0 mm), spaced by 18.0 mm, were recorded in photosensitive single mode fiber (PS1250/1500, FiberCore), using an UV excimers laser and the phase mask method. Typically, these sensors can operate from -150 °C up to 350 °C without damaging the sensor reflection signal.

2.2 Experimental setup

A schematic diagram of the experimental setup for real-time temperature smartphone LiB monitoring is shown in Fig. V.1. The optical fiber sensors response was measured with a standard optical interrogator (sm125-500, Micron Optics Inc.) operating at 2.0 Hz and with wavelength accuracy of 1.0 pm. The voltage was real-time measured, with a USB6008 NI DAQ, 12-bit resolution and customized LabVIEW® application. During all tests, the battery with the attached sensors was kept inside a standard thermal chamber (Model 340, Challenge Angelantoni Industrie), whereas the remaining components (power resistors, DAQ, and optical interrogator) were placed on the outside.

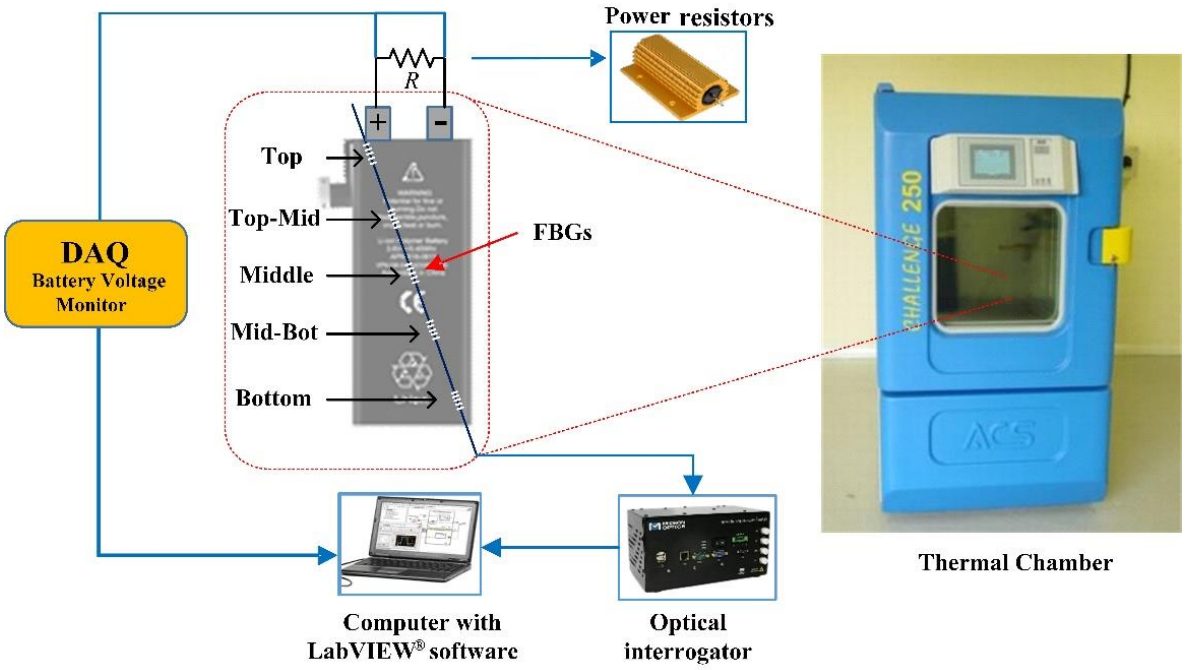

Figure V.1. (left) Schematic of rechargeable smartphone LIB test setup with the location of FBGs and (right) thermal chamber used.

2.3 Sensors thermal calibration

The sensors were previously calibrated on the thermal chamber in a temperature range from 10.0 °C up to 100.0 °C, with 10.0 °C steps. Figure V.2 presents the spectra attained for two different temperatures, 10.0 °C and 50.0 °C.

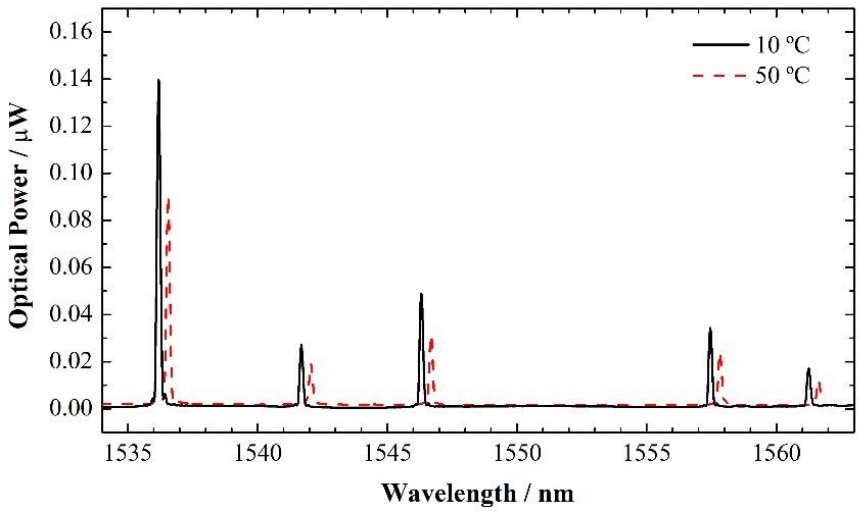

Figure V.2. Spectra of the FBG sensors network at two different temperatures.

The shift towards longer wavelengths (red shift) with the increase of temperature, a behavior typical of this type of sensors, can be observed. Notice that each peak corresponds to a different sensing element, however all of them are in the same optical fiber.

Table V.1 indicates the Bragg wavelength (λ_B) at room temperature and the sensitivities (k_T) obtained by the thermal calibration. Through the equation $\Delta\lambda = k_T \times \Delta T$, where $\Delta\lambda$ is the wavelength shift, it is possible to determine the temperature variation (ΔT) detected by the sensors.

Table V.1. Fiber sensors position with the respective Bragg wavelength at 20.0 °C and sensitivities obtained through the calibration.

FBG position	**λ_B / nm**	**k_T / pm/°C**
Top	1536.23	9.08
Top-Middle	1541.77	9.14
Middle	1546.21	9.17
Middle-Bottom	1557.35	9.24
Bottom	1561.55	9.29

Considering the calculation of the standard deviation between the maximum and minimum fluctuations of the sensors signals, acquired over 1 h on the thermal chamber with stabilized temperature an experimental resolution of 0.1 °C was determined for the FBGs. It should be highlighted that these sensors are not sensitive to external RH variations, thus no compensation towards this parameter is required [30].

2.4 Environmental conditions

According to the Köppen-Geiger classification, there are five major climate groups on our planet: tropical, dry, temperate, cold, and polar [31]. Depending on the method, the climatic zones can be identified by combining different parameters, such as, temperature, precipitation, RH, and radiation [32]. In this study, the temperature and RH were considered as these parameters could be simultaneously controlled in the thermal chamber.

Table V.2 shows the values considered during the experiments to study the influence of

three different environmental conditions on the LIB thermal behaviour and performance.

Table V.2. Typical mean values of temperature and RH for each climate selected for this study.

Environment	Temperature / °C	RH / %
Dry	40.0	20.0
Temperate	18.0	50.0
Cold	7.0	75.0

2.5 Battery test procedure

To perform the cycling tests on the LIB, a charge rate of 0.70 C was performed, using a commercial battery charger with output voltage of 5.0 V (ETA0U83EWE, Samsung, Vietnam). Different discharge rates (1.32 C, 2.67 C, and 5.77 C) were used, in order to monitor the battery performance and behavior under normal and abnormal operating conditions. Three different power resistors (10 W) were employed, with an equivalent resistance of 2.00 Ω, 1.00 Ω, and 0.47 Ω.

The battery test procedure, shown in Fig. V.3, was selected in order to promote abusive operating conditions on the battery. In all cycling tests, the battery was discharged until a voltage of 0.5 V was reached.

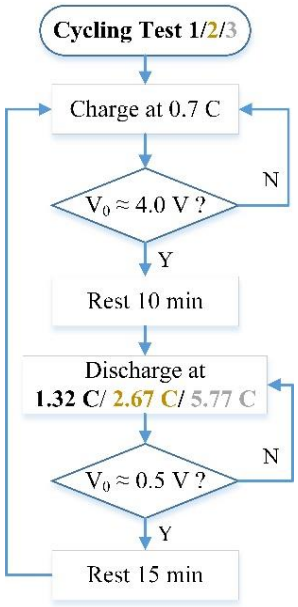

Figure V.3. Cycling tests flowchart for each discharge rate, 1.32 C (cycling test 1), 2.67 C (cycling test 2), and 5.77 C (cycling test 3).

Between the charge/discharge steps, a resting time was selected in order to stabilize the battery temperature. Each discharge rate was repeated several times and the results were consistent throughout the experiments.

3. Results and discussion

Figure V.4 shows the output voltage variation as the battery was subjected to the different cycling tests, for each environmental condition selected. A total of six cycles are presented, two for each discharge rate. Between the temperate and dry environments there is no significant change in the time that the cycles take to occur. However, when the battery is exposed to the cold environment, the time that the battery took to perform the same cycles was ~35% lower when compared to the other two environments. This is an indicator of the lower performance of the battery under these conditions.

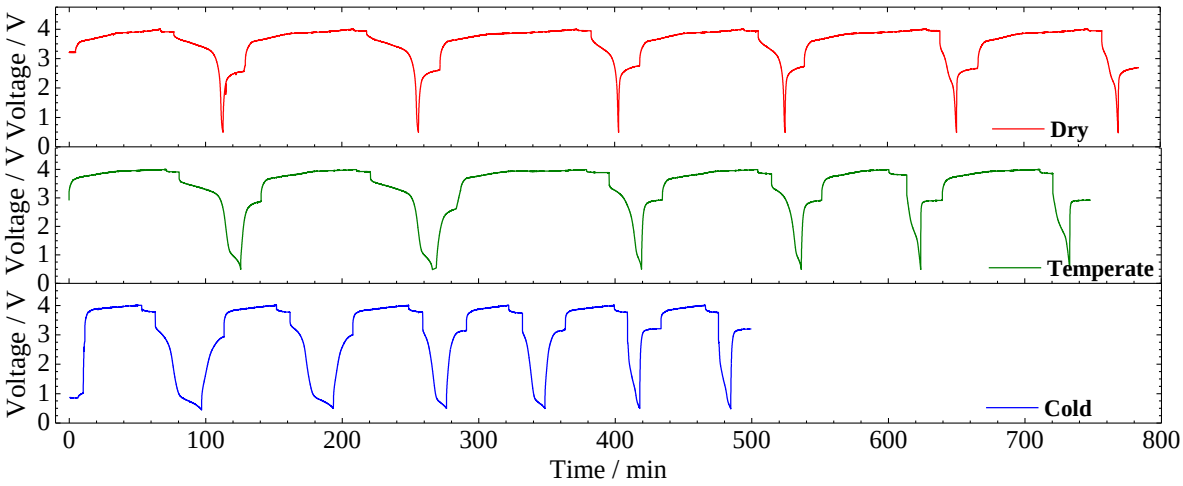

Figure V.4. Voltage signal variations during the cycling tests under the environments selected.

This behavior is highlighted in Fig. V.5, where a single cycle was considered for each environment. The charging time depends on the environmental conditions (Fig. V.5 a)). The 4.0 V were achieved after 37 min, 70 min and 80 min for the cold, temperate and dry environments, respectively. Concerning the discharging behaviour, there is a notorious influence of cold environment when compared to the dry and temperate climate conditions (Fig. V.5 b)).

Considering the voltage that the LiB presented after the resting time (~4.0 V), and for 1.32 C, there is a nearly instantaneous drop in voltage to 3.8 V and 3.7 V for the dry and temperate environments, respectively. From this point on, the voltage variation is slower, as it takes ~30 min for the voltage to reach the cut-of voltage (3.2 V) (normal operating conditions), following the typical discharge behaviour of a LIB. As expected, the discharge rate increase leads to a faster discharge and, in the case of 5.77 C this behaviour is no longer observable. After this plateau there is a fast voltage decrease until the discharge process end (abnormal operating conditions).

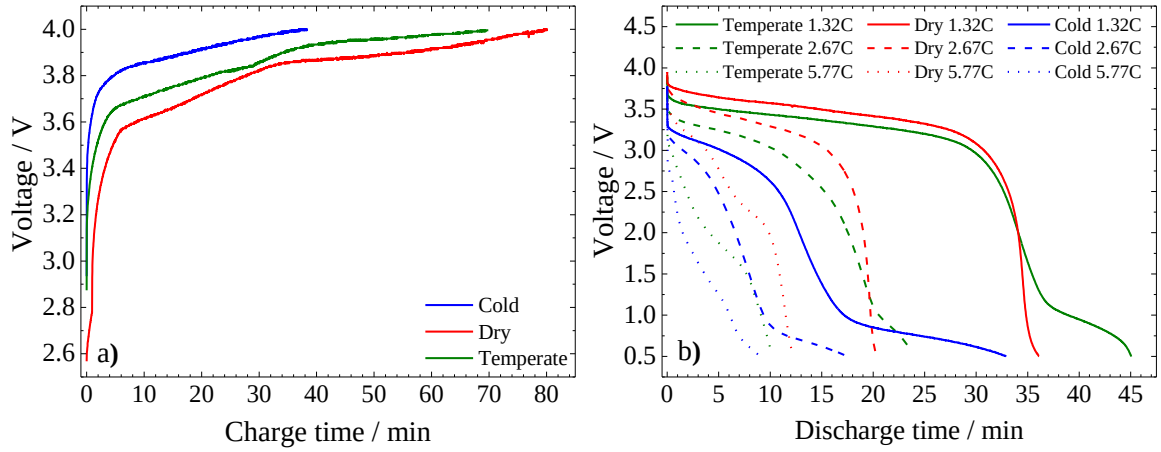

Figure V.5. a) Charge time and b) three different discharge rate times, during the first cycle and respective voltage signal, under different environmental conditions.

Considering the behaviour until the cut-off voltage, a higher performance of the LIB under the environmental condition typical of the dry climates is observed, possibly due to the decrease of the battery internal resistance with the increase of the external temperature together with the low relative humidity (40.0 °C; 20.0 %RH). This behaviour was consistent throughout the cycling experiments in each type of environment.

A significantly different behaviour was observed regarding discharge voltage response when the LIB was subjected to the environmental conditions typical of cold weather. For instance, at 1.32 C, after only ~1 min the LIB achieved the cut-off voltage, followed by the fast decrease until 0.5 V. Increasing the discharge rate led to an even faster discharge (it took less than 10 s to drop from 4.0 V to 3.2 V). It should be highlighted that the lower battery performance in this case, is in accordance with the literature [5-9].

The FBG sensors responses during the cycling tests under different environmental conditions and the corresponding battery voltage are shown in Fig. V.6.

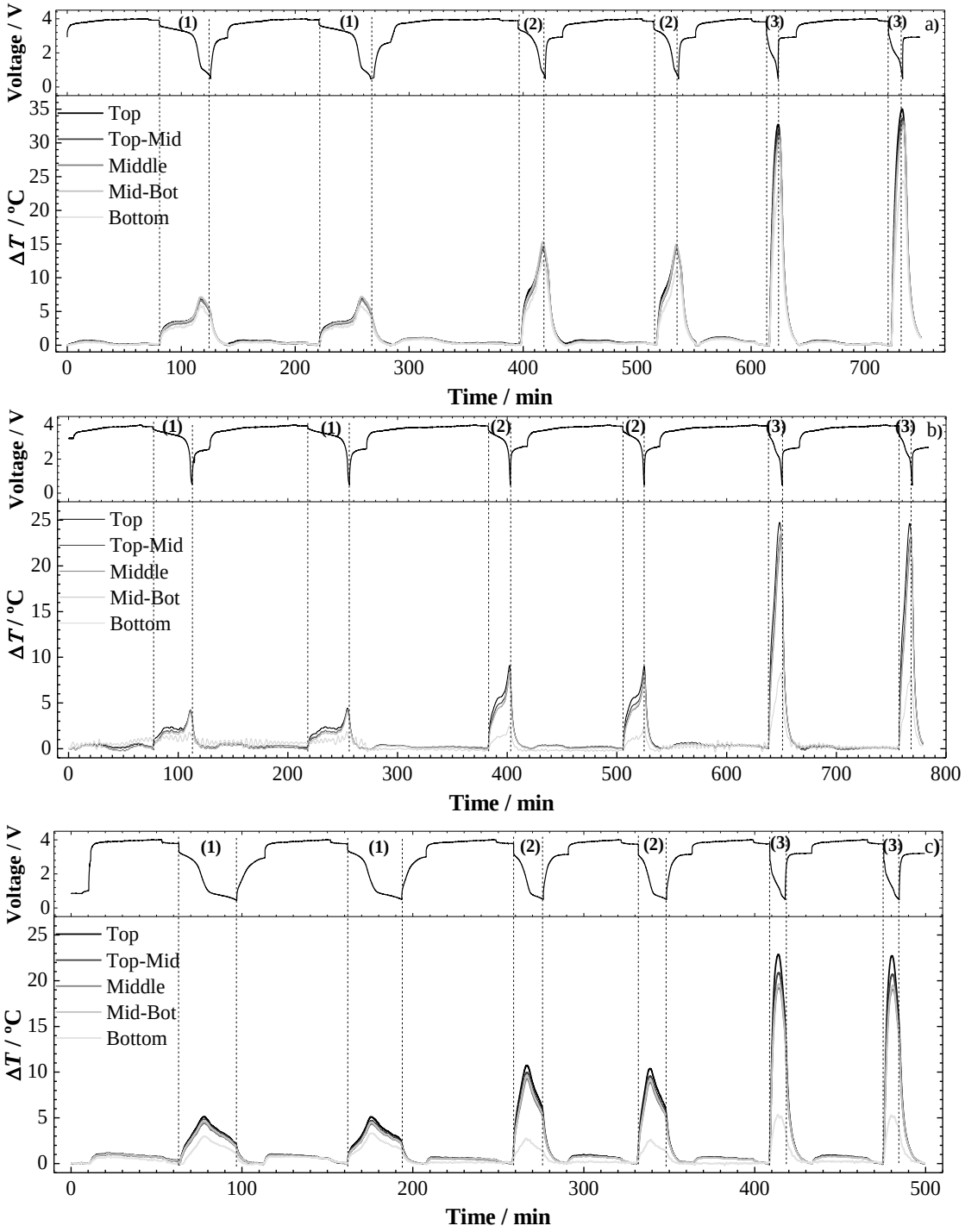

Figure V.6. Surface temperature variations during the cycling tests under the environmental conditions typical of the a) temperate , b) dry, and c) cold climates. Five different positions are considered: top, top-middle, middle, middle-bottom, and bottom. The discharge rates are also indicated, (1) 1.32 C, (2) 2.67 C, and (3) 5.77 C.

During the charge process, an increase of (1.0 ± 0.1) °C was registered in all cycles until the battery charged up to ~98.8%. Above this value and until the maximum voltage was achieved (4.0 V), the temperature decreased once again to room temperature. It was observed, in all cases, that during the discharge process a significant temperature rise occurs as the discharge rate increases.

Regarding the surface temperature variations when the LIB was exposed to the temperate environmental conditions, shown in Fig. V.6 a), the presence of two shoulders in the temperature peaks is observed during the discharge rate of 1.32 C and 2.67 C. For the lowest discharge rate, the first shoulder occurred until the LIB achieved the cut-off voltage. There was a sudden temperature increase of (3.0 ± 0.1) °C (coincident with the fast voltage drop from 3.9 to 3.7 V), followed by a slower variation. Once the battery achieved the abnormal operating regime, and due to the fast voltage drops, a larger temperature increase was registered. For this environmental condition, absolute temperatures of (25.0 ± 0.1) °C, (35.0 ± 0.1) °C and (53.0 ± 0.1) °C were detected by the FBG sensors placed near the electrodes for the discharge rates of 1.32 C, 2.67 C and 5.77 C, respectively. As can be seen in Fig. V.5 b), at 5.77 C the voltage drop until 3.2 V is very fast. Thus, the temperature variation measured presented only one shoulder, which was due to the abnormal operating conditions. Overall, the behaviour was the same in the five positions, meaning that the voltage variation translates into similar temperature shifts regardless of the sensor location.

Increasing the temperature to 40.0 °C and decreasing the RH to 20.0% led to lower temperature variations when compared to the previous case (see Fig. V.6 b)). The peaks shape is like the ones presented in Fig. V.6 a), for the sensors located between the top and the middle-bottom position. The sensor located at the bottom presented a discrepant response, which was attributed to an unintentional change in the fiber position during this experiment, and, consequently, a poor contact between the LIB and this FBG. This also influenced the results obtained under the cold environment. Absolute temperature values of (65.0 ± 0.1) °C were achieved for the top FBG sensor under the higher discharge rate.

The environmental temperature decreases and RH increase, typical of cold climates, translated in lower ΔT, as can be seen in Fig. V.6 c). A maximum temperature shift of (23.0 ± 0.1) °C was registered by the sensor located in the top, at 5.77 C (under abnormal operating conditions). It can also be observed that at 5.77 C, a significant difference of

(2.0 ± 0.1) °C was detected between the sensors placed on the top and top-middle, and (3.2 ± 0.1) °C between the top and middle. Notice that the temperature varies accordingly to the voltage profile, increasing as the voltage drops to 1.0 V and slowly decreasing until the voltage reaches 0.5 V. This behaviour is more pronounced for the lowest discharge rate and can be related to a poorer performance of the battery under these environmental conditions, as well as a possible slowdown of the electrochemical reactions, translating into a decrease in the discharge capacity and power capabilities.

Figure V.7 highlights the temperature variation dependence with voltage under the three discharge rates, which was detected by the top FBG under different environments. It is possible to observe that for the highest discharge rate the maximum temperature shift (which occurs, as aforementioned, during abnormal operating conditions) is detected at higher voltages than for the other discharge rates. Notice that in this figure the time factor is not considered, which can be misleading. For instance, observing the 2.67 C curve in Fig. V.7 b), from 4.0 V to 3.2 V the temperature increased (6.0 ± 0.1) °C in 12 min.

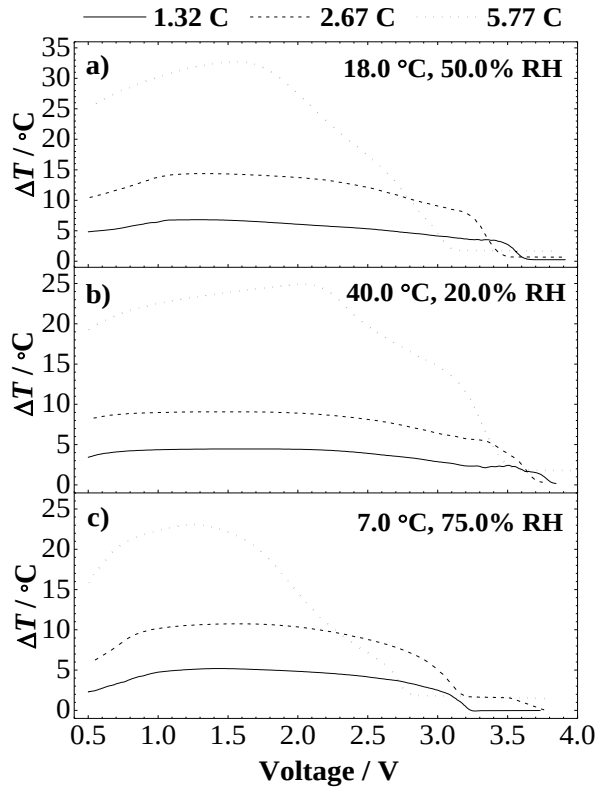

Figure V.7. Temperature dependence with the voltage under the three discharge rates, monitored by the FBG located on the top considering the different environments.

Between the cut-off voltage and 0.5 V, it further increased (3.0 ± 0.1) °C, however, this step only took 8 min. In fact, faster variations of voltage usually translate in higher temperature variations at the LIB surface.

The temperature detected by the sensors at the cut-off voltage, in all positions, for the different environmental conditions under study is summarized in Fig. V.8. Notice that, in this figure, only the two lowest discharge rates for the dry and temperate climates, and the results regarding 1.32 C for the cold climate, are shown. This is due to the fact that at 5.77 C and 2.67 C, under the cold environment, the voltage drop from 4.0 V to 3.2 V was very fast and the setup used did not present enough resolution to be able to detect such variation in terms of temperature.

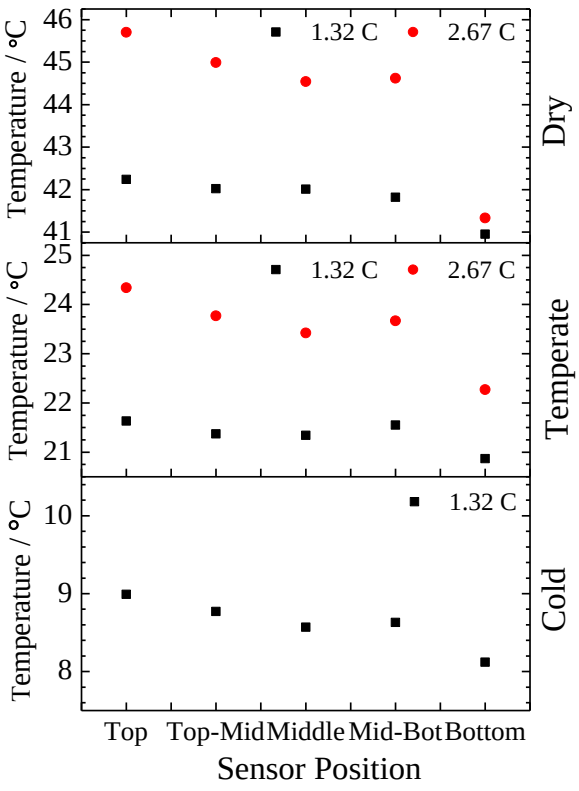

Figure V.8. Higher surface temperatures detected by all the FBGs at the cut-off voltage, under the three environments during the discharge rates of 1.32 C and 2.67 C.

In all cases, the highest temperature detected was at the top (near the electrodes), followed by the top-middle position. The temperature at the middle-bottom was slightly higher than at the middle, contrary to what was expected. However, the difference is relatively small of the order of the experimental resolution (< 0.1 °C) and can be ignored. Finally, the temperature detected at the bottom of the LIB was lower in all cases.

For the temperate and dry environments, average temperature differences of (3.0 ± 0.1) °C and (2.3 ± 0.1) °C were, respectively registered between the discharge rates of 2.67 C and 1.32 C, being this difference higher near of the electrodes, successively decreasing until the bottom position, becoming evident the existence of a thermal gradient on the battery.

The decrease was significantly higher for 2.67 C (dry environment), coincident with the already mentioned unintentional movement of the fiber, which also influenced the result for the cold environmental conditions. Nevertheless, the temperature profile measured in this work is in good agreement with results reported in the literature for polymer LIB [18, 20].

4. Conclusions

A network of optical fiber sensors was successfully used to monitor external temperature changes in a smartphone LIB, during testing under different environmental conditions at constant charge and different discharge rates (1.32 C, 2.67 C, and 5.77 C). Five different locations were monitored using only a single optical fiber on the battery surface, taking advantage of its multiplexing capability as well as reliability and fast response, performing a thermal spatial mapping of a LIB surface.

To the best of our knowledge, this type of measurements was performed on cell phone LIBs for the first time. This measuring method with FBG sensors proved to be an effective, precise, alternative and easier solution to monitor *in situ*, multipoint and *operando* temperature distributions on the LIB surface. This study quantifies and elucidates which values of temperature are achieved when the battery is exposed to three different environmental conditions and, through a thermal mapping, show which areas of the LIB are necessary to cool faster, in order to improve their performance and thus avoid the occurrence of a thermal runaway.

According to the cycling tests, when the battery is exposed to the cold environment, the time that the battery took to perform the same cycles was ~35% lower when compared to the dry and temperate environments. In general, it was observed that the sensors were able to detect temperature variations which tracked the voltage signal. Faster variations of voltage usually translated in higher temperature variations at the LIB surface, and this effect is evidenced when the LIB operates under abnormal conditions. For instance, temperatures of (65.0 ± 0.1) °C, (53.0 ± 0.1) °C, and (30.0 ± 0.1) °C, were achieved during the higher discharge rate of 5.77 C, when exposed the dry, temperate, and cold climates, respectively.

Under normal operating conditions, the thermal gradient from the top to the bottom was confirmed by the sensors responses, being independent of the type of climate, and relative temperatures of (2.3 ± 0.1) °C and (3.5 ± 0.1) °C were achieved for the dry and temperate climates, respectively, near the electrodes. Under the cold environment a variation of just (1.9 ± 0.1) °C was registered. In general, lower temperature variations were detected when the LIB operated under the cold environment. The higher temperature shifts detected by the FBGs in the other two environments, until 3.2 V, are related with the greater performance of the LIB in terms of discharge capacity and power capabilities, demonstrating that these environmental conditions are the best to operate the LIB in order to extend their lifetimes and promote safety control. This information can be very helpful for the next generation of LIB design, evidencing which areas require a faster cooling to reduce accumulated heat.

The FBGs prove to be a precise and useful tool to promote the optimization of LIB design for different environments and safety in terms of development of new intrinsic materials for the prevention of thermal runaway in the lithium batteries.

Acknowledgments: This work was funded by European project "Stable Interfaces for Rechargeable Batteries "(SIRBATT) (FP7-ENERGY-2013, grant agreement No. 608502) and by FEDER funds through the COMPETE 2020 Programme and National Funds through FCT - Portuguese Foundation for Science and Technology under the project UID/CTM/50025/2013. Micael Nascimento and Marta S. Ferreira are also grateful for research fellowships BI/UI96/6642/2016 and SFRH/BPD/124549/2016, respectively.

References

[1] J. Jaguemont, L. Boulon, Y. Dubé, A comprehensive review of lithium-ion batteries used in hybrid and electric vehicles at cold temperatures, Appl. Energy 164 (2016) 99-114.

[2] S.M. Rezvanizaniani, Z. Liu, Y. Chen, J. Lee, Review and recent advances in battery health monitoring and prognostics technologies for electric vehicle (EV) safety and mobility, J. Power Sources 256 (2014),110-124.

[3] Z. Zhang, P. Ramadass, W. Fang, Safety of lithium-ion batteries, Lithium-ion batteries: Advances and applications 18 (2014), 409-435.

[4] T.M. Bandhauer, S. Garimella, T.F. Fuller, A critical review of thermal issues in lithium-ion batteries, J. Electrochem. Society 158 (2011), R1-R25.

[5] L.S. Guo, Z.R. Wang, J.H. Wang, Q.K. Luo, J.J. Liu, Effects of the environmental temperature and heat dissipation condition on the thermal runaway of lithium ion batteries during the charge-discharge process, J. Loss Prevent Proc (2017), In Press.

[6] Z. Ling, Z. Zhang, G. Shi, X. Fang, L. Wang, X. Gao, Y. Fang, T. Xu, S. Wang, X. Liu, Review on thermal management systems using phase change materials for electronic components, Li-ion batteries and photovoltaic modules, Renew. Sust. Energ. Rev. 31 (2014), 427-438.

[7] P.J. Mankowski, J. Kanevski, P. Bakirtzian, S. Cugno, Cellular phone collateral damage: A review of burns associated with lithium battery powered mobile devices, Burns 42 (2016),e61-e64.

[8] R. Grimes, E. Walsh, P. Walsh, Active cooling of a mobile phone handset, Appl. Therm. Eng. 30 (2010), 2363-2369.

[9] G. Kim, A. Pesaran, Battery thermal management design modeling, World Electr. Veh. J 1 (2007), 126-133.

[10] Q. Wang, B. Jiang, Q. Xue, H. Sun, B. Li, H. Zou, Experimental investigation on EV battery cooling and heating by heat pipes, Appl. Therm. Eng. 88 (2015),54-60.

[11] A. Babapoor, M. Azizi, G. Karimi, Thermal management of a Li-ion battery using carbon fiber-PCM composites, Appl. Therm. Eng. 82 (2015), 281-290.

[12] N. Javani, I. Dincer, G.F. Naterer, G.L. Rohrauer Modelling of passive thermal management for electric vehicle battery packs with PCM between cells, Appl. Therm. Eng. 73 (2014), 307-316.

[13] D. Chen, J. Jiang, G.H. Kim, C. Yang, A. Pesaran, Comparison of different cooling methods for lithium ion battery cells, Appl. Therm. Eng. 94 (2016), 846-854.

[14] Y. Ji, C.Y. Wang, Heating strategies for Li-ion batteries operated from subzero temperatures, Electrochem. Acta 107 (2013), 664-674.

[15] S.S. Zhang, K. Xu, T.R. Jow, The low temperature performance of Li-ion batteries, J. Power Sources 115 (2003), 137-140.

[16] S. Tippmann, D. Wapler, L. Balboa, B. Spier, W.G. Bessler, Low temperature charging of lithium-ion cells part I: Eletrochemical modeling and experimental investigation of degradation behavior, J. Power Sources 252 (2014), 305-316.

[17] J. Yi, U.S. Kim, S. Chee, T. Han, S. Park, Modelling the temperature dependence of the discharge behavior of a lithium-ion battery in low environmental temperature, J. Power Sources 244 (2013), 143-148.

[18] M. Yildiz, H. Karakoc, I. Dincer, Modelling and validation of temperature changes in pouch lithium-ion battery at various discharge rates, Int. Commun. Heat Mass Transfer 75 (2016) 311-314.

[19] A.A. Andreev, A.G. Vozmilov, V.A. Kalmakov, Simulation of lithium battery operation under severe temperature conditions, Procedia Eng. 129 (2016) 201-206.

[20] P. Wang, X. Zhang, L. Yang, X. Zhang, M. Yang, H. Chen, D. Fang, Real-time monitoring of internal temperature evolution of Li-ion coin cell battery during the charge and discharge process, Extreme Mech. Lett. 9 (2016) 459-466.

[21] Z. Li, J. Zhang, B. Wu, J. Huang, Z. Nie, Y. Sun, F. An, N. Wu, Examining temporal and spatial variations of internal temperature in large-format laminated battery with embedded thermocouples, J. Power Sources 241 (2013) 536-553.

[22] M.S.K. Mutyala, J. Zhao, J. Li, H. Pan, C. Yuan, X. Li, In situ temperature measurement in lithium-ion battery by flexible thin film thermocouples, J Power Sources 260 (2014) 43-49.

[23] S. Panchal, I. Dincer, M. Agelin-Chaab, M. Fowler, R. Fraser, Uneven temperature and voltage distributions due to rapid discharge rates and different boundary conditions for series-connected $LiFePO_4$ batteries, Int. Commun. Heat Mass Transfer 81 (2017) 210-217.

[24] S. Panchal, I. Dincer, M. Agelin-Chaab, R. Fraser, M. Fowler, Experimental temperature distributions in a prismatic lithium-ion battery at varying conditions, Int. Commun. Heat Mass Transfer 71 (2016) 35-43.

[25] K.T.V. Grattan, B.T. Meggitt, Optical fiber sensor technology: volume 3: applications and systems. Kluwer Academic Publishers (1999).

[26] M. Nascimento, M. Ferreira, J.L. Pinto, Real time thermal monitoring of lithium batteries with fiber sensors and thermocouples: A comparative study, Measurement 111 (2017) 260-263.

[27] G. Yang, C. Leitão, Y. Lib, J.L. Pinto, X. Jiang, Real-time temperature measurement with fiber Bragg sensors in lithium batteries for safety usage, Measurement 46 (2013) 3166-3172.

[28] S. Novais, M. Nascimento, L. Grande, M.F. Domingues, P. Antunes, A. Alberto, C. Leitão, R. Oliveira, S. Koch, G.T. Kim, S. Passerini, J.L. Pinto, Internal and external temperature monitoring of a Li-ion battery with fiber Bragg grating sensors, Sensors 16 (2016), 1394.

[29] L.W. Sommer, P. Kiesel, A. Ganguli, A. Lochbaum, B. Saha, J. Schwartz, C-J. Bae, M. Alamgir, Fast and slow ion diffusion processes in lithium-ion pouch cells during cycling observed with fiber optic strain sensors, J. Power Sources 296 (2015), 46-52.

[30] B. Gu, M. Yin, A.P. Zhang, J. Qian, S. He, Optical fiber relative humidity sensor based on FBG incorporated thin-core fiber modal interferometer, Optics Express 19 (2011), No.5.

[31] M.C. Peel, B.L. Finlayson, T.A McMahon, Updated world map of the Köppen-Geiger climate classification, Hydrol. Earth Syst. Sc. 11 (2007), 1633-1644.

[32] J.E. Oliver, Encyclopedia of World climatology. Encyclopedia of Earth Sciences Series, (2005), Springer

Chapter VI

Thermal mapping of a lithium polymer batteries pack with FBGs network

Published in *Batteries*, 4(4), 67

DOI: 10.3390/batteries4040067

Thermal mapping of a lithium polymer batteries pack with FBGs network

Micael Nascimento, Tiago Paixão, Marta S. Ferreira, and João L. Pinto

Abstract:

In this work, a network of 37 fiber Bragg grating (FBG) sensors is proposed for real time, *in-situ*, and *operando* multipoint monitoring the surface temperature distribution on a pack of 3 prismatic lithium polymer batteries (LiPBs). With such network, a spatial and temporal thermal mapping of all pack interfaces is performed. In each interface, 9 strategical locations are monitored, by considering a 3×3 matrix, corresponding to the LiPBs top, middle and bottom zones. The batteries are subjected to charge and discharge cycles, where the charge is carried out at 1.0 C, whereas the discharge rates are of 0.7 C and 1.4 C. The results show that, in general, a thermal gradient is recognized from the top to the bottom, being less prominent in the end of charge steps. The results also indicate the presence of hot spots between two of the three batteries, located near the positive tab collector. This occurs due to the higher current density of the lithium ions in this area. The presented FBG sensing network can be used to improve the thermal management of batteries, by performing a spatiotemporal thermal mapping, as well as by identifying which are the zones more conducive to the possibility of existence of hot spots, preventing severe consequences such as thermal runaway and promoting their safety. To the best of our knowledge, this is the first time that a spatial and temporal thermal mapping is reported for this specific application, using a network of FBG sensors.

Keywords: Lithium polymer batteries pack; FBGs network; *in-situ* monitoring; thermal mapping; safety.

1. Introduction

Lithium polymer batteries (LiPBs) are extensively used as rechargeable energy storage systems for a wide range of electronic devices such as smartphones and laptops, due to their high specific energy, power densities, nominal voltage, and low self-discharge rates [1-3].

Exceeding the limits of current, voltage, or power may result in internal battery damage. Possible thermal runaway, characterized by the faster temperature increase, can also occur

if proper precautions are not taken. This is an essential issue, with high impact in the global LiPB behavior. Moreover, LiPBs must be prudently electrically and thermally monitored and managed, to avoid safety and performance issues [4-8]. The internal structure of a LiPB is made-up of multiple layers, forming a "jelly roll" structure, where each layer consists of the anode, cathode, electrolyte, and polymer film separators. Recent studied have been published using new composite polymer electrolytes for solid-state lithium batteries, not only to improve their thermal stability, but also to allow a wide electrochemical stability window and compatibility with the electrodes. These are fundamental requirements for the next generation of reliable large-scale energy storage systems and to develop more completely solid devices [9-12]. Under abnormal conditions, such as temperature exceeding the separators melting point or breakdown of the layered materials, an internal short circuit can occur. The possible hot spots generated by internal short circuit can ignite thermal runaways, leading to fire or explosion of the batteries [8,13,14]. However, some of these problems would be solved if these technologies were associated with a better understanding of the spatiotemporal thermal mapping of the batteries under different and real time operating conditions, improving the thermal management of all battery system.

Temperature can affect both the LiPBs lifetime and energy, and therefore, it should be within an optimum range of temperature, to ensure better performance and long life, both for use and storage [15, 16]. The ability to quantify and evaluate the mechanism of thermal runaway generated during the electrochemical processes that occur, will create a beneficial information regarding their behavior as well as an active tool to promote their safety. The thermal sensing of LiPBs is typically performed using different types of thermocouples in strategic locations [3, 14-24], micro-electro-mechanical systems [25], mathematical models [26,27], and resistance temperature sensors [28, 29]. Generally, for commercialized battery packs, most of the existing methods use single-point temperature monitoring on the cell surface to represent the overall state of the cell [19].

Recent works showed that fiber Bragg gratings (FBG) are an alternative method to realize temperature measurements in lithium batteries. Some of the advantages of using such sensors, when compared to electronic ones, are the ease in multiplexing, fast response, immunity to electromagnetic interference, lower invasiveness, and the small size [30-35]. The research and development of a sensor network based on FBGs has attracted significant interest, because by inscribing several FBGs with different grating periods in the same

optical fiber, a broad selection of sensors can be manufactured. This allows the user to monitor different positions in the structure with only a single fiber. Only one light source is required, and the same interrogation system is employed for different FBGs, effectively decreasing the system cost. Multiple FBG sensors can be readily accommodated and the location of each sensor can be precisely controlled, which is essential to quantitatively distinguish the temperature of different spots [30, 36]. These works reveal that FBGs can be an optimal, low cost, and non-active tool to support and improve the LiB thermal management.

In this work, a sensing network of 37 FBGs is proposed for the detection of temporal and spatial variations of temperature at the interfaces of a pack of 3 prismatic LiPBs. A cycling protocol considering the charge at 1.0 C, and different discharge rates, at 0.7 C and 1.4 C, is performed. The temperature measurements are performed *in-situ* and *operando*.

2. Materials and methods

2.1 Fiber Bragg grating sensors network

A fiber Bragg grating (FBG) sensor consists of a small segment of a single-mode optical fiber (length of a few millimeters) with a photoinduced periodically modulated refractive index in the fiber core. The FBG resonant wavelength, λ_B, is related to the grating period (Λ) and to the effective refractive index of the core mode (n_{eff}) through Eq. (1):

$$\lambda_B = 2n_{eff}\Lambda, \tag{1}$$

When the grating is illuminated with a broadband optical source, the reflected power spectrum presents a sharp peak, which is caused by interference of light with the planes of the grating [31]. When the fiber is exposed to external variations of a given measurand (such as temperature), both n_{eff} and Λ can be changed, producing a shift in λ_B. The FBG sensitivity (k) towards a given parameter is basically obtained by subjecting the sensor to pre-determined and controlled variations of such parameter and measuring the λ_B for each step. The effects of temperature are accounted in the Bragg wavelength shift ($\Delta\lambda$) by differentiating Eq. (1):

$$\Delta\lambda = 2\lambda_B\left(\frac{1}{n_{eff}}\frac{\partial n_{eff}}{\partial T} + \frac{1}{\Lambda}\frac{\partial \Lambda}{\partial T}\right)\Delta T = \lambda_B(\alpha + \xi)\Delta T = k_T\Delta T, \tag{2}$$

where α, ξ, and k_T are the thermal expansion, thermo-optic coefficient of the optical fiber material, and the temperature sensitivity, respectively.

2.2 Experimental setup

The FBGs (length of ~3.0 mm each) were sequentially recorded in four different photosensitive single mode fibers (SMF) (GF1, Thorlabs Inc., Newton, MA, USA), by the phase mask method. A pulsed Q-switched Nd:YAG laser system (LOTIS TII LS-2137U Laser, Minsk, Belarus) lasing at the fourth harmonic (266 nm), focusing the beam in the SMF with a plano-convex cylindrical lens (working length of 320 mm), was used. The reflected Bragg wavelengths were measured with an optical interrogator (sm125-500, Micron Optics Inc., Atlanta, GA, USA) operating at 2.0 Hz and wavelength accuracy of 1.0 pm. Typically, these sensors can operate from -150 ºC up to 350 ºC without damaging the sensor´s reflection signal [37,38]. Figure VI.1 presents the spectrum for one of the fibers, with a total of 10 FBG sensors.

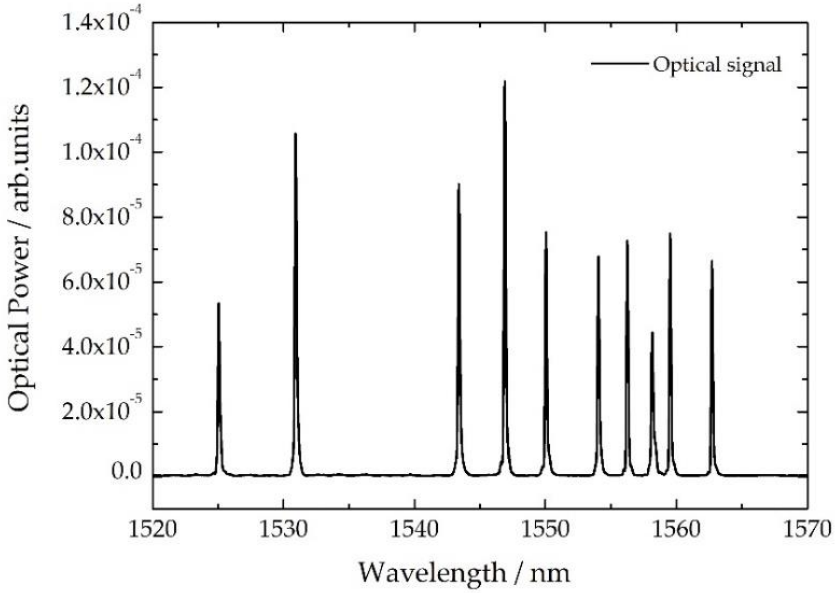

Figure VI.1. Spectra of the 10 FBG sensors network recorded in one fiber.

A thermal calibration was performed prior to attaching the fiber sensors network to the LiPBs pack. The sensors thermal calibration was made using a Peltier device, with a resolution of 0.01 °C. The temperature range was between 20.0 °C and 60.0 °C, in steps of

5.0 °C. Table VI.1 indicates the λB at room temperature and the k_T obtained through the thermal calibration for one fiber. Notice that, in the other fibers, k_T and λ_B of the FBGs are very similar, and are in the same location on the LiPBs. Through equation 2, it is possible to convert the wavelength shifts detected by the sensors into temperature variation (ΔT). Considering the calculation of the standard deviation between the maximum and minimum fluctuations of the sensors signals, acquired over 1 h on the Peltier device with stabilized temperature, an experimental resolution of 0.1 °C was determined for the FBGs.

The position of each FBG, in relation to the battery, is presented in the format of a matrix (*i*.*j*), where *i* = 1,2,3 corresponds to the top, middle, and bottom positions, whereas *j* = 1,2,3 indicates the sensor location on the left, middle and right, respectively.

Table VI.1. Fiber sensors position on the LiPB with the corresponding Bragg wavelengths and sensitivities obtained through the thermal calibration at 20.0 °C.

FBG position	**λ_B / nm**	**k_T ± 0.1 / pm/°C**	**FBG position**	**λ_B / nm**	**k_T ± 0.1 / pm/°C**
Room	1525.05	10.0	(2.2)	1554.06	10.2
(1.1)	1530.92	10.0	(2.3)	1556.25	10.2
(1.2)	1543.39	10.1	(3.1)	1558.17	10.3
(1.3)	1546.91	10.1	(3.2)	1559.52	10.3
(2.1)	1550.05	10.2	(3.3)	1562.71	10.3

Three rechargeable prismatic LiPBs (Cameron Sino Technology, China) with nominal voltage of 3.7 V/cell, nominal capacity of 1600 mAh and dimensions of 79 mm (length) × 54 mm (width) × 4 mm (thickness), were packaged in series, performing a LiPBs pack with a nominal voltage of 11.1 V. The voltage signal was monitored using a 12-bit resolution data acquisition system (DAQ) (USB6008, National Instruments). The acquisition modules were controlled by a LabVIEW® customized application, allowing the real-time monitoring of the acquired data. The LiPBs pack was cycled twice under two different discharge rates of 0.7 C and 1.4 C through two power resistors of 10.0 Ω and 5.0 Ω, respectively, until a cut-off pack voltage of 9.0 V was reached. A fast charge current of 1.0 C was applied, using a commercial Turnigy Accucell-6 balance charger/discharger with maximum current of 5.0 A.

The temperature variations were monitored with a network of 37 FBG sensors, divided by four different optical fibers (9 FBG sensors in each fiber), glued to the surface of the battery in nine strategic locations disposed as a 3x3 matrix, as can be seen in Fig. VI.2.

The extra FBG sensor was used out of the pack to monitor the room temperature variations and thus to eliminate possible external fluctuations. This setup allowed the monitoring of temperature variations throughout the LiPBs pack interfaces on the top, middle and bottom areas. Thermal paste was placed along all fibers to increase thermal conductivity between the battery and the optical sensors.

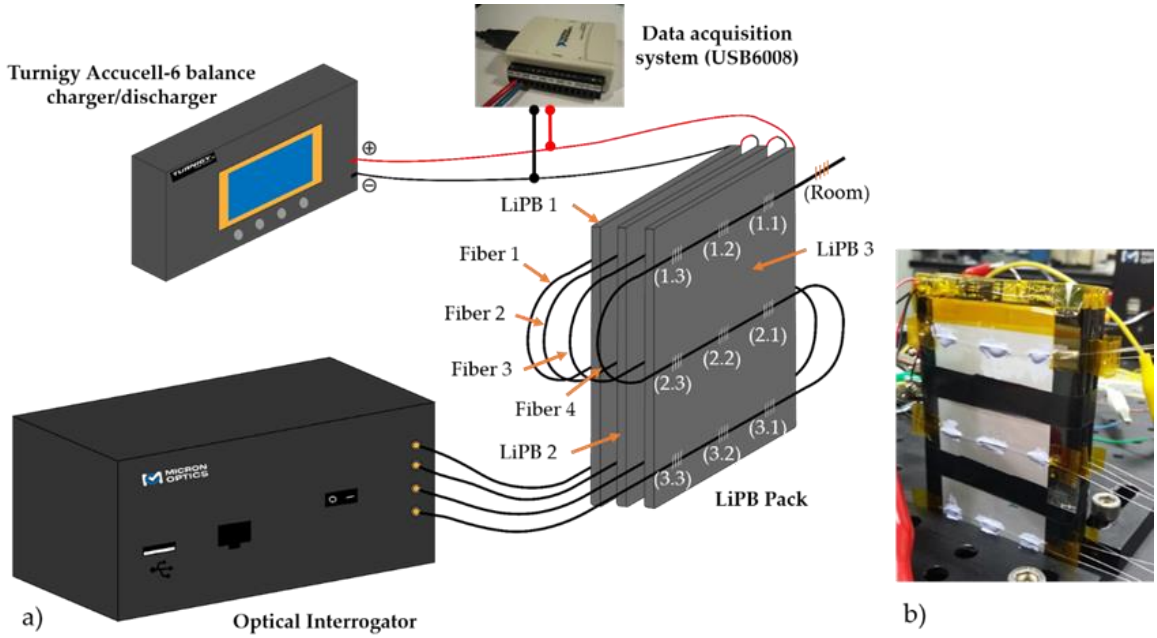

Figure VI.2. a) Experimental setup of the sensing network with the FBG sensors positions used to monitor the LiPBs pack. b) Photograph of the LiPBs pack instrumented with the fiber sensing network.

In total, four interfaces on the LiPBs pack were monitored. The fiber 1 was placed in the surface of the LiPB1 (interface air-LiPB1) (negative electrode surface), the fibers 2 and 3 were sandwiched in the interfaces between the LiPB1 and LiPB2 (interface LiPB1-LiPB2), and LiPB2 and LiPB3 (interface LiPB2-LiPB3), respectively. The fiber 4 was positioned in the other surface of the LiPB3 (interface LiPB3-air) (positive electrode surface).

3. Results and discussion

3.1 Cycling protocols – Voltage and temperature curves

Figure VI.3 presents the voltage signals measured with the DAQ during the cycling tests for each battery that composed the LiPBs pack, under normal and abusive discharge

conditions of 0.7 C (Fig. VI.3 a)) and 1.4 C (Fig. VI.3 b)). In total, four discharge cycles were applied, followed by a fast charge of ~1.0 C in all of them. Between the constant current (CC) charge/discharge steps, a resting time of ~15 min was selected to stabilize the temperature and relax the LiPBs pack. It is important to mention that the cooling of the LiPBs pack during all the cycling tests was performed by natural convection. The intentional short-circuit at the discharge cycle observed in Fig. VI.3 a) was performed to assess the thermal impact at LiPBs pack and its influence on the voltage behavior. After the circuit was reestablished, the LiPBs pack returned to its previous behavior without affecting the posterior data.

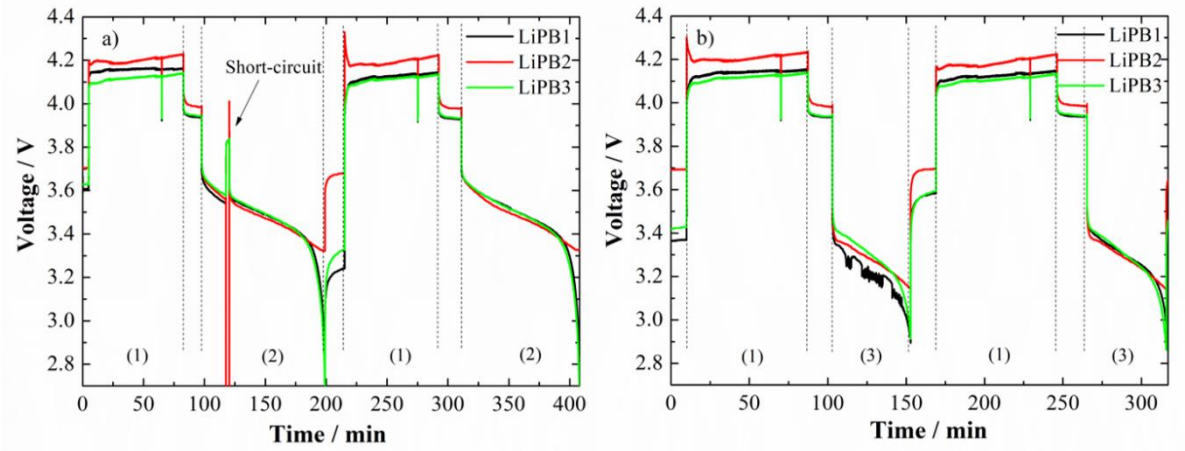

Figure VI.3. Voltage dependence with time for each LiPB, a) at 0.7 C discharge rate and b) at 1.4 C discharge rate. (1) CC charge at 1.0 C; (2) CC discharge at 0.7 C; (3) CC discharge at 1.4 C.

For both discharge rates, the LiPB2 exhibited a better performance, when compared to the other two pack batteries, presenting higher values of voltage and more stable signals. For this reason, the temperature variations detected by the FBGs network placed on the interface LiPB1-LiPB2 as function of the time and pack voltage were selected and are shown in Figures VI.4 and VI.5. The intentional short circuit described before and presented in Fig. VI.4 a), at around 120 min, translated into an instantaneous decrease of temperature, as expected. The temperature increased once again once the circuit was reestablished, following the same behavior as in the second cycle.

During all cycling tests, showed in both Figures VI.4 a) and VI.5 a), the sensors responses were very coherent with the voltage signals. The temperature fluctuations detected by the FBG sensors corresponded to the normal heating flux produced by the LiPB pack. Over the four CC charge steps (1), maximum temperature variations (ΔT) of (4.0 ± 0.1) °C were sensed by the FBG sensors placed on the positions (1.1) and (1.2). During the CC discharge steps (2) and (3), higher ΔT values of (6.8 ± 0.1) °C (highlighted on Fig. VI.4 b)) and (14.0 ± 0.1) °C (highlighted on Fig. VI.5 b)) were respectively registered, at the end of each step.

Over the CC discharge steps (2) and (3), a gradual temperature increase can be observed, while the LiPBs pack discharges up to 9.0 V. However, three different temperature increasing rates can be precisely tracked. The first one, immediately after the beginning of discharge, the second, between the 11.0 V and 10.5 V, and the last one between the 10.5 V and 9.0 V. The first one is the higher and faster and it is proportional to the discharge rate applied. The second one is only registered under the discharge rate of 0.7 C, due to the higher jump in voltage to 10.3 V, when the CC discharge step begins.

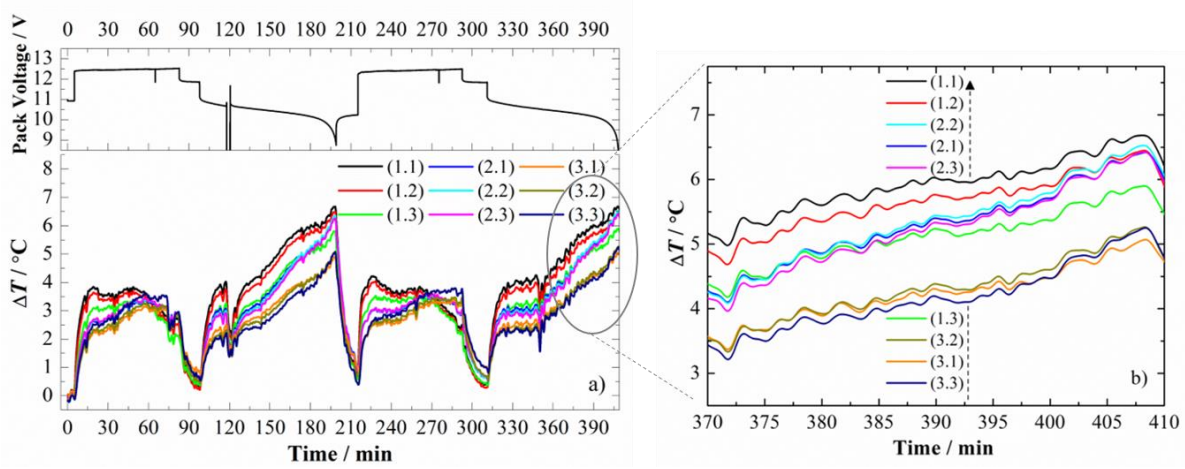

Figure VI.4. a) Temperature variations, during two cycling tests, in all the LiPB surface positions as a function of the pack voltage at 0.7 C discharge rate. b) Enlarged image representing the temperature variations recorded by the 9 FBG sensors inscribed in the fiber 2 during the CC discharge step at 0.7 C.

On the thermal behavior detected by the sensors located at the LiPB1-LiPB2 interface, during a CC discharge step at 0.7 C, and highlighted in Fig. VI.4 b), there is a clear

continuous heat generation up to the end of the discharge (EOD) process, in all areas of the surface. However, there are different temperature variations, depending on the sensor location. For example, the FBG placed in the position (1.3), at ~370 min presented the 3rd highest temperature variation, but as the temperature did not increase at the same rate as in other sensors, at ~383 min that location became the 6th hottest area.

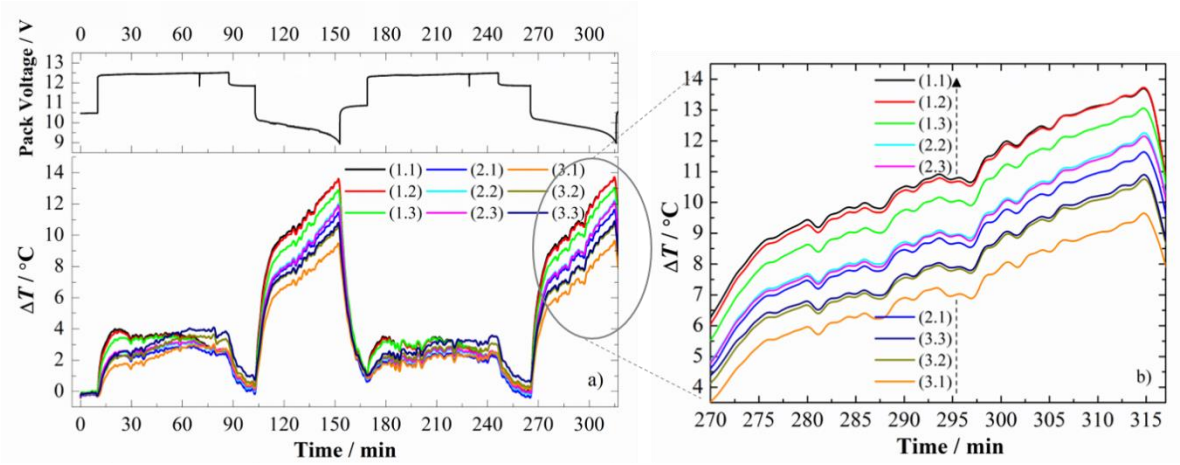

Figure VI.5. a) Temperature variations with time, during two cycling tests, in all the LiPB surface positions as a function of the pack voltage at 1.4 C discharge rate. b) Enlarged image representing the temperature variations recorded by the 9 FBG sensors located at interface LiPB1-LiPB2, during the higher discharge rate.

A continuous increase of heat generation can be observed in all areas during discharge rate at 1.4 C (see Fig. VI.5 b)), and there were not detected any changes in terms of gradient of temperature between the beginning and finishing of the process in all FBGs areas. Thus, the locations (1.1) and (1.2) were the hottest spots both when the discharge started and ended. The coldest zone was monitored by the FBG sensor on the location (3.1). In EOD, at ~315 min, a significant difference of temperature variation between the hot and cold areas of (4.3 ± 0.1) °C can be observed.

3.2 Spatial and temporal thermal mapping

3.2.1 CC charge at 1.0 C

The spatial and temporal thermal mapping of the four interfaces can be inferred through the FBG sensors responses just instants after the beginning (first instantaneous increase of

temperature) and the end of each CC charge step, at 1.0 C, as it is shown in Fig. VI.6. In this figure, each set of data represents the mean ΔT values between the four equal CC charge steps that the LiPBs pack was submitted to. Analyzing the temperature distribution produced in the beginning of charge (BOC), the same thermal profiles are observed in all the interfaces, with heating zones at the top of the LiPBs that compose the pack identified by the FBGs located on (1.1), (1.2), and (1.3), and cold areas predominantly in the bottom positions, corresponding to the (3.1), (3.2), and (3.3) zones.

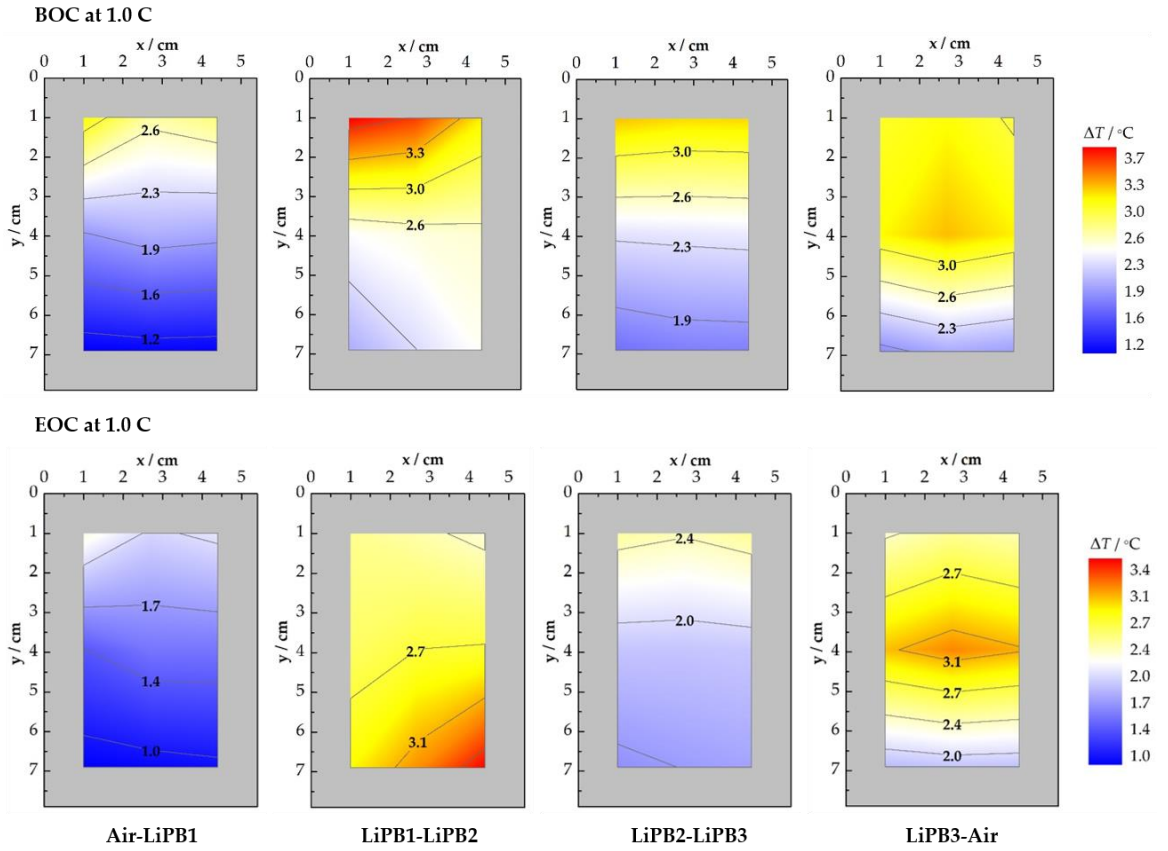

Figure VI.6. Spatial and temporal thermal mapping of the LiPBs pack when the CC charge at 1.0 C begins and ends.

Between all the interfaces monitored, the interface air-LiPB1 (monitored by fiber 1), can be considered the coldest. On the other hand, the hottest interface was the one sandwiched between the LiPB1 and LiPB2 (monitored by fiber 2). The warmest area was detected in this surface by the FBG in the position (1.1), with ΔT values of (3.7 ± 0.1) °C. At the center of

the interface between the LiPB3 and the air, a heating zone with ΔT values of (3.3 ± 0.1) °C was identified. This possibly happened due the higher proximity with the positive electrode existing in this surface.

In the end of charge (EOC) a different thermal profile can be observed, mainly at the interface LiPB1-LiPB2, in which the heating zone was detected by the FBG placed in position (3.3), with ΔT values of (3.4 ± 0.1) °C, and the coldest in the top position (1.3). Notice that the scale is slightly different in relation to the scale used in the BOC. The surface monitored by the sensors in the fiber 1 (Air-LiPB1 interface) remains the coldest. An interesting thermal profile was identified in the interface LiPB3-air, with a clear warmer central area and a decreasing of ΔT from that area until the battery extremities. The interface LiPB2-LiPB3 shows to be the more stable thermally all over the surface.

3.2.2 CC discharge at 0.7 C

The temporal and spatial thermal mapping of the interfaces presented in the LiPB pack in the beginning of discharge (BOD) and EOD instants, at 0.7 C, can be seen in Fig. VI.7. As in BOC process, the thermal profiles are gradual from the bottom (colder areas) to the top (hotter areas). However, at the interface LiPB3-air, a different behavior was observed. In this case, the hottest area was located in the middle of the LiPB3 surface. The hottest spots, with ΔT of (3.8 ± 0.1) °C and (3.5 ± 0.1) °C, were detected by the FBGs (1.1) and (2.2), located near the positive tab collector and in the center of the active area, in the interfaces LiPB1-LiPB2 and LiPB3-air, respectively. This observation can be correlated with the higher activation and current density of the Li^+ near both tabs, negative and positive, and the fact that the material of the positive tab (e.g. aluminum) is more conducive on heat generation than the negative tab material (e.g. nickel), due the different electrical resistance of the two materials.

At the EOD, the coldest zones are well evidenced on the bottom of the cells, being more pronounced in the interface air-LiPB1. The hottest spots, with ΔT of (6.8 ± 0.1) °C, was measured near the positive tab collector by the FBG located in (1.1), interface LiPB1-LiPB2, as well as in the areas (1.2), (2.1), (2.2), and (2.3) with ΔT of (6.4 ± 0.1) °C, all of them in the center of the active area of the cell, translating into the warmest interface in the LiPB pack. The FBGs inscribed in the fibers 3 and 4 also registered higher temperature changes

near to both tab current collectors, i.e. in the areas (1.1) and (1.3). Notice that, in Fig. VI.7, different scales were used for the EOD and BOD thermal maps, so, a thermal color comparison between the two cannot be performed in this case.

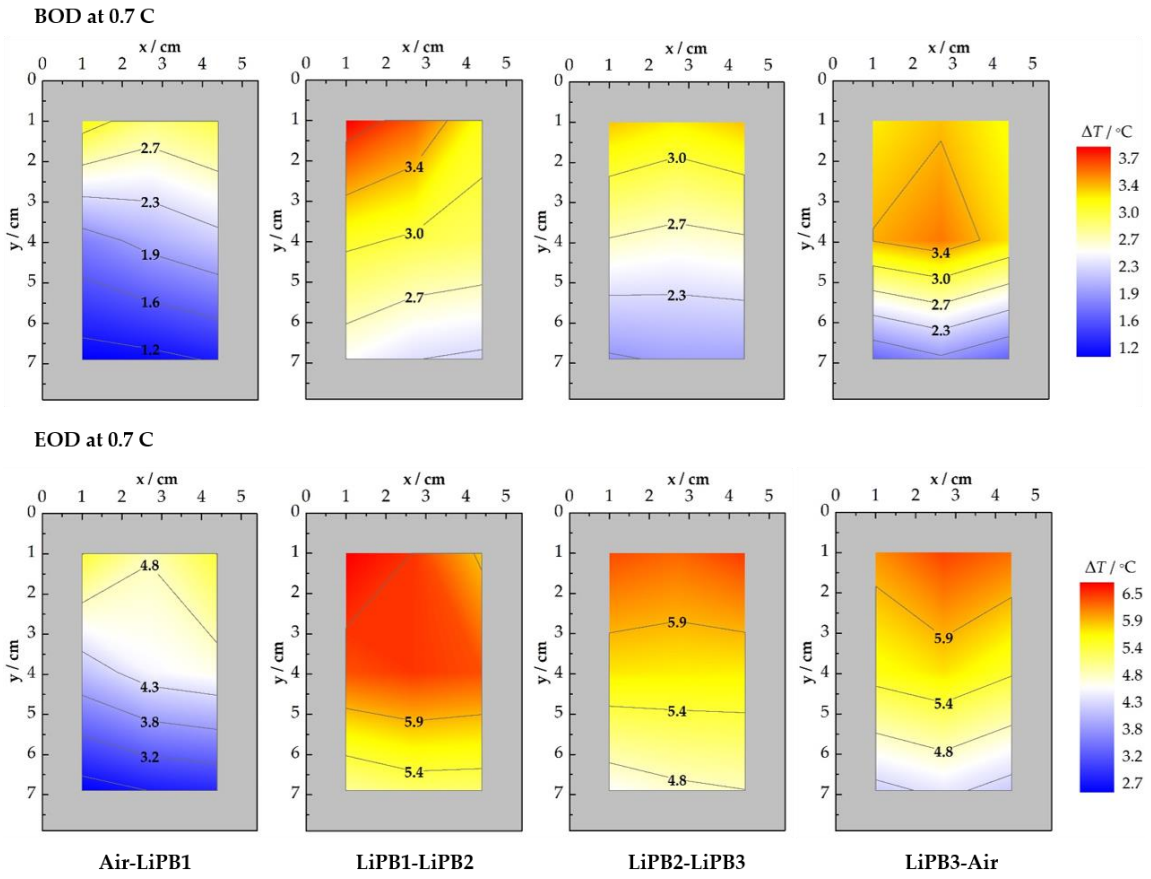

Figure VI.7. Spatial and temporal thermal mapping of the LiPB pack at the BOD and EOD instants, for the CC discharge at 0.7 C.

3.2.3 CC discharge at 1.4 C

Figure VI.8 shows the temperature variation detected by all the FBGs at the BOD and EOD, at the higher discharge rate of 1.4 C, in all the interfaces that compose the LiPBs pack. Due to the large temperature range on the BOD and EOD, the scales were also chosen independently to show the distribution with high resolution.

In general, and following the trend noticed in Fig. VI.7, the hottest zones were located at both collector tabs, on the positions (1.1), (1.2), and (1.3), and the coldest zones were located

at the bottom of the LiPBs, on the positions (3.1), (3.2), and (3.3). The temperature distribution gradient followed the line from the top to the bottom. These thermal profiles are in accordance with literature, however the batteries dimensions reported are not the same, and they were tested separately, instead of in a pack of batteries [3,19,27].

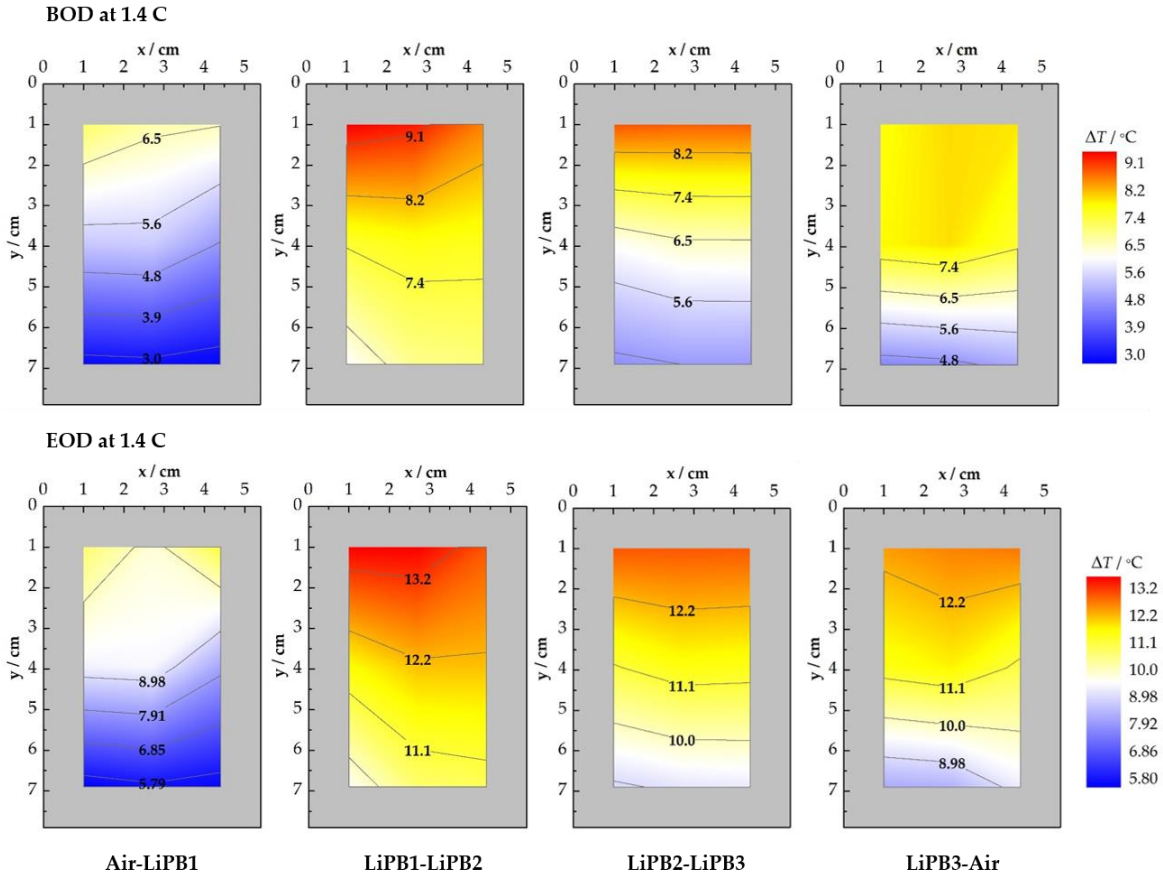

Figure VI.8. Spatial and temporal thermal mapping of the LiPBs pack when the CC discharge at 1.4 C begins and ends.

On the BOD, the main hottest spot, with a ΔT of (9.4 ± 0.1) °C, was detected by the FBG located at the interface LiPB2-LiPB2, at the area (1.1). From all the pack interfaces, the warmest was between the LiPB1 and LiPB2. The coldest interface was between the air-LiPB1, registering the lowest cold zones value of in all batteries pack of (2.8 ± 0.1) °C on the (3.1), (3.2) and (3.3) areas. The thermal profiles at the EOD follow the same behavior as at the BOD, however, the temperature variations were higher. The hottest spot, with ΔT of (14.0 ± 0.1) °C was clearly registered by the sensor written in the fiber 2 and located in the

position (1.1). The results indicate that this area is the likely to be the hot spot zone in all the LiPBs pack, being the most critical region in terms of safety. This occurred due to the higher current density of the Li^+ in the positive tab collector. A plausible reason for the fact that this occurred in the interface between LiPB1-LiB2 can be attributed to the higher performance registered by the LiPB2, as can be seen in Fig. VI.3.

Comparing the temperature distribution in all the interfaces showed in Fig. VI.8, it can be observed that the ΔT mean value between all interfaces is (4.0 ± 0.1 °C), revealing a low thermal discrepancy between them. However, the physical spacing between thermal boundaries is different at all interfaces, highlighting their specific thermal profiles.

4. Conclusions

A sensing network of 37 FBGs was successfully used to monitor and to implement a temporal and spatial thermal mapping of four interfaces in a pack of 3 prismatic LiPBs. The batteries were connected in series and a cycling protocol was established with normal CC charge (1.0 C) and two different CC discharge steps (0.7 C and 1.4 C). In total, the thermal profiles in the BOC, BOD, EOC, and EOD steps were analyzed. On the BOC, a maximum temperature variation of (3.7 ± 0.1) °C was measured near the positive tab in the interface LiPB1-LiPB2. A heating zone of (3.3 ± 0.1) °C was also identified in the center of the surface between the LiPB3 and the air.

In general, over the discharge steps the hotter zones were located at the both collector tabs, and the cold zones were at the bottom of the LiPBs. For the higher discharge rate, the thermal profiles at the EOD were very similar with the ones identified at the BOD. At the EOD, a hot spot, with ΔT of (14.0 ± 0.1) °C was registered by the sensor located near the positive tab collector, at the interface LiPB1-LiPB2. This occurs due to the higher current density of the Li^+ in that region. This sensing technique also allows more points to be monitored. For that, more FBG sensors with different Bragg wavelengths can be recorded in the same optical fiber or can be used different fiber sensing configurations without increasing the invasiveness of the battery pack interfaces.

The presented FBG sensing network shows to be a good, precise, non-invasive and low-cost tool to improve thermal management and safety of batteries, identifying critical zones for the appearance of hot spots.

Funding: This research was funded by Project POCI 01-0145-FEDER-016414, cofinanced by POCI and PORL, through FEDER funds and by National Funds through FCT – Fundação para a Ciência e Tecnologia, Grant numbers BI/UI96/6642/2018, PD/BD/128265/2016 (DAEPHYS) and SFRH/BPD/124549/2016 and by FEDER funds through the COMPETE 2020 Programme and National Funds through the project UID/CTM/20025/2013.

Author Contributions: All authors contributed equally. Micael Nascimento, Tiago Paixão and Marta S. Ferreira conceived the experiments and analyzed the data. All authors discussed the results, wrote and revised the paper.

Conflicts of Interest: The authors declare no conflicts of interest.

References

[1] Zhang, Z.; Ramadass, P.; Fang, W. Safety of lithium-ion batteries. In Lithium-ion batteries: Advances and applications. Pistoia G. 1st Ed.; Publisher: Elsevier Amsterdam, Netherlands, 2014; Volume 18, pp. 409-435, ISBN: 978-0-444-59513-3.

[2] Spotnitz, R.; Franklin, J. Abuse behavior of high-power, lithium-ion cells. J Power Sources 2003, 113, 81-100, DOI: 10.1016/S0378-7753(02)00488-3.

[3] Panchal, S.; Dincer, I.; Agelin-Chaab, M.; Fraser, R.; Fowler, M. Experimental temperature distributions in a prismatic lithium-ion battery at varying conditions. Int. Commun. Heat Mass Transfer 2016, 71, 35-43, DOI: 10.1016/j.icheatmasstransfer.2015.12.004.

[4] Xing Y.; Miao Q.; Tsui K.-L.; Pecht M. Prognostics and Health Monitoring for Lithium-ion Battery. IEEE International Conference on, 2011, DOI: 10.1109/ISI.2011.5984090.

[5] Feng X.; Fang M.; He X.; Ouyang M.; Lu L.; Wang H.; Zhang M. Thermal runaway features of large format prismatic lithium ion battery using extended volume accelerating rate calorimetry. J Power Sources 2014, 255, 294-301, DOI: 10.1016/j.jpowsour.2014.01.005.

[6] Koch, S.; Birke, K.P.; Kuhn, R. Fast thermal runaway detection for lithium-ion cells in large scale traction batteries. Batteries, 2018, 4, 16, DOI: 10.3390/batteries4020016.

[7] Lei, B.; Zhao, W.; Ziebert, C.; Uhlmann, N.; Rohde, M.; Seifert, H.J. Experimental analysis of thermal runaway in 18650 cylindrical Li-ion cells using an accelerating rate calorimeter. Batteries 2017, 3, 14, DOI: 10.3390/batteries3020014.

[8] Loveridge, M.J.; Remy, G.; Kourra, N.; Genieser, R.; Barai, A.; Lain, M.J.; Guo, Y.; Amor-Segan, M.; Williams, M.A.; Amietszajew, T.; Mark, E.; Bhagat, R.; Greenwood, D. Looking Deeper into the Galaxy (Note 7). Batteries 2018, 4, 3, DOI: 10.3390/batteries4010003.

[9] Bella, F.; Colò, F.; Nair, J.R.; Gerbaldi, C. Photopolymer Electrolytes for Sustainable, Upscalable, Safe, and Ambient-Temperature Sodium-Ion Secondary Batteries. ChemSusChem 2015, 8, 3668-3676, DOI: 10.1002/cssc.201500873.

[10] Radzir, N.N.M.; Hanifah, S.; Ahmad, A.; Hassan, N.H.; Bella, F. Effect of lithium bis(trifluoromethylsulfonyl)imide salt-doped UV-cured glycidyl methacrylate. Solid State Electrochem. 2015, 19, 3079-3085, DOI: 10.1007/s10008-015-2910-z.

[11] Suriyakumara, S.; Gopi, S.; Kathiresan, M.; Bose, S.; Gowd, E.B.; Nair, J.R.; Angulakshmi, N.; Meligrana, G.; Bella, F.; Gerbaldi, C.; Stephan, A. M. Metal organic framework laden poly(ethylene oxide) based composite electrolytes for all-solid-state Li-S and Li-metal polymer batteries. Electrochem. Acta 2018, 285, 355-364, DOI: 10.1016/j.electacta.2018.08.012.

[12] Li, X.; Wang, Z.; Lin, H.; Liu, Y.; Min, Y.; Pan, F. Composite electrolytes of pyrrolidone-derivatives-PEO enable to enhance performance of all solid-state lithium-ion batteries. Electrochem. Acta 2019, 293, 25-29, DOI: 10.1016/j.electacta.2018.10.023.

[13] Mankowski, P.J.; Kanevski, J.; Bakirtzian, P.; Cugno, S. Cellular phone collateral damage: A review of burns associated with lithium battery powered mobile devices. Burns 2016, 42, e61-e64, DOI: 10.1016/j.burns.2015.10.012.

[14] Duh Y-S.; Lin K.H.; Kao C-S. Experimental investigation and visualization on thermal runaway of hard prismatic lithium-ion batteries used in smart phones. J Therm Anal Calorim. 2018, 132, 1677-1692, DOI: 10.1007/s10973-018-7077-2.

[15] Panchal, S.; Dincer, I.; Agelin-Chaab, M.; Fraser, R.; Fowler M. Thermal modeling and validation of temperature distributions in a prismatic lithium-ion battery at different discharge rates and varying boundary conditions. Appl. Therm. Eng. 2015, 96, 190-199, DOI: 10.1016/j.applthermaleng.2015.11.019.

[16] Panchal, S.; Dincer, I.; Agelin-Chaab, M.; Fraser, R.; Fowler M. Experimental and theoretical investigation of temperature distributions in a prismatic lithium-ion battery. Int. J. Therm. Sci. 2015, 99, 204-2015, DOI: 10.1016/j.ijthermalsci.2015.08.016.

[17] Mutyala, M.S.K.; Zhao, J.; Li, J.; Pan, H.; Yuan, C.; Li, X. In situ temperature measurement in lithium-ion battery by flexible thin film thermocouples. J Power Sources 2014, 260, 43-49, DOI: 10.1016/j.jpowsour.2014.03.004.

[18] Fu, Y.; Lu, S.; Li, K.; Liu, C.; Cheng, X.; Zhang, H. An experimental study on burning behaviors of 18650 lithium ion batteries using a cone calorimeter. J Power Sources 2015, 273, 216-222, DOI: 10.1016/j.jpowsour.2014.09.039.

[19] Li Z.; Zhang J.; Wu B.; Huang J.; Nie Z.; Sun Y.; An F.; Wu N. Examining temporal and spatial variations of internal temperature in large-format laminated battery with embedded thermocouples. J Power Sources 2013, 241, 536-553, DOI: 10.1016/j.jpowsour.2013.04.117.

[20] Ji Y.; Wang C. Y. Heating strategies for Li-ion batteries operated from subzero temperatures. Electrochem. Acta 2013, 107, 664-674, DOI: 10.1016/j.electacta.2013.03.147.

[21] Tippmann S.; Wapler D.; Balboa L.; Spier B.; Bessler W. G. Low temperature charging of lithium-ion cells part I: Eletrochemical modeling and experimental investigation of degradation behavior. J Power Sources 2014, 252, 305-316, DOI: 10.1016/j.jpowsour.2013.12.022.

[22] Yildiz M.; Karakoc H.; Dincer I. Modelling and validation of temperature changes in pouch lithium-ion battery at various discharge rates. Int. Commun. Heat Mass Transfer 2016, 75, 311-314, DOI: 10.1016/j.icheatmasstransfer.2016.03.009.

[23] Panchal, S.; Dincer, I.; Agelin-Chaab, M.; Fraser, R.; Fowler M. Uneven temperature and voltage distributions due to rapid discharge rates and different boundary conditions for series-connected LiFePO4 batteries. Int. Commun. Heat Mass Transfer 2017, 81, 210-217, DOI: 10.1016/j.icheatmasstransfer.2016.12.026.

[24] Mathew, M.; Mastali, M.; Catton, J.; Samadani, E.; Janhunen, S.; Fowler, M. Development of an electro-thermal model for electric vehicles using a design of experiments approach. Batteries 2018, 4, 29, DOI: 10.3390/batteries4020029.

[25] Lee C-Y.; Weng F-B.; Huang Y-P.; Chang C-P.; Cheng C-K. Real time monitoring of internal temperature and voltage of high-temperature fuel cell stack. Electrochim. Acta 2015, 161, 413-419, DOI: 10.1016/j.electacta.2015.02.135.

[26] Yi J.; Kim U. S.; Chee S.; Han T.; Park S. Modelling the temperature dependence of the discharge behavior of a lithium-ion battery in low environmental temperature. J Power Sources 2013, 244, 143-148, DOI: 10.1016/j.jpowsour.2013.02.085.

[27] Kim U. S.; Yi J.; Chee S.; Han T.; Park S. Modelling the thermal bahaviour of a lithium-ion battery during charge. J Power Sources 2011, 196, 5115-5121, DOI: 10.1016/j.jpowsour.2011.01.103.

[28] Wang P.; Zhang X.; Yang L.; Zhang X.; Yang M.; Chen H.; Fang D. Real-time monitoring of internal temperature evolution of Li-ion coin cell battery during the charge and discharge process. Extreme Mech. Lett. 2016, 9, 459-466, DOI: 10.1016/j.eml.2016.03.013.

[29] Lee C-Y.; Lee S-J.; Hung Y-M.; Hsieh C-T.; Chang Y-M.; Huang Y-T.; Lin J-T. Integrated microsensor for real-time microscopic monitoring of local temperature, voltage and current inside lithium ion battery. Sensor Actuat. A: Phys. 2017, 253, 59-68, DOI: 10.1016/j.sna.2016.10.011.

[30] Grattan, K.T.V.; Meggitt, B.T. Optical fiber sensor technology: Applications and Systems. Publisher: Kluwer Academic Publishers, London, 1999; Volume 3, pp. 357-363, ISBN: 978-1-4757-6077-4.

[31] Othonos, A.; Kalli, K. Fiber Bragg Gratings: Fundamentals and Applications in Telecommunications and Sensing. Publisher: Artech House: New York, NY, USA, 1999.

[32] Yang, G.; Leitão, C.; Lib, Y.; Pinto, J.L.; Jiang, X. Real-time temperature measurement with fiber Bragg sensors in lithium batteries for safety usage. Measurement 2013, 46, 3166-3172, DOI: 10.1016/j.measurement.2013.05.027.

[33] Sommer, L.W.; Kiesel, P.; Ganguli, A.; Lochbaum, A.; Saha, B.; Schwartz, J.; Bae, C-J.; Alamgir, M. Fast and slow ion diffusion processes in lithium-ion pouch cells during cycling observed with fiber optic strain sensors. J. Power Sources 2015, 296, 46-52, DOI: 10.1016/j.jpowsour.2015.07.025.

[34] Novais, S.; Nascimento, M.; Grande, L.; Domingues, M.F.; Antunes, P.; Alberto, A.; Leitão, C.; Oliveira, R.; Koch, S.; Kim, G.T.; Passerini, S.; Pinto, J.L. Internal and external temperature monitoring of a Li-ion battery with fiber Bragg grating sensors. Sensors 2016, 16, 1394, DOI: 10.3390/s16091394.

[35] Nascimento, M.; Ferreira, M.; Pinto, J.L. Real time thermal monitoring of lithium batteries with fiber sensors and thermocouples: A comparative study. Measurement 2017, 111, 260-263, DOI: 10.1016/j.measurement.2017.07.049.

[36] Gao H.; Li H.; Liu B.; Zhang H.; Lou J.; Cao Y.; Yuan S.; Zhang W.; Kai G.; Dong X. A novel fiber Bragg grating sensor multiplexing technique. Opt. Commun. 2005, 251, 361-366, DOI: 10.1016/j.optcom.2005.03.027.

[37] Mihailov, S.J. Fiber Bragg Grating Sensors for Harsh Environments. Sensors, 2012, 12, 1898-1918, DOI: 10.3390/s120201898.

[38] Gupta, S.; Mizunami, T.; Yamao, T.; Shimomura, T. Fiber Bragg grating cryogenic temperature sensors. Appl. Opt. 1996, 35, 5202-5205, DOI: 10.1364/AO.35.005202.

Chapter VII

Internal strain and temperature discrimination with optical fiber hybrid sensors in Li-ion batteries

Published in *Journal of Power Sources*, 2019, 410-411, 1-9

DOI: 10.1016/j.jpowsour.2018.10.096

Internal strain and temperature discrimination with optical fiber hybrid sensors in Li-ion batteries

Micael Nascimento, Susana Novais, Markus Ding, Marta S. Ferreira, Stephan Koch, Stefano Passerini, João L. Pinto

Abstract

Strain and temperature are critical parameters to monitor in Li-ion batteries (LIBs) to improve their safety and long-term cycling stability. High local current densities can result in a massive heat release, decomposition of the electrolyte, gas evolution and even explosion of the battery cell, known as thermal runaway. However, the corrosive chemical environment in the batteries is a challenge to monitor strain and temperature. Optical fiber sensors, due to their high chemical stability and small diameter, can be embedded within the LIBs, thus becoming an interesting solution for *operando* and *in situ* measurements. In this work, a hybrid sensing network constituted by fiber Bragg gratings and Fabry-Perot cavities is proposed for the discrimination of strain and temperature. The proof-of-concept was performed by attaching the sensing network to the surface of a smartphone battery. Afterwards, it was embedded in a Li-ion pouch cell to monitor and simultaneously discriminate internal strain and temperature variations in three different locations. Higher thermal and strain variations are observed in the middle position. The methodology presented proves to be a feasible and non-invasive solution for internal, real-time, multipoint and *operando* temperature and strain monitoring of LIBs, which is crucial for their safety.

Keywords: Li-ion batteries; embedded sensors; Fabry-Perot interferometer; fiber Bragg gratings; strain; temperature.

1. Introduction

Lithium-ion batteries (LIBs) are extensively used in portable electronic devices such as smartphones and laptops, and automotive/aerospace industries, which have driven the battery development regarding new materials, structures, and designs, due to their optimized conditions in the perspective of power, energy, long cycle-life, and slow self-discharge [1-3].

As in other electrochemical energy storage systems, the chemistry of the active materials alters during the charge/discharge processes, promoting strains in electrode particles and changes in electrode volume. This volume variation is caused by Li^+ intercalation into host materials, like graphite and lithium transition metal oxide and resultant lattice expansion and contraction [4, 5]. The LIB stability and safety can be affected by these induced strains, being the principal cause of material failure and other forms of performance degradation [1].

Another crucial phenomenon that can affect the LIB safety is the thermal runaway, caused by the fast-increasing temperature that can be formed in specific operating conditions [6, 7]. The excess heat generated during over-charge/discharge or in the presence of short circuits may cause irreversible damage particularly to the electrolyte resulting in its decomposition, gas evolution and even explosion of the battery cell [7,8].

The optimized design of a LIB management system needs firstly to solve questions in terms of inherent safety under both normal and abuse operating conditions, being correlated with strain and temperature monitoring. The ability to quantify and evaluate the variation in strain and heat generated during the electrochemical processes that the batteries can operate will be crucial information regarding their behavior as well as an active tool to promote their safety. To achieve this goal, knowledge of the internal strain and temperature sensing is therefore critical [1,6].

Due to the more specific electrochemical behaviors and internal structure of the LIBs, their internal sensing is challenging. To work around this problem, sensors with mechanical robustness, immunity to electromagnetic radiation, resistance to corrosion and low invasiveness, are required. The temperature and strain sensing of LIB is typically performed using pyrometers [9], electro-mechanical sensors [4], 3D digital image correlation [8], thermocouples [10-11], and high energy X-ray diffraction technique [12]. On the other hand, due to the advantages of ease in multiplexing, fast response and immunity to electromagnetic interference when compared to electronic sensors [13], recent works showed that optical fiber sensors are a suitable solution to perform internal and external temperature and strain measurements in LIBs [14-19].

Fiber Bragg gratings (FBGs) are used in sensing temperature, strain, pressure, bending, refractive index, among other physical parameters. However, as these sensors are sensitive

to more than one physical parameter at the same time, they suffer from large cross sensitivity, such as strain and temperature.

Many techniques have been proposed to simultaneously discriminate strain and temperature. The most straightforward way is using two different FBGs: one strain-free FBG and another that simultaneously detects strain and temperature [15]. However, this method can be challenging when the sensors are embedded in electrochemical materials, due to the necessity of involving the strain-free FBG sensors in other material [20]. Typically, conductive microtubes are used, at the cost of increasing the invasiveness and the possibility of interacting with the electrochemical materials [20].

Other methods are based on the use of different sensing elements that have different responses to strain and temperature. For example, methods have been reported that use an FBG pair [21], chirped FBG [22], or cascading an FBG with a thermochromic material coated fiber tip [23]. All these methods have good response to strain and temperature, however they are inappropriate for precise measurements due to low spatial resolution. FBGs were also recorded in high birefringence [24] or doped [25] fibers, however they require a fiber laser system for demodulation. Combined Fabry-Perot (FP) and FBG sensors were studied; however, the production is complex and photosensitive fiber is needed [26]. Furthermore, the FP cavity was produced using a capillary tube with a length of ~420 μm [27].

Recent studies show the wide use and utility of this type of sensors to monitor physical parameters of LIBs, both internally and externally. FBG sensors were extensively used to discriminate simultaneously external bi-directional strain and temperature in a prismatic LiB, using an independent strain-free FBG [15]. On the other hand, FBGs were also utilized to determine fast and slow ion diffusion processes in Li-ion pouch cells [16], to monitor internal and external temperature variations in lithium-ion pouch bag cells [17], and to monitor the strain evolution of LIB electrodes [19]. FP sensors based on air cavities are typically used to monitor strain or pressure variations [28, 29] due to the fact that they are almost insensitive to temperature shifts [28].

However, when this type of sensors is integrated inside materials, their sensitivity to temperature and strain changes due to the mechanical stresses produced by the surrounding material, and an internal calibration is required [31,32].

Internal discrimination of strain and temperature in LIB can be improved by combining the signals of FBGs and FPs, by writing the FBG sensor as near as possible to the FP cavity. The main advantages of this process are the different strain and temperature sensitivities obtained by the FP cavities comparatively with the FBGs, together with the necessity of using a single fiber to monitor the same point, decreasing the invasiveness inside the battery. Besides, no extra-material is needed to be integrated in the discrimination method.

In this study, a hybrid sensing network of FBGs and FPs was preliminary tested on the surface of a smartphone battery to discriminate external strain and temperature variations. The sensing network was also embedded in a LIB to monitor and discriminate *operando* and *in situ* internal strain and temperature shifts. Galvanostatic cycling at different C-rates was applied to correlate the variations in temperature and strain with processes in the LIB. To the best of our knowledge, this is the first time that this innovative methodology is presented for this type of application.

2. Materials and methods

2.1 Theoretical considerations: FBG and FP sensors

Typically, an FBG sensor consists of a short segment of a single-mode optical fiber (with a length of a few millimeters) with a photoinduced periodically modulated index of refraction in the core of the fiber. The FBG resonant wavelength is related to the effective refractive index of the core mode (n_{eff}) and to the grating period (Λ). When the grating is illuminated with a broadband optical source, the reflected power spectrum presents a sharp peak, which is caused by interference of light with the axis of the grating and can be described through Equation (1) [13],

$$\lambda_B = 2n_{eff}\Lambda\,, \tag{1}$$

where λ_B is the so-called Bragg wavelength. When the fiber is exposed to external variations of a given measurand (such as strain, temperature, stress or pressure, among others), both n_{eff} and Λ can be modified, causing a shift in the Bragg wavelength.

A FP sensor is designed of two parallel reflecting surfaces separated by a certain length (L). Interference arises due to the multiple super positions of both reflected and transmitted beams at two parallel surfaces. In an optical fiber, the FP can be formed by intentionally

building up reflectors inside (intrinsic) or outside (extrinsic) the fibers. The intrinsic FP fiber sensors have reflecting components within the fiber itself. The intrinsic FP cavity can be designed by different methods such as micro machining [29], chemical etching [33], and thin film deposition [34]. The wavelength dependent intensity modulation of the input light spectrum, that occurs due to the optical phase difference (δ_{FP}) between two reflected or transmitted beams describes the reflection or transmission spectrum of an FP. This phase difference of the FP can be tailored according to Equation (2).

$$\delta_{FP} = \frac{4\pi nL}{\lambda}, \tag{2}$$

where, λ, *L* and *n* are the wavelength of the incident light, the length and the refractive index of the cavity, respectively. It is important to note that the phase difference is changed with the variation in the optical path length difference of the interferometer, when some perturbation is presented to the sensor. For example, a phase variation occurs when longitudinal strain is applied to the FP sensor due to a change in the length of the cavity or a change in surrounding refractive index. It is possible to quantitatively obtain the strain applied, by measuring the wavelength shift of a FP spectrum [35].

2.2 Strain and temperature discrimination using a hybrid sensor

As aforementioned, with a single measurement of the Bragg wavelength-shift it is not possible to discriminate the effect of changes in strain and temperature. The strain and temperature discrimination can be performed using a combination of the wavelengths of FBG with a FP cavity sensor, forming a hybrid sensor. The methodology presented is based on writing the FBG sensor as close as possible to the FP cavity sensor, which simultaneously detects strain and temperature. If the wavelength-shifts to strain and temperature are linear, a response to a strain shift, $\Delta\varepsilon$ and a temperature shift, ΔT, is given by:

$$\Delta\lambda_{FBG} = k_{FBG_\varepsilon}\Delta\varepsilon + k_{FBG_T}\Delta T, \tag{3}$$

where $k_{FBG\varepsilon}$, and k_{FBGT} are the strain and temperature sensitivities of the FBG, respectively, determined in the calibration procedure. The FP cavity of the hybrid sensor also acts as a strain and temperature sensor. In this case, the wavelength shift, $\Delta\lambda_{FP}$, is related to strain variation, $\Delta\varepsilon$, and temperature variation, ΔT, according to:

$$\Delta\lambda_{FP} = k_{FP_\varepsilon}\Delta\varepsilon + k_{FP_T}\Delta T, \quad (4)$$

where $k_{FP\varepsilon}$ and k_{FPT} are the strain and temperature sensitivities of the FP cavity, respectively. Therefore, the temperature and strain variations can be determined through the matrixial method, using Equation (3) and (4), expressed as:

$$\begin{bmatrix}\Delta\lambda_{FBG}\\ \Delta\lambda_{FP}\end{bmatrix} = \begin{bmatrix}k_{FBG_\varepsilon} & k_{FBG_T}\\ k_{FP_\varepsilon} & k_{FP_T}\end{bmatrix}\begin{bmatrix}\Delta\varepsilon\\ \Delta T\end{bmatrix}. \quad (5)$$

If these sensitivities are known, a sensitivity matrix for simultaneous measurement of strain and temperature can be derived as:

$$\begin{bmatrix}\Delta\varepsilon\\ \Delta T\end{bmatrix} = \frac{1}{M}\begin{bmatrix}-k_{FP_T} & k_{FBG_T}\\ k_{FP_\varepsilon} & -k_{FBG_\varepsilon}\end{bmatrix}\begin{bmatrix}\Delta\lambda_{FBG}\\ \Delta\lambda_{FP}\end{bmatrix}, \quad (6)$$

where M = $k_{FP\varepsilon}$ k_{FBGT} - k_{FPT} $k_{FBG\varepsilon}$ is determinant of the coefficient matrix, which must be non-zero for possible simultaneous measurement [36].

2.3 Sensor design

The proposed sensing structure constituted by an FBG in series with a FP cavity is shown in Fig. VII.1 a. The FP cavity was fabricated by producing an air bubble between a single mode fiber (SMF, 28e, Thorlabs Inc., Newton, USA) and a multimode fiber (MMF, GIF625, Thorlabs Inc., Newton, USA). Initially the two fibers were placed in the splicing machine (Fujikura 62S, Tokyo, Japan) and aligned using the manual mode. The SMF was removed and an arc discharge was applied to the MMF tip. The electrical discharge high power was transferred to the MMF tip, causing a partial melting. Because of the surface tension, the fiber acquired a round shape. Afterwards, both fibers were aligned once again, and a small amount of compression was applied between them. After one arc, the energy transferred to the fiber tips will cause their melting and, as the temperature in the fibers outer region decreases faster than on the inside, some air is trapped, forming a microbubble [37] (Fig. VII.1 b). Typically, the length of such cavities is lower than 100 µm, giving rise to a high free spectral range.

The FBGs used in the monitoring system, with estimated length of ~3.0 mm, were written by the phase mask method. A pulsed Q-switched Nd:YAG laser system (LOTIS TII LS-2137U Laser, Minsk, Belarus) lasing at the fourth harmonic (266 nm), focusing the beam in

the SMF with a plano-convex cylindrical lens (working length of 320 mm), was used. The single pulse used to produce the FBGs was 8.0 ns duration with measured pulse energy of 0.9 mJ. The FBGs were written as close to the FP cavity as possible, to allow nearly punctual detection of strain and temperature. Furthermore, as the SMF used was photosensitive, the FBGs were written in that region.

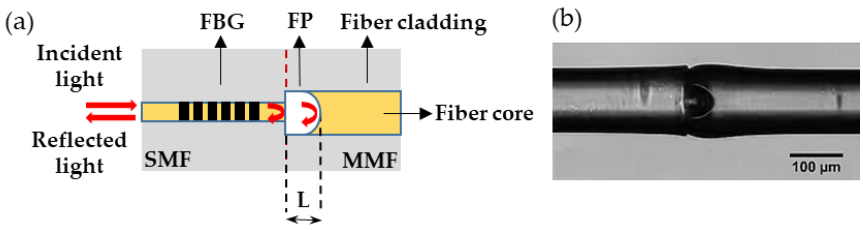

Figure VII.1. a) Experimental diagram of the hybrid sensor. b) Microscope image of the FP cavity formed between the SMF + MMF.

2.4 Experimental setup

2.4.1 External monitoring of strain and temperature

The battery used in the proof-of-concept experiment was a commercial hard prismatic rechargeable smartphone LIB (iPhone 5G Battery, Singapore) with an open-circuit voltage of 4.3 V, nominal capacity of 1440 mAh, cut-off voltage of 3.2 V, and dimensions of 8.6 cm (length) × 3.0 cm (width) × 0.3 cm (thickness). The internal structure of this battery is constructed by winding the ribbon-like electrode and separator to form a 'jelly-roll' structure. The negative and positive active materials, carbon/graphite and pure cobalt, respectively, are coated on each side of the separator materials, and thin layers of copper and aluminum foils are used as the current collectors [6].

The fiber with the hybrid sensor was pre-tensioned and fixed to the battery on its extremities, being placed in direct contact with the surface and in the center of the LIB, as is shown in Fig. VII.2. To calculate the length variations, the distance between the two fixed points (8.6 cm) was considered. As the glue was placed as close to the edge of the LIB as possible, the length variations are related to the battery dimension. This configuration allows the discrimination of strain and temperature in the same point, where both sensors detect strain and temperature shifts.

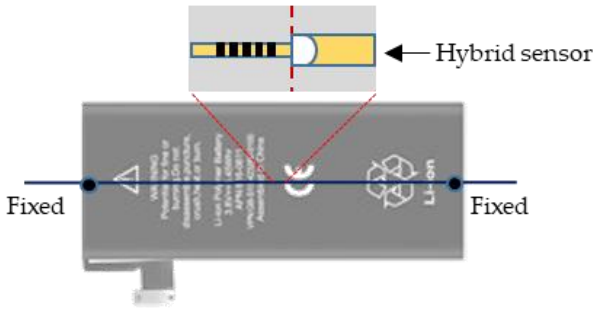

Figure VII.2. Hybrid sensor location to external temperature and strain discrimination of a commercial LIB.

The reflected spectra were measured with an optical interrogator (sm125-500, Micron Optics Inc., Atlanta, GA USA) operating at 2.0 Hz and wavelength accuracy of 1.0 pm. The commercial LIB was subjected to charge/discharge cycles under a discharge rate of 1.32 C, through a power resistor of 2.0 Ω until a voltage of 2.0 V was reached.

A charge rate of 0.70 C was applied, using a commercial battery charger with output voltage of 5.0 V (ETA0U83EWE, Samsung, Vietnam). Between the charge/discharge steps, a resting time of 10 min was selected to stabilize the battery. The voltage signal was monitored using a 12-bit resolution data acquisition system (DAQ) (USB6008, National Instruments, Austin, TX, USA), and controlled by a LabVIEW® customized application, allowing the real-time monitoring of the acquired data.

2.4.2 Li-ion pouch cell assembly

The pouch cell was assembled using a commercial lithium iron phosphate (LFP, Clariant, Muttenz, Switzerland) cathode (91:4:5 LFP: Super C65:JSR, 12 mg cm^{-2} active mass loading) on aluminum foil and a graphite anode (92:3:5 SBG-1:Super C65:CMC, supplied by SGL Carbon, 5.6 mg cm^{-2} active mass loading) on copper foil with an active area of 16 cm^2, following a procedure already described in literature [38]. The Li-ion pouch cell assembly was carried out inside the dry room (relative humidity < 0.1% at 20 °C), where all materials were stored prior to usage. Two sheets of a single layer polyolefin membrane (Hipore SV718, 10 µm, Asahi Kasei, Tokyo, Japan) were used as separator. 500 µL of a 1 M

lithium hexafluorophosphate ($LiPF_6$) in ethylene carbonate/dimethyl carbonate (1:1 vol%) with 1 wt% vinylene carbonate solution were used as electrolyte.

The sensors network was internally placed between the two separators layers, in the x-axis, on the top (near the tab-electrode connection), middle (center of the electrochemical active area), and bottom of the cell, to get a total gradient mapping of the strain and temperature in all cell area, as shown in Fig. VII.3.

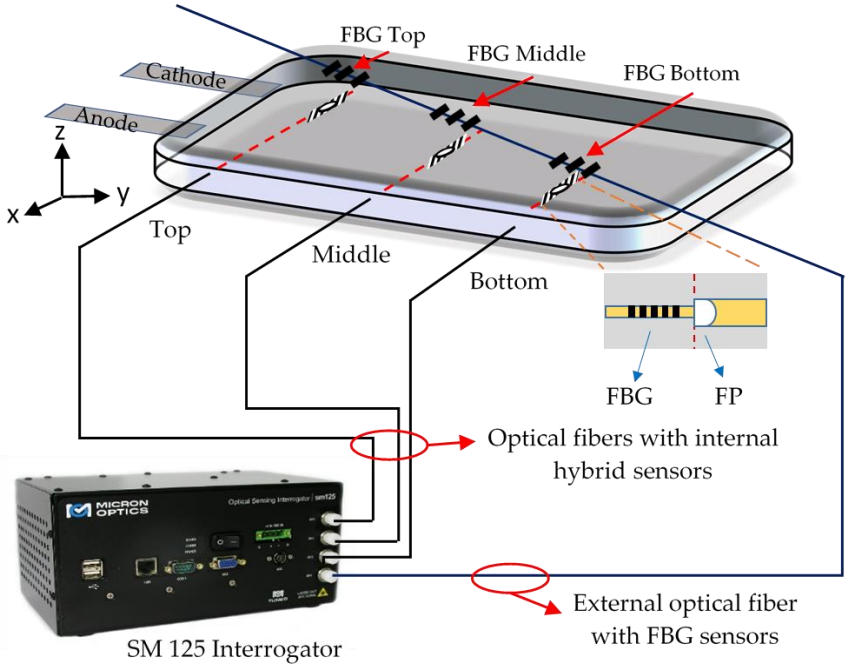

Figure VII.3. Experimental setup diagram of the internal and external optical sensors network used to temperature and strain monitoring of the Li-ion pouch cell.

The Li-ion pouch cell was heat-sealed under vacuum, and the fibers with the hybrid sensors were fixed to the pouch bag in the region of the seal. The distance between the fixed points was 6.0 cm. Externally, a network of 3 FBGs was placed in direct contact with the surface of the pouch cell, parallel to the above-mentioned internal ones. To increase both the contact area and the thermal conductivity, a thermal paste was used to attach the sensors to the pouch cells. The Li-ion cell was cycled several times at different discharge rates.

2.5 Sensors calibration

Prior to the fiber sensors attachment to the LIB, a calibration to strain and temperature was carried out. The strain characterization was performed using a micrometric translation stage between 0 με and 1200 με. The thermal calibrations after and before the integration in the Li-ion pouch cell were performed in a thermal chamber (Model 340, Challenge Angelantoni Industrie, Massa Martana, Italy), between 10.0 °C and 150.0 °C, in steps of 20.0 °C. Figures VII.4 a and VII.5 a show the spectral response of the hybrid sensor under the temperature and strain calibrations, respectively.

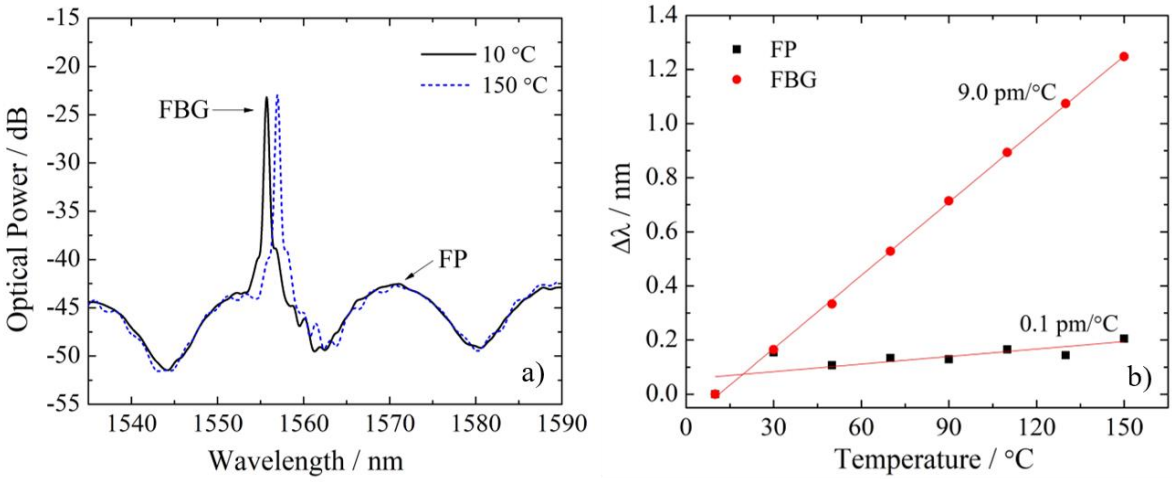

Figure VII.4. a) Spectral response of the hybrid sensor at two different temperatures and b) wavelength shift with the applied temperature.

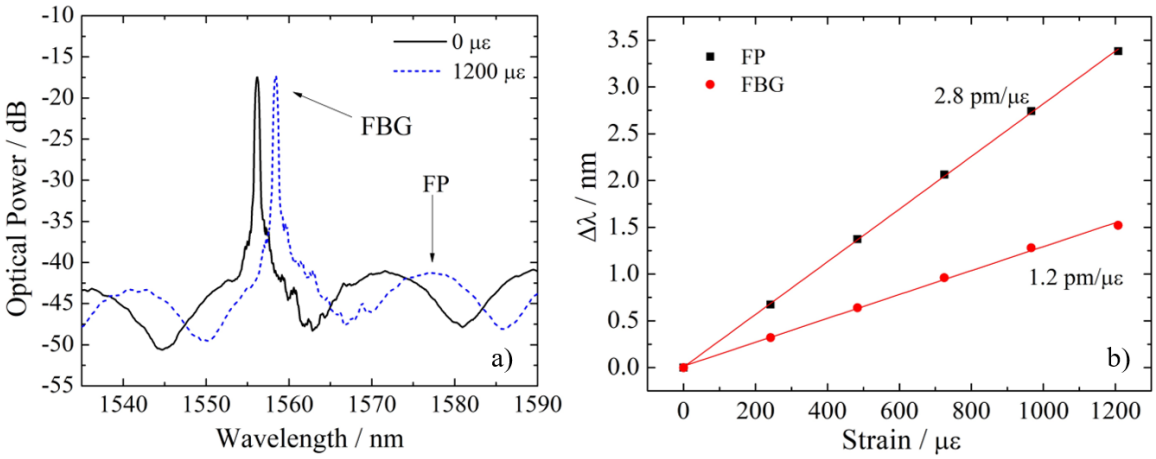

Figure VII.5. a) Spectral response of the hybrid sensor for an applied strain of 0 με and 1200 με and b) wavelength shift with the applied strain.

Tables VII.1 and VII.2 show the temperature and strain sensitivities obtained for each hybrid sensor before and after embedded in the LIB and for the network of external FBGs. The length of each FP cavity produced is also presented in Table VII.2.

Table VII.1. Temperature and strain sensitivities of all FBGs obtained before and after embedding.

Sensors location		***FBG***				
		λ_B **/ nm**	k_T **± 0.1 pm/°C**		$k\varepsilon$ **± 0.1 pm/με**	
			Before embedding	***After embedding***	***Before embedding***	***After embedding***
Hybrid Sensor Top		1536.01	8.1	30.0	1.2	0.9
Hybrid Sensor Middle		1535.83	8.0	14.0	1.1	0.8
Hybrid Sensor Bottom		1556.48	9.0	24.0	0.9	0.7
External FBGs	*Top*	1559.40	9.2		-	
	Middle	1561.41				
	Bottom	1562.64				

Table VII.2. Temperature and strain sensitivities of all FPs obtained before and after embedding.

Sensors location	***FP***				
	k_T **± 0.1 pm/°C**		$k\varepsilon$ **± 0.1 pm/με**		L **± 0.1 /μm**
	Before embedding	***After embedding***	***Before embedding***	***After embedding***	
Hybrid Sensor Top	0.1	40.0	2.3	1.9	66.2
Hybrid Sensor Middle	0.1	28.0	2.0	0.9	53.9
Hybrid Sensor Bottom	0.1	29.0	2.8	2.2	79.5

From the internal strain and temperature calibrations, and according to the matrixial method (Eq. 6), determinant values of 21.0, -9.8, and 32.5 were obtained for the hybrid sensors placed at the top, middle, and bottom positions, respectively.

3. Results and discussion

3.1 Preliminary test: External temperature and strain discrimination

The temperature and strain variations registered by the hybrid sensor fixed externally and parallel to the prismatic battery are presented in Fig. VII.6. The cycling protocol, where the discharge rate of 1.32 C was applied, is also presented. The temperature and strain

discrimination were performed considering the matrixial method previously presented in Eq. (6), and the calibrations presented in Tables VII.1 and VII.2.

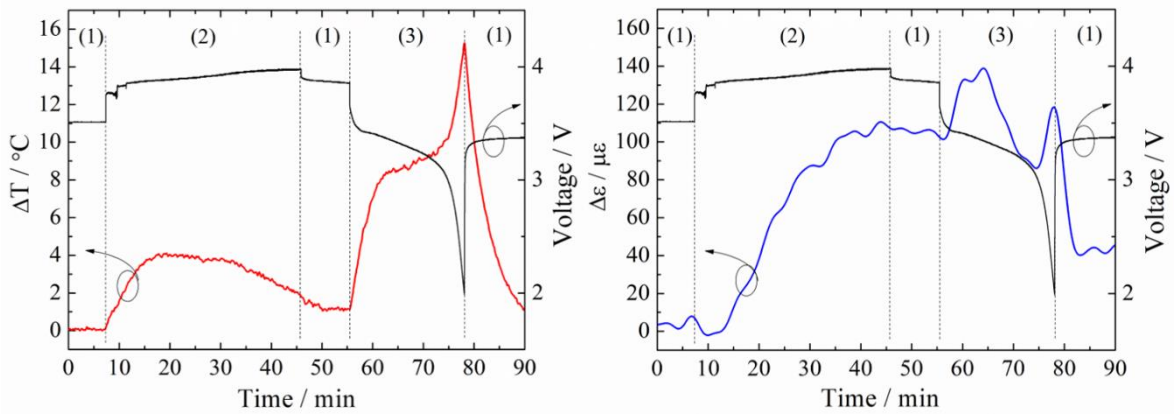

Figure VII.6. External temperature and strain variations detected by the hybrid sensor.

The step (1) corresponds to constant voltage (CV) steps of ~10 min, which were used to stabilize the LIB during the cycling protocol. Over the constant current (CC) charge step (2), a maximum temperature variation of 4.0 ± 0.1 °C was measured during the first 12 min, and a maximum strain variation of 110.0 ± 0.1 με was obtained near the end of this step. During the CC discharge step, two moments of increase of temperature occurs. The first, during the first ~5 min until the voltage reaches the cut-off (3.2 V), registering a ΔT of 8.3 ± 0.1 °C. The second fast increase of temperature was recorded between the 3.0 V and 2.0 V, reaching ΔT of 15.3 ± 0.1 °C.

Regarding the strain variations during this step, also two moments of increasing occur, however, a relaxation of ~60.0 με can be observed between these two maxima. In the first and second increases, Δε values of 138.9 ± 0.1 με and 118.5 ± 0.1 με were registered by the hybrid sensor, respectively.

The ΔT and Δε values obtained through this preliminary test along the real time battery monitoring are in accordance with the already reported in the literature [15,18]. Thus, the methodology used proves to be a satisfactory, precise and useful for the simultaneous discrimination of temperature and strain.

3.2 Li-ion pouch cell: Internal temperature and strain discrimination

Three different positions (top, middle and bottom) were internally monitored in the Li-ion pouch cell. Fig. VII.7 presents the ΔT and $\Delta\varepsilon$ values recorded by all optical sensors during the galvanostatic cycling protocol. In total, 8 charge/discharge cycles between the voltage values of 3.9 V and 2.0 V were applied. The three first cycles were at 0.5 C, the following three at 1.0 C, and the last 2 cycles at 0.25 C. Three different steps were applied: CC charge, CV charge, and CC discharge.

The temperature and strain variations registered by the optical sensors placed on the top positions are presented in Fig. VII.7 a) and b), respectively. Analyzing all the reported data, it is evident that during the cycling protocol, all the internal sensors follow with high accuracy the voltage signals, evidencing the reliability of these sensors to monitor internal parameters in LIB. It is also possible to observe that a significant difference between the ΔT values detected by the internal and external sensors occurs.

During all cycles, the increase of temperature is more accentuated when the battery is submitted to the charge process. Internally, the temperature variations that occurs in the battery are higher, reaching differences of 1.2 ± 0.1 °C when compared to the external sensor, during the lower C-rate. Maximum ΔT of 2.7 ± 0.1 °C and 1.8 ± 0.1 °C were recorded in the end of the CC charge process at 0.3 C, for the internal and external sensors, respectively. Regarding the strain variations (Fig. VII.7 b) recorded by the hybrid sensor placed in the top position, a contraction of $\sim 20.0 \pm 0.1$ με was detected during the lower C-rate cycles, in particular at the end of each CC charge step, i.e., at ~12h and ~18h. However, this variation represents a contraction of the cell in this region, probably due to the Li^+ transport to negative electrode area. During the discharge processes, variations of 13.0 ± 0.1 με can be observed, representing and expansion on this area, reflecting the inverse flux of the Li^+.

Figures VII.7 c) and d) show the temperature and strain variations monitored by the sensors in the center of the active area of the cell. Internal and external maximum ΔT values of 3.3 ± 0.1 °C and 2.5 ± 0.1 °C were recorded in the end of the CV charge process, respectively. Comparatively with the top position, this greater sensed variation is probably

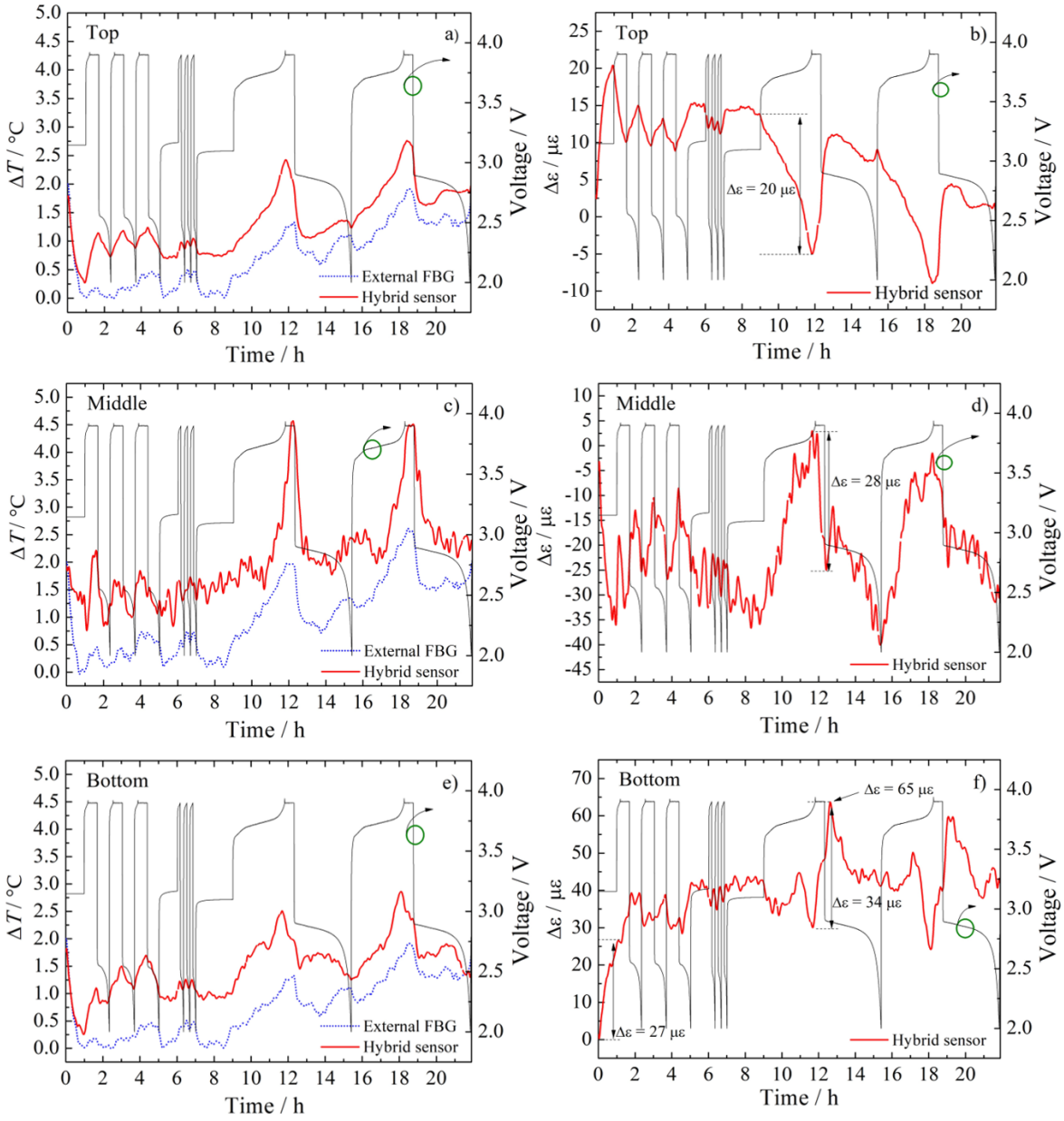

Figure VII.7. a), c), and e) Internal and external temperature variations monitored by optical sensors and b), d), and f), internal strain variations detected by the hybrid sensors, on the top, middle and bottom positions, respectively.

related with some heat accumulation and higher electrochemical activity in this area. In this area, a difference of ~2.5 ± 0.1 °C was found, during the CV charge step, between the internal and external sensors.

Concerning strain (see Fig. VII.7 d)), the maximum variation detected by the internal sensor was of 38.0 ± 0.1 με, in the end of the slow CC charge process. After this, when the

discharge process begins, a decreasing of the strain variation can be observed, and simultaneously, a relaxation of the cell in the center of the active area. Under the CV charge step, between 11.8 h and 12.4 h, a successive contraction in this area up to 28.0 ± 0.1 με, as indicated by arrows in Fig. VII.7 d), can be observed. The reason behind the negative strain detected by the sensor located in the middle in the first hour is still not fully understood. One explanation can be attributed to the fact that this sensor misaligned during the battery assembly and a small curvature was created.

The optical sensors identified successive temperature and strain fluctuations in the bottom area, as can be seen in Fig. VII.7 e) and f), respectively. This probably is related to the successive activation/inactivation of the Li^+ to flow between the negative and positive electrodes along the galvanostatic cycling protocol. When the CC charge process starts, a progressive increase of ΔT values is not observed, and an interruption occurs around the 3.8 V with a small decrease of the ΔT values. After this, it is observed a new increase of the temperature, reaching a maximum of 2.5 ± 0.1 °C, in the end of the CC charge step.

When the CV charge process was applied, a consequent decrease of temperature can be observed, and after this, when the CC discharge starts, a successive decreasing was measured, with a subsequent increase when the cell voltage crosses the 2.9 V, reaching internal temperature variation of 1.5 ± 0.1 °C.

The strain variations detected by the sensor located at the bottom are presented in Fig. VII.7 f). During the first hour, when the cycling protocol begins, an expressive expansion of 27.0 ± 0.1 με was detected in this area of the cell. As in the temperature signals, also the strain signal undergoes constant fluctuations during all the experiment. In this area, higher strain variations of 34.0 ± 0.1 με were obtained between the beginning of the CV charge and the CC discharge steps, reaching a maximum Δε value of 65.0 ± 0.1 με, as indicated by arrows in Fig. VII.7 f, followed by a decrease and subsequent relaxation of 23.0 ± 0.1 με, up to the end of this last step.

This strain values can be translated to displacement values (ΔD), in micrometers, through the Equation (7),

$$\Delta D = \Delta\varepsilon \times D \ , \qquad (7)$$

where D represent the distance between the fixed points of the fiber. Thus, a maximum displacement in the x-axis of 3.9 μm was obtained by the sensors in the bottom area. These

calculated values are in accordance with the reported in the literature through a 3D digital image correlation [1].

All the strain variations are correlated with the temperature variations detected, due to the thermal expansion of the material that compose the cell, and with the constant Li^+ fluctuation and intercalation from and to the positive electrode on the charge/discharge processes.

4. Conclusions

In this study, a hybrid sensing methodology based on an FBG sensor in series with a FP cavity, was used in the surface of a LIB to discriminate strain and temperature variations. After a successful prove of concept, it was embedded in a lithium ion pouch cell to monitor and discriminate *operando* and *in situ* internal strain and temperature shifts in three different areas of the cell (top, middle and bottom).

Galvanostatic cycling at different C-rates was applied to the cell and the evolution of strain and temperature was followed with the proposed sensor. In the end of the CC charge step at lower C-rate, maximum temperature and strain variations, i.e., 2.7 ± 0.1 °C and 20.0 ± 0.1 με, respectively, were recorded by the sensor placed in the top position. In the end of the CV charge step for the same C-rate, maximum temperature and strain values of 3.3 ± 0.1 °C and 38.0 ± 0.1 με, were measured in the middle point, respectively.

The maximum absolute strain variations were detected in the bottom and were obtained in the beginning of the CC discharge step, also at the lower C-rate, registering values of 65.0 ± 0.1 με. However, the higher ΔT detected in this area, with the value of 2.5 ± 0.1 °C, occurred in the end of the CC charge step.

It is evident that higher temperature variations lead to higher strain variations, which are promoted by the rapid Li^+ transport/intercalation between/into the positive and negative electrodes. There is an expansion increase when the temperature also increases, due to the thermal expansion of the battery materials. Thus, the internal structure of the battery is an important parameter to consider which can influence the behavior of battery materials in terms of expansion and contraction over its operation.

To the best of our knowledge, this is the first time that this hybrid sensing methodology is proposed for *in situ* measurement in LIB, and that, an internal quantification of the strain

values produced during charge/discharge processes are reported. The sensing methodology presented to discriminate internal strain and temperature proved to be an effective, non-invasive, and precise option to monitor lithium batteries real time, multipoint and *operando*. This is a helpful tool to design future batteries promoting particularly their safety.

Acknowledgements: Micael Nascimento and Susana Novais gratefully acknowledge the funding of Project POCI-01-0145-FEDER-016414, cofinanced by Programa Operacional Competitividade e Internacionalização and Programa Operacional Regional de Lisboa, through Fundo Europeu de Desenvolvimento Regional (FEDER) and by National Funds through FCT – Fundação para a Ciência e Tecnologia for research fellowships BI/UI96/6642/2018 and BI/UI96/6643/2018, respectively. Marta S. Ferreira is also grateful for the research fellowship SFRH/BPD/124549/2016. Stephan Koch acknowledges Foundation of German Business for financial support. Base funding of the Helmholtz association is kindly acknowledged. All authors also gratefully acknowledge the European Project "Stable Interfaces for Rechargeable Batteries "(SIRBATT) (FP7-ENERGY-2013, grant agreement No. 608502).

Author Contributions: All authors contributed equally. Micael Nascimento, Susana Novais, Marta S. Ferreira, Markus S. Ding and Stephen Koch conceived the experiments and analyzed the data. All authors wrote and revised the paper.

Conflicts of Interests: The authors declare no conflicts of interest.

References

[1] P. K. Leung, C. Moreno, I. Masters, S. Hazra, B. Conde, M. R. Mohamed, R. J. Dashwood, R. Bhagat, Real-time displacement and strain mappings of lithium-ion batteries using three-dimensional digital image correlation, J. Power Sources 271 (2014) 82-86, DOI: 10.1016/j.jpowsour.2014.07.184.

[2] P. Wang, X. Zhang, L. Yang, X. Zhang, M. Yang, H. Chen, D. Fang, Real-time monitoring of internal temperature evolution of li ion coin cell battery during the charge and discharge process, Extreme Mech. Lett. 9 (2016) 459-466, DOI: 10.1016/j.eml.2016.03.013.

[3] Z. Zhang, P. Ramadass, W. Fang, Safety of lithium-ion batteries. In Lithium-ion batteries: Advances and applications. 1st Ed.; Gianfranco Pistoia; Publisher: Elsevier Amsterdam, Netherlands, 18, 409-435, ISBN: 978-0-444-59513-3 (2014).

[4] W. Xianming, S. Yoshitsugu, S. Go, N. Hitoshi, Y. Chisa, K. Koichi, Understanding volume change in Lithium-ion cells during charging and discharging using in situ measurements, J. Electrochem. Soc. 154 (2007) A14-A21, DOI: 10.1149/1.2386933.

[5] H. L. Jae, M. L. Hyang, A. Soonho, Battery dimensional changes during charge/discharge cycles – thin rectangular lithium ion and polymer cells, J. Power Sources 119-121 (2003) 833-837, DOI: 10.1016/S0378-7753(03)00281-7.

[6] D. Yih-Shing, H.L. Kai, K. Chen-Shan, Experimental investigation and visualization on thermal runaway of hard prismatic lithium-ion batteries used in smart phones, J. Therm. Anal. Calorim. (2018) 1-16, DOI: 10.1007/s10973-018-7077-2.

[7] T. M. Bandhauer, S. Garimella, T. F. Fuller, A critical review of thermal issues in lithium-ion batteries, J. Electrochem. Soc. 158 (2011) R1-R25, DOI: 10.1149/1.3515880.

[8] Q. Wang, P. Ping, X. Zhao, G. Chu, J. Sun, C. Chen, Thermal runaway caused fire and explosion of lithium ion battery, J. Power Sources 208 (2012) 210-24, DOI: 10.1016/j.jpowsour.2012.02.038.

[9] S. Panchal, I. Dincer, M. Agelin-Chaab, R. Fraser, M. Fowler, Experimental temperature distributions in a prismatic lithium-ion battery at varying conditions, Int. Commun. Heat Mass Transfer 71 (2016) 35-43, DOI: 10.1016/j.icheatmasstransfer.2015.12.004.

[10] M. S. K. Mutyala, J. Zhao, J. Li, H. Pan, C. Yuan, X. Li, In situ temperature measurement in lithium-ion battery by flexible thin film thermocouples, J. Power Sources 260 (2014) 43-49, DOI: 10.1016/j.jpowsour.2014.03.004.

[11] Y. Fu, S. Lu, K. Li, C. Liu, X. Cheng, H. Zhang, An experimental study on burning behaviors of 18650 lithium ion batteries using a cone calorimeter, J. Power Sources 273 (2015) 216-222, DOI: 10.1016/j.jpowsour.2014.09.039.

[12] X. Yu, Z. Feng, Y. Ren, D. Henn, Z. Wu, K. An, B. Wu, C. Fau, C. Li, and S. J. Harris, Simultaneous operando measurements of the local temperature, state of charge, and strain inside a commercial lithium-ion battery pouch cell, J. Electrochem. Soc. 7 (2018) 165 A1578-A1585, DOI: 10.1149/2.1251807jes.

[13] K. T. V. Grattan, B. T. Meggitt, Optical fiber sensor technology: Applications and Systems. Publisher: Kluwer Academic Publishers, London, 3 357-363, ISBN: 978-1-4757-6077-4 (1999);

[14] G. Yang, C. Leitão, Y. Lib, J. L. Pinto, X. Jiang, Real-time temperature measurement with fiber Bragg sensors in lithium batteries for safety usage, Measurement 46 (2013) 3166-3172, DOI: 10.1016/j.measurement.2013.05.027.

[15] M. Nascimento, M. S. Ferreira, J. L. Pinto, Simultaneous Sensing of Temperature and Bi-Directional Strain in a Prismatic Li-Ion Battery, Batteries 4 (2018) 23, DOI: 10.3390/batteries4020023.

[16] L. W. Sommer, P. Kiesel, A. Ganguli, A. Lochbaum, B. Saha, J. Schwartz, C.-J. Bae, M. Alamgir, Fast and slow ion diffusion processes in lithium-ion pouch cells during cycling observed with fiber optic strain sensors, J. Power Sources 296 (2015) 46-52, DOI: 10.1016/j.jpowsour.2015.07.025.

[17] S. Novais, M. Nascimento, L. Grande, M. F. Domingues, P. Antunes, A. Alberto, C. Leitão, R. Oliveira, S. Koch, G.-T. Kim, S. Passerini, J.L. Pinto, Internal and external temperature monitoring of a Li-ion battery with fiber Bragg grating sensors, Sensors 16 (2016) 1394, DOI: 10.3390/s16091394.

[18] M. Nascimento, M. S. Ferreira, J. L. Pinto, Real time thermal monitoring of lithium batteries with fiber sensors and thermocouples: A comparative study, Measurement 111 (2017) 260-263, DOI: 10.1016/j.measurement.2017.07.049.

[19] C.-J. Bae, A. Manandhar, P. Kiesel, and A. Raghavan, Monitoring the strain evolution of lithium-ion battery electrodes using an optical fiber Bragg grating sensor, Energy Technol. 4 (2016) 1–6, DOI: 10.1002/ente.201500514.

[20] D. Homa, C. Hill, A. Floyd, and G. Pickrell, Fiber Bragg gratings embedded in 3D printed prototypes, Sci. Adv. Today 2 (2016) 25242.

[21] M. R. Mokhtar, T. Sun, and K. T. V. Grattan, Bragg grating packages with non-uniform dimensions for strain and temperature sensing, IEEE Sens. J. (2012) 12, 139–144, DOI: 10.1109/JSEN.2011.2134845.

[22] O. Frazão, M. Melo, P. V. S. Marques, and J. L. Santos, Chirped Bragg grating fabricated in fused fibre taper for strain-temperature discrimination, Meas. Sci. Technol. (2005) 16, 984–988, DOI: 10.1088/0957-0233/16/4/010.

[23] C. Fernández-Valdivielso, I. R. Matías, and F. J. Arregui, Simultaneous measurement of strain and temperature using a fiber Bragg grating and a thermochromic material, Sens. Actuators A (2002) 101, 107–116, DOI: 10.1016/S0924-4247(02)00188-7.

[24] L. A. Ferreira, F. M. Araújo, J. L. Santos, and F. Farahi, Simultaneous measurement of strain and temperature using interferometrically interrogated fiber Bragg grating sensors, Opt. Eng. (2000) 39, 2226–2234, DOI: 10.1117/1.1305493.

[25] J. Jung, N. Park, and B. Lee, Simultaneous measurement of strain and temperature by use of a single fiber Bragg grating written in an erbium:ytterbium-doped fiber, Appl. Opt. (2000) 39, 1118–1120.

[26] Q. Liu, Z. L. Ran, Y. J. Rao, S. C. Luo, H. Q. Yang, and Y. Huang, Highly integrated FP/FBG sensor for simultaneous measurement of high temperature and strain, IEEE Photon. Technol. Lett. (2014) 26, 1715–1717, DOI: 10.1109/LPT.2014.2331359.

[27] Y. Jiang, D. Yang, Y. Yuan, J. Xu, D. Li, and J. Zhao, Strain and high-temperature discrimination using a Type II fiber Bragg grating and a miniature fiber Fabry-Perot interferometer, Appl. Opt. 55 (2016) 23 6341-6345, DOI: 10.1364/AO.55.006341.

[28] B. Dong, J. Hao, C. Liaw, B. Lin, S.C. Tjin, Simultaneously strain and temperature measurement using a compact photonic crystal fiber inter-modal interferometer and fiber Bragg grating, Appl. Opt. 49 (2010) 32 6232-6235, DOI: 10.1364/AO.49.006232.

[29] S. Novais, M. S. Ferreira, J. L. Pinto, Lateral load sensing with an optical fiber inline microcavity, IEEE Photon Technol Lett. 29 (2017) 17 1502–1505, DOI: 10.1109/LPT.2017.2735021.

[30] Y. Liu, D. N. Wang, W. P. Chen, Crescent shaped Fabry-Perot fiber cavity for ultra-sensitive strain measurement, Scientific Reports Nature (2016) 6:38390, DOI: 10.1038/srep38390.

[31] A. K. Singh, S. Berggren, Y. Zhu, M. Han, and H. Huang, Simultaneous strain and temperature measurement using a single fiber Bragg grating embedded in a composite laminate, Smart Mater. Struc. 26 (2017) 115025, DOI: 10.1088/1361-665X/aa91ab.

[32] M. G. Zubel, K. Sugden, D. J. Webb, D. Saez-Rodriguez, K. Nielsen, and O. Bang, Proc. of SPIE 9886, 98860N (2016), DOI: 10.1117/12.2228753.

[33] Y. Zhang, X. Chen, Y. Wang, K. L. Cooper, A. Wang, Microgap multicavity Fabry-Perot biosensor, J. Lightw. Technol. 25 (2007) 1797-1804, DOI: 10.1109/JLT.2007.899169.

[34] J. R. Zhao, X. G. Huang, W. X. He, J. H. Chen, High-resolution and temperature-insensitive fiber optic refractive index-based sensor on Fresnel reflection modulated by Fabry-Perot interference, J. Lightw. Technol. 28 (2010) 2799-2803, DOI: 10.1109/JLT.2010.2065215.

[35] B. H. Lee, Y. H. Kim, K. S. Park, J. B. Eom, M. J. Kim, B.S. Rho, H.Y. Choi, Interferometric Fiber Optic Sensors. Sensors 12 (2012) 2467-2486, DOI: 10.3390/s120302467.

[36] O. Frazão, J. L. Santos, Simultaneous measurement of strain and temperature using a Bragg grating structure written in germanosilicate fibres, J. Opt. A: Pure Appl. Opt. 6 (2004) 553–556, DOI: 10.1088/1464-4258/6/6/010.

[37] D. W. Duan, Y. J. Rao, Y. S. Hou, T. Zhu, Microbubble based fiberoptic Fabry–Perot interferometer formed by fusion splicing single-mode fibers for strain measurement, Appl. Opt. 51 (2012) 8 1033–1036, DOI: 10.1364/AO.51.001033.

[38] N. Loeffler, J. Zamory, N. Laszczynski, I. Doberdo, G.-T. Kim, S. Passerini, Performance of LiNi1/3Mn1/3Co1/3O2/graphite batteries based on aqueous binder, J. Power Sources 248 (2014) 915–922, DOI: 10.1016/j.jpowsour.2013.10.018.

Chapter VIII

Final remarks and future developments

Final remarks and future developments

The sensing of characteristic parameters, such as temperature and strain variations in lithium-ion batteries (LIBs) seems to be an essential issue to ensure their operation in safe conditions. Typically, LIBs are monitored through electronic sensing devices. However, in addition to low resolution and accuracy, higher dimensions and invasiveness, these sensors are not suitable to be embedded in LIBs, due to the harsh electrochemical environment of the battery. Alternative solutions, with higher precision, multipoint capabilities, reduced the system costs, and that can be easily integrated in LIBs with low invasiveness, are the fiber optic sensors.

In this Thesis, this matter was addressed by proposing different sensing networks based on fiber Bragg gratings (FBGs) to study, monitor, and quantify multipoint temperature and strain variations in different configurations of LIBs (cylindrical, prismatic, and pouch cell). The studies comprised both external and internal monitoring; during normal and abusive operating conditions, i.e. under different environments and/or charge/discharge C-rates.

The following lines summarize the main results and contributions for each Chapter, together with future work perspectives.

[Chapter II] The optical sensors responses were compared with electronic devices, namely K-type thermocouples (TCs). The results obtained show that the FBGs had a rise time 28.2% lower than the TCs, making them a better choice for the real time monitoring for this specific application. However, other type of studies could be done, for instance, by comparing the thermal responses of the FBGs with other type of TCs or other electronic sensors.

[Chapter III] Temperature and strain shifts in the surface of a cylindrical rechargeable LIB were monitored with FBG sensors, based on the FBG strain-free method. During the discharge at 1.33 C, a higher temperature fluctuation was measured, with a consequent strain increase, induced by a larger internal pressure of the battery.

In the future, other type of experimental tests could be done, by integrating a rolled up elliptical sensing configuration along this type of battery, to monitor the battery thermal expansion in that direction.

[Chapter IV] Temperature and bi-directional (*x*- and *y*-direction) strain variations were simultaneously monitored in a prismatic rechargeable LIB surface through a network of FBG

sensors. When the battery was subjected to abnormal operating conditions, it is evident that higher temperature and strain variations occur, which are promoted by the rapid Li^+ transport between the positive and negative electrodes. Over the CC charge step, maximum temperature and strain variations were reached at the end of the process. A maximum LIB longitudinal expansion of 0.06% was detected. Due the thermal expansion of the materials that compose the battery, its internal structure is an important parameter to have in consideration and can influence the behavior of the battery materials in terms of expansion and contraction over its operation.

The simultaneous monitoring of temperature and different components of strain could also be assessed by inscribing FBGs in birefringent fibers, such as the bow-tie or the PANDA fibers.

[Chapter V] Temperature changes in a smartphone LIB surface were monitored by a FBGs network, during testing under different environmental conditions (cold, temperate, and dry climates) at constant charge and different discharge rates (1.32 C, 2.67 C, and 5.77 C). According to the cycling tests, when the battery is exposed to the cold environment, the time that the battery took to perform the same cycling protocol was ~35% lower when compared to the others two environments. In general, lower temperature variations were detected when the LIB operated under the cold environment. The higher temperature shifts detected by the FBGs in the other two environments, are related with the greater performance of the LIB in terms of discharge capacity and power capabilities, indicating that these environmental conditions are the best to operate the LIBs in order to extend their lifetimes.

However, studies under other types of environmental conditions can be implemented, and other type of batteries configurations can also be tested. In this case, special attention should be given to the pouch cells, a configuration that is still being actively investigated in the lab-scale.

[Chapter VI] A network of 37 FBG sensors was used to temporal and spatial thermal mapping the interfaces of a lithium polymer batteries (LiPBs) pack connected in series. In general, over the charge and discharge steps the hotter zones were located at the both collector tabs, due to the higher current density of the Li^+ in that region, and the cold zones were at the bottom of the LiPBs pack.

A comparative study, with the LiPBs pack connected in parallel should be developed, in order to completely understand how the type of pack connections can influence the zones of appearance of hot spots.

[Chapter VII] The simultaneous measurement of internal temperature and strain variations in a Li-ion pouch cell configuration was achieved by employing a hybrid sensor, that combined the operational characteristics of both FBG and Fabry-Perot interferometer sensors. Galvanostatic cycling at different C-rates was applied to the cell and the evolution of strain and temperature was followed with the proposed sensor. Higher temperature shifts lead to higher strain changes, which are promoted by the rapid Li^+ transport/intercalation between/into the positive and negative electrodes. There is an expansion increase when the temperature also increases, due to the thermal expansion of the battery materials. Thus, the internal structure in this type of battery configuration is also an important parameter to consider, which can influence the behavior of battery materials in terms of expansion and contraction over its operation. To the best of our knowledge, this is the first time that this hybrid sensing methodology is proposed for *in situ* measurement in LIBs, and that, an internal quantification of the strain values produced during charge/discharge processes are reported.

However, a different approach could be performed by writing FBGs in a multicore fiber. The FBGs can be written in different cores, enabling an internal 3D strain monitoring of locations of interest. More internal points could also be monitored to get a total knowledge of the entire active area of the battery. The influence of different cathode materials or pouch cells dimensions might also be studied. Furthermore, the integration of optical sensors in different layers should be tested.

In the future, all information gathered from the optical sensors could be readily available to the user, through the creation of a digital platform where the data would be acquired and analyzed in real time. This could also be integrated in the battery management systems already available, which are currently focused on detection of voltage, current, capacity, and external temperature.

The sensing networks presented in this Thesis, proved to be an effective, precise, non-invasive and alternative and useful tool to:

- ✓ Real time, multipoint, *in situ* and *operando* monitor temperature and bi-directional strain changes in LIBs surfaces;
- ✓ Promote the design optimization of next LIBs generation;
- ✓ Develop new intrinsic materials for the prevention of thermal runaway in LIBs;
- ✓ Improve thermal management and safety of LIBs, identifying critical zones for the appearance of hot spots, due to the thermal profile's recognition.
- ✓ Discriminate internal strain and temperature in Li-ion pouch cells.

The optical fiber sensing network developed in this work, associated with the development of other types of fiber sensors, can be used to monitor internal and external characteristic parameters in other types of emerging batteries, such as the hydrogen fuel cells. Hydrogen has been widely used in many industrial processes, such as automobile fuel, petroleum extraction, and most importantly, power generation. However, great safety concerns are associated with the transportation, storage and usage of hydrogen, because it is highly explosive in air when its volume concentration reaches to the lower explosive limit (4%) [1, 2]. Therefore, the reliable and accurate monitoring of hydrogen at low concentrations is extremely important [3]. Temperature and relative humidity (RH) are also important hydrogen fuel cell parameters, as they significantly affect the performance of proton exchange membrane fuel cells, particularly due to the effect that these coupled parameters have on the water balance within the cell, charge transfer resistance, as well as catalytic activity, mass transfer, and heat management [4]. Thus, it is essential to monitor characteristic parameters inside the hydrogen fuel cells during its operation, such as, hydrogen and oxygen concentrations, temperature, and RH. All these parameters can be measured using adequate fiber sensing configurations. Furthermore, the integration of optical fiber sensors with hydrogen fuel cells will allow a significant scientific breakthrough in the field of energetic sustainability with significant advantages in safety and autonomy of these cells.

Recently, the sensing networks developed in the context of this Thesis have also been applied in a different application. They have been integrated during the additive manufacturing-based hybrid processes for long and continuous fiber reinforced thermoplastic matrix composites. It is expected that these networks can be used for improving the hybrid additive manufacturing design, as well as the multifunctional and graded features.

Optical sensing networks were successfully embedded simultaneously to the printing of new materials, in order to monitor the fabrication process temperature. The results were compared with the data provided by thermography. In a near future, the sensing networks will be further developed and used in matrices of different types of composite materials, such as, polylactic acid (PLA) matrix, PLA matrix reinforced by nickel-titanium wires, polyether ether ketone matrix, and carbon matrix in different carbon concentrations. The aim is to attain accurate responses towards strain, temperature and RH, among other parameters of interest.

References

[1] Y.Zhang, H. Peng, X. Qian, Y. Zhang, G. An, and Y. Zhao. Recent advancements in optical fiber hydrogen sensors. *Sensors and Actuators B*, 2017, 244, 393 – 416, DOI: 10.1016/j.snb.2017.01.004.

[2] G. Zhang, M. Yang, and Y. Wang. Optical fiber-tip Fabry–Perot interferometer for hydrogen sensing. *Opt. Commun*., 2014, 329, 34 - 37, DOI: 10.1016/j.optcom.2014.04.084.

[3] C-Y. Lee, F-B. Weng, C-H. Cheng, H-R. Shiu, S-P. Jung, W-C. Chang, P-C. Chan, W-T. Chen, and C-J. Lee. Use of flexible micro-temperature sensor to determine temperature in situ and to simulate a proton exchange membrane fuel cell. *J. Power Sources*, 2011, 196, 228 - 234, DOI: 10.1016/j.jpowsour.2010.06.051.

[4] N.A. David, P.M. Wild, J. Jensen, T. Navessin, and N. Djilali. Simultaneous In Situ Measurement of Temperature and Relative Humidity in a PEMFC Using Optical Fiber Sensors. *J. Electrochem Soc*., 2010, 157, 8, B1173 - B1179, DOI: 10.1149/1.3436652.